EXPERIMENTAL INVESTIGATION OF THE INFLUENCE OF SURFACE ENERGY AND PORE FLUID CHARACTERISTICS ON THE BEHAVIOR OF PARTIALLY SATURATED COARSE-GRAINED SOILS

A Thesis
Presented to
The Academic Faculty

by

Ross E. Cutts

In Partial Fulfillment
of the Requirements for the Degree
Masters of Science in the
School of Civil Engineering

Georgia Institute of Technology
August 2009

EXPERIMENTAL INVESTIGATION OF THE INFLUENCE OF SURFACE ENERGY AND PORE FLUID CHARACTERISTICS ON THE BEHAVIOR OF PARTIALLY SATURATED COARSE-GRAINED SOILS

Approved by:

Dr. Susan E. Burns, Advisor
School of Civil and Environmental Engineering
Georgia Institute of Technology

Dr. Glenn J. Rix
School of Civil and Environmental Engineering
Georgia Institute of Technology

Dr. J. Carlos Santamarina
School of Civil and Environmental Engineering
Georgia Institute of Technology

Date Approved:

To the many people in my life who helped foster my curiosity.

ACKNOWLEDGEMENTS

I would like to thank my advisor, Dr. Susan Burns, for not only being a wonderful mentor, but also a good friend. As Dr. Burns best put it, “You are not working under me, you are working beside me on this journey.” With this in mind I am forever grateful to have had the opportunity of exploration with such a wonderful advisor and research group. I would also like to thank my committee for their valuable input, and in particular Dr. Santamarina for the wonderful conversations and insights that he provided. I truly look up to both of you, and I hope one day to be as knowledgeable and gentle hearted as you have been to me.

I would also like to thank my parents for planting the seed that made this possible. Growing up my parents created an environment very open towards learning and curiosity for which I am very fortunate and grateful. I still remember countless times when things would end up in a mess or broken, but as long as it was due to a “science experiment” my parents were always supportive.

I would also like to acknowledge my future wife and best friend Erin Griffin for her unending support. She is my foundation which never wavers, and who makes all the hard work worthwhile. I am so lucky to have found someone with whom I share so much, I look forward to our many adventures that lie ahead.

TABLE OF CONTENTS

Page

ACKNOWLEDGEMENTS ..... **iv**

LIST OF TABLES ..... **viii**

LIST OF FIGURES ..... **ix**

SUMMARY ..... **xii**

Chapter 1 INTRODUCTION **1**

Chapter 2 LITERATURE REVIEW **6**

2.1. Saturation stages 6

2.2. Effective stress in unsaturated soils 8

2.3. Menisci geometry 9

2.4. Particle packing 12

2.5. Surface energy and water interaction 13

2.6. Properties of the solid substrate: silica 14

2.7. Properties of the solid substrate: polytetrafluoroethylene 16

2.8. Contact angle 17

2.9. Surface tension 19

2.10. Fluid phases with dissolved salts 21

2.11. Vapor pressure and stability of calcium chloride solutions 23

Chapter 3 MATERIALS and METHODS **25**

3.1. Materials 26

3.2. Methods 27

3.3. Packing model development 29

3.4. Resultant force vectors for partially saturated soils 30

3.5. Coarse spherical grained soil polyhedron unit and pore space volume 32

Chapter 4 RESULTS and ANALYSIS **35**

4.1. Contact angle and wetting 35

4.2. Surface tension 40

4.3. Meniscus modeling: optical analysis 41

4.4. Meniscus modeling: mass-based analysis 43

4.5. Empirical modeling of meniscus evaporation between two spherical glass beads 46
4.6. Salt precipitation and cementation 50
4.7. Capillary Rise 71
4.8. Discussion 83
4.9. Engineering implications 83

Chapter 5 CONCLUSIONS 86

5.1. Overview 86
5.2. Limitations 87

REFERENCES 88

LIST OF TABLES

Page

Table 3-1. Experimental Matrix 26
Table 3-2. Volume and Void Space Relationships for Studied Packings 33
Table 3-3. Porosity and Number of Menisci for Studied Packings 34
Table 4-1. Advancing and Receding Contact Angles Measured on Glass and PTFE 36
Table 4-2. Lower Estimate for Minimal Pore Radii for Studied Packings 72
Table 4-3. Upper Estimate for Minimal Pore Radii for Studied Packings 73

LIST OF FIGURES

Page

Figure 1-1. Gas-liquid menisci; a) convex on the gas side; b) concave on the gas side. For gas-liquid interfaces, the phase with the lower pressure expands, producing a meniscus with a geometry that is concave to the higher pressure. In this fiigure, gas pressure is lower than liquid pressure in a), and gas pressure is higher than liquid pressure in b) (after Lu and Lkios, 2004). 3
Figure 2-1. Soil suction regimes of the SWCC curve as a function of water content (figure from Lu and Likos, 2004). 7
Figure 2-2. Menscius evaptionation between two sperhical particles; note the decreasing area over which the unbalanced atmospheric pressure acts. 10
Figure 2-3. Menscius evaptionation between two platey particles, showing the area over which the unbalanced atmospheric pressure acts. 12
Figure 2-4. Ideal coarse-grained packings: a) simple cubic; b) cubic tetrahedral; c): pyramidal; d) tetrahedral. 13
Figure 2-5. Governing forces operative at the gas/liquid/solid interface. 14
Figure 2-6. Orientation of the water molecules to the exposed silanol groups on the quartz surface (Iler 1979) 15
Figure 2-7. Charge densities of a 1 micron silica sphere with varing pH (firgure from Behrens and Grier 2001). 16
Figure 2-8. PTFE polymer and molecular structure. 17
Figure 2-9. Visual location of the measured contact angle on two droplets with differing contact angles; hydrophilic versus hydrophobic. 17
Figure 2-10. Simplified illustration of surface tension resulting from only the unbalanced forces acting on the molecules at the interface between the air and bulk liquid phases. 20
Figure 2-11. The alignment of the surrounding polar water molecules by their attraction to the positively charged ion, resulting in a hydration sphere. 20
Figure 2-12. Three stages of salt dissolution: a) the solute-to-solute attraction is broken; b) the solvent to solvent attraction is broken; c) the solvent to solute attraction is formed. 22
Figure 2-13. Vapor pressure of calcium chloride as a function of temperature and pressure (Dow Chemical). 24
Figure 3-1. Injection of fluid for measurement of contact angle at air/water/silica interface. 28
Figure 3-2. The four packing geometries modeled in this investigation. 30
Figure 3-3. Visualization of menisci loading along vertical axis for a simple cubic packing. 31
Figure 4-1. Contact angles measured at the air/water/solid interfaces for glass and PTFE. 36

Figure 4-2. Contact angle on soda lime glass substrate, measured as a function of sodium chloride concentration. 37
Figure 4-3. Contact angle on PTFE substrate, measured as a function of sodium chloride concentration. 37
Figure 4-4. Contact angle on soda lime glass substrate, measured as a function of calcium chloride concentration. 38
Figure 4-5. Contact angle on PTFE substrate, measured as a function of calcium chloride concentration. 38
Figure 4-6. Measured contact angles as a function of salt concentration. 39
Figure 4-7. Measured contact angles as a function of ionic strength. 40
Figure 4-8. Surface tension at the air water interface, measured as a function of sodium chloride and calcium chloride concentration. 41
Figure 4-9. Geometry used to model the evaporating water meniscus. 42
Figure 4-10. Meniscus volume change measurements based on measurements of mass reduction due to evaporation 44
Figure 4-11. Meniscus volume change measurements based on optical imaging of the reduction of meniscus dimensions due to evaporation. 45
Figure 4-12. Rate of mass change for NaCl solution and deionized water menisci evaporation. 45
Figure 4-13. Optical image of meniscus during two particle evaporation experiment. 46
Figure 4-14. Empirical model developed from fitting experimental data with Matlab. 47
Figure 4-15 Curve fitting for meniscus surface radius. 47
Figure 4-16 Curve fitting for meniscus diameter. 48
Figure 4-17. Curve fitting for meniscus thickness 48
Figure 4-18. Curve fitting varibles combined. 49
Figure 4-19. Empirical soil water characteristic curve for a single menisci based on evaporation rates determined in two particle evaporation study. 50
Figure 4-20. Configuration for optical observation of salt crystallization from fluid meniscus. 51
Figure 4-21. NaCl (0.0001 M) crystallization on 3 contact packing (soda lime glass, 3 mm diameter). 54
Figure 4-22. NaCl (0.0001 M) crystallization on 4 contact packing (soda lime glass, 3 mm diameter). 55
Figure 4-23. NaCl (0.1 M) crystallization on 3 contact packing (soda lime glass, 3 mm diameter). 56
Figure 4-24. NaCl (0.1 M) crystallization on 4 contact packing (soda lime glass, 3 mm diameter). 57
Figure 4-25. NaCl (0.5 M) crystallization on 3 contact packing (soda lime glass, 3 mm diameter). 58
Figure 4-26. NaCl (0.5 M) crystallization on 4 contact packing (soda lime glass, 3 mm diameter). 59
Figure 4-27. NaCl (1 M) crystallization on 3 contact packing (soda lime glass, 3 mm diameter). 60
Figure 4-28. NaCl (1 M) crystallization on 4 contact packing (soda lime glass, 3 mm diameter). 61
Figure 4-29. NaCl (at saturation) crystallization on 4 contact packing (soda lime glass, 3 mm diameter). 62
Figure 4-30. NaCl (1 M) crystallization on 3 contact packing (PTFE, 3 mm diameter). 63
Figure 4-31. NaCl (1 M) crystallization on 4 contact packing (PTFE, 3 mm diameter). 64
Figure 4-32. $CaCl_2$ (1 M) crystallization on 3 contact packing (soda lime glass, 3 mm diameter). 65

Figure 4-33. $CaCl_2$ (1 M) crystallization on 4 contact packing (soda lime glass, 3 mm diameter). 66
Figure 4-34. $CaCl_2$ (1 M) crystallization on 3 contact packing (PTFE, 3 mm diameter). 67
Figure 4-35. $CaCl_2$ (1 M) crystallization on 4 contact packing (PTFE, 3 mm diameter). 68
Figure 4-36. Heated evaporation of $CaCl_2$ solution on PTFE surface, and subsequent hygroscopic saturation.....69
Figure 4-37 $CaCl_2$ (1 M) hygroscopic satruation at atmospheric humidity on 4 contact packing (PTFE, 3 mm diameter).....70
Figure 4-38. Capillary rise for pre-wetted soda lime glass substrate in large and small pores as a function of NaCl concentration. 74
Figure 4-39. Capillary rise for desiccated soda lime glass substrate in large and small pores as a function of NaCl concentration. 74
Figure 4-40. Capillary rise for pre-wetted soda lime glass substrate in large and small pores as a function of $CaCl_2$ concentration. 75
Figure 4-41. Capillary rise for desiccated soda lime glass substrate in large and small pores as a function of $CaCl_2$ concentration.....75
Figure 4-42. Capillary rise for pre-wetted PTFE substrate in large and small pores as a function of NaCl concentration.....76
Figure 4-43. Capillary rise for desiccated PTFE substrate in large and small pores as a function of NaCl concentration.....76
Figure 4-44. Capillary rise for pre-wetted PTFE substrate in large and small pores as a function of $CaCl_2$ concentration.....77
Figure 4-45. Capillary rise for desiccated PTFE substrate in large and small pores as a function of CaCl2 concentration.....77
Figure 4-46. Lower bound capillary rise for pre-wetted substrates. 79
Figure 4-47. Upper bound capillary rise for pre-wetted substrates. 80
Figure 4-48. Lower bound capillary rise for desiccated substrates. 81
Figure 4-49. Upper bound capillary rise for desiccated substrates. 82
Figure 4-50. Salt crystallization patterns with no hydrogen peroxide prerinse. 85
Figure 4-51. Salt crystallization patterns with hydrogen peroxide prerinse. 85

SUMMARY

In this study, the behavior of partially saturated coarse-grained soil packings was studied as a function of solid surface composition and aqueous salt concentration. The substrates tested were PTFE and soda lime glass, while the aqueous electrolytes consisted of NaCl and $CaCl_2$ in differing concentrations. In order to gain a fundamental understanding of the unsaturated soils system, the two phase intersections of gas-liquid and solid-liquid were studied. The effect of varying aqueous electrolytes on the gas-liquid interface was analyzed by testing the surface tension while systematically varying the electrolyte concentration, while the effect on the solid/liquid/gas interface was studied by altering the surface hydrophobicity and aqueous solution concentration. In order to extend the analysis to soil fabrics, four ideal coarse gained packings were subdivided into their smallest repeating units. These repeating units, along with the measured dependence of the contact angles and surface tension on salt types, allowed an estimation of the equilibrium behavior of the capillary rise and tensile strength within a uniform coarse-grained fabric.

The major findings of this study include:

- Increasing the hydrophobicity of the solid surface increased both the advancing and receding water contact angles.
- Dissolved salt ions in water had little effect on the contact angle on a hydrophilic surface (glass), but lowered the contact angle on a hydrophobic surface (PTFE).

- Differences between advancing and receding contact angles were more pronounced for hydrophilic substrates.
- Pore fluid surface tension increased with increasing salt concentration
- The four ideal coarse-grained packings were reduced into representative elementary repeating unit volumes allowing for comparison across fabric types.
- Empirical estimation of the rate of water evaporation between a two particle contact (visual and mass-based approaches) was developed.
- Heights of capillary rise as a function of packing, surface hydrophobicity, dissolved salt concentration, and contact angle hysteresis was estimated; rise was greater given a prewetted dense packing with a hydrophilic surface.
- Height of capillary rise was relatively unaffected by the aqueous concentration of salt in contact with hydrophilic surfaces, but substantially altered in the case of hydrophobic surfaces
- NaCl precipitation in a hydrophilic particle system nucleated from the particle contacts, and continued to precipitate out in a thin film until desiccation.
- NaCl precipitation in a hydrophibic particle system nucleated as large crystals in the large pores within the packing.
- $CaCl_2$ is hygroscopic and remained as a liquid below its precipitation temperature, above the precipitation temperature salt crystallization behavior was similar to the non deliquescent salts.

Chapter 1

INTRODUCTION

The presence of interfaces in solid-liquid-gas systems is one of the most influential parameters in the mechanical behavior of partially saturated particulate materials. Specifically, the interfacial behavior known as surface tension, which occurs at the gas-liquid interface, generates additional interaction forces in partially saturated soil systems. In either the saturated or desiccated state, a coarse-grained soil develops no tensile strength between the particles, as there are no driving attractive forces between individual sand grains. However, when both liquid and gas phases are present and the soil fabric is at partial saturation, an interfacial liquid-gas membrane will develop at particle contacts, creating an apparent tensile strength between grains. This tensile strength is what allows a sand castle to be built from a partially saturated coarse-grained soil without the aid of cementation; however, the tensile strength is only present until desiccation occurs.

The attractive force which develops at interfaces in air-water systems, commonly known as surface tension, is a free energy per unit area, with units of energy per area or force per length (J/m^2 or N/m (mN/m are equivalent to dynes/cm)). Surface tension results from the unbalanced attraction between liquid molecules exposed to the gas phase on the fluid surface, and can be thought of in terms of mechanical behavior, or in terms of surface free energy (Adamson and Gast 1997). Application of the concept of surface free energy can be framed mathematically to indicate that work must be performed to bring

molecules from the interior of the fluid phase to the surface of the fluid phase (Adamson and Gast 1997).

In a particulate material that is partially saturated with water and air, a meniscus is created between particles in the coarse-grained soil fabric. The operative forces at the meniscus include the surface tension of both the liquid and gas phases, and the pressure in the liquid and gas phases. In the case of air as the gaseous phase, the surface tension of air is negligible, resulting in three forces required for equilibrium: surface tension of water, and the pressures in the water and air phases (Lu and Likos, 2004). In particulate systems at atmospheric pressure, there will be a pressure differential between the air and water phase resulting in a curvature of the interface, which results in a tensile stress on the interface (Lu and Likos, 2004), and the interface will be concave to the higher pressure side, whether that is gas or liquid (Figure 1-1).

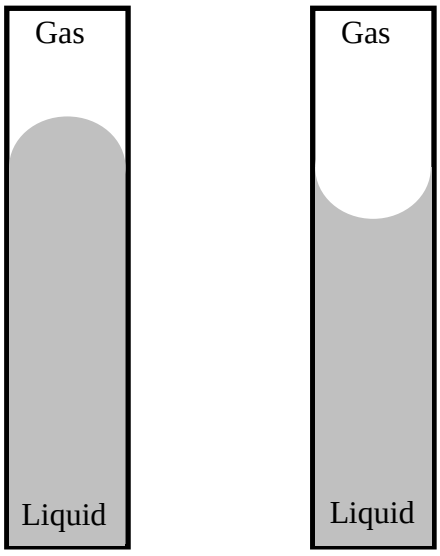

Figure 1-1. Gas-liquid menisci; a) convex on the gas side; b) concave on the gas side. For gas-liquid interfaces, the phase with the lower pressure expands, producing a meniscus with a geometry that is concave to the higher pressure. In this fiigure, gas pressure is lower than liquid pressure in a), and gas pressure is higher than liquid pressure in b) (after Lu and Lkios, 2004).

The geometry of the meniscus is controlled both by the liquid-gas interaction (surface tension) and the solid-liquid interaction (contact angle). At equilibrium, the system will minimize energy, yielding a spherical (circular) geometry. The tension in the interface occurs due to the unbalanced molecular forces acting on the surface molecules, yielding a resultant force acting in the direction of the bulk liquid. Additionally, when there is attraction between the liquid and solid phases, an additional force is applied to the gas and liquid surface of the meniscus, resulting in a lower fluid pressure in the meniscus, causing the pore gas pressure to exert a force perpendicular to the meniscus.

Consequently, the ultimate tensile strength that can be developed is influenced by the liquid and solid attraction, as well as the interfacial properties between the liquid and the gas phase. The solid to liquid attraction exerts the tension that results in a lower fluid pressure, and if this tension is greater than the liquid-to-liquid molecular attraction, cavitation of the pore fluid will occur.

In coastal areas with saline pore fluid or in areas where the application of de-icing compounds is necessary, dissolved salts can be present in the pore fluid of unsaturated coarse-grained soils. The presence of these salt ions can result in temporary cementation once desiccation occurs. Salts dissociate freely in water, resulting in an increase in the ionic concentration of the pore fluid within the soil matrix. The dissolved ions bind water within a hydration sphere, and provide additional attractive forces between the water molecules that increase the liquid-to-liquid attraction along the liquid-to-gas interface, resulting in an increase in the surface tension in water with high concentrations of salt. However, as evaporation of the pore fluid occurs, the number of water molecules available to solubilize the salt ions decreases, and the salt will precipitate once saturation has been reached. If the attraction between the water, salt, and solid is strong enough to prevent the vaporization of water molecules, a stable salt water solution will remain until energy is added into the system in the form of heat, to break these bonds.

This thesis investigates the behavior of partially saturated particulate materials interacting with a variety of fluid types. Variables within the investigation included the hydrophobicity of the solid surfaces, the ionic concentration within the pore fluid, and the effect of particle packing on the behavior of fluid interfaces in a coarse-grained soil

packing. Consideration will be given to the effect these variables yield on the attractive forces at particle to particle contacts.

Chapter 2

LITERATURE REVIEW

2.1. Saturation stages

Unsaturated soils exhibit two primary stages of saturation: the funicular stage which is characterized by penetration of a gas phase into a previously saturated soil, followed by the pendular stage, which occurs as the previously connected water phase becomes discontinuous, leaving a thin water coating on soil particles, and pore space that is predominately occupied by the intruding gas phase (Cho and Santamarina 2001). As the water phase in a particulate medium is displaced by an intruding gas phase, tensile stress or suction may develop between two particles that are connected through a water meniscus. The tensile strength that develops between the particles can be attributed to two primary mechanisms, the water-to-particle surface attraction and the pressure difference between the water in the meniscus and the air phase (Cho 2001; Cho and Santamarina 2001; Lu et al. 2007).

In geotechnical engineering, a soil water characteristic curve (SWCC) is used to convey the constitutive relationship that describes the relationship between the amount of pore water in a system and the reduction in potential (Lu and Likos, 2004). At low values of water content, the suction within the soil matrix is high, and water will occur as a thin film coating on the soil particles, with short range adsorption forces acting as the dominant mechanism of suction within the soil. However, at higher values of water content, the soil particles will experience lower values of suction, when capillarity, which is controlled by pore structure and size, becomes the dominant mechanism of suction.

The developed SWCC is unique to a soil type and will be a function of multiple factors including the soil's surface area, pore size distribution, grain size distribution, density, organic material content, clay content, and mineralogy. Typically, a fine-grained soil like a clay will require large quantities of water to form a sorbed water layer, while capillarity will be the dominant mechanisms for a coarse-grained soil like a sand. In general usage, the SWCC is divided in to three primary regions (Figure 2-1): 1) tightly adsorbed regime, characterized by low water content, high suction, and water retention through microscale bonding mechanisms; 2) adsorbed film regime with low water content and thin film adsorption (electric field effects, dispersion forces, exchangeable cation hydration); and 3) capillary regime with high water content and surface electrical effects no longer exerting a strong influence (Lu and Likos, 2004).

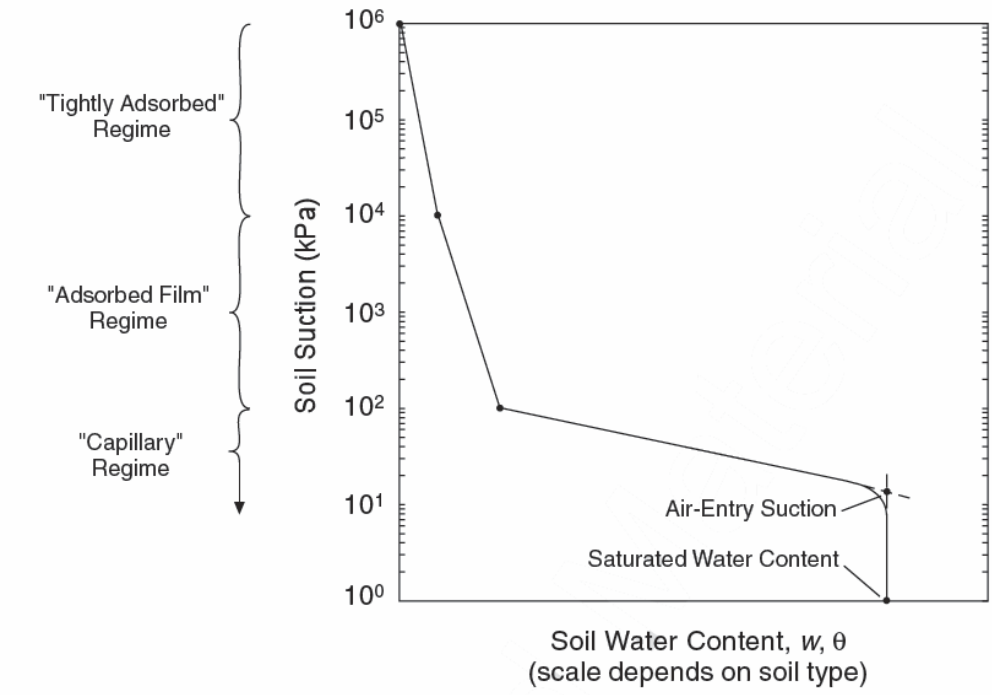

Figure 2-1. Soil suction regimes of the SWCC curve as a function of water content (figure from Lu and Likos, 2004).

2.2. Effective stress in unsaturated soils

Soils are particulate materials, with strength that is governed by the effective confining stress. Because the effective stress represents stress carried by the soil skeleton, it controls the behavior of the soil mass. In saturated soils, the effective stress has been defined by Terzaghi (Budhu 2007; Cho and Santamarina 2001; Mitchell and Soga 2005; Santamarina 2003):

$$\sigma' = \sigma - u_w$$

Where σ = total stress = stress due to the weight of all the soil and water above the point of interest, u_w = pore water pressure, and $\sigma' = \sigma - u_w$ = effective stress.

In 1959, Bishop proposed a modified version of the effective stress equation to account for unsaturated soils:

$$\sigma' = (\sigma - u_a) - \mathrm{X}(u_a - u_w)$$

Where u_a = pore air pressure and X = experimentally derived parameter which varies as a function of degree of saturation (0 in the dry state and 1 in the saturated state) (Cho and Santamarina 2001; Lu and Likos 2004; Lu and Likos 2006). This equation is an oversimplification of the complex and diverse particle level actions taking place throughout the soil. While the Bishop definition is the classic one, the method acts both on a local and fabric level and is unable to capture the full behavior of unsaturated soils, which means that it cannot be defined as a true effective stress (Cho and Santamarina 2001); consequently, additional definitions have been developed. More recently, the effective stress of unsaturated soils has also been defined as a quasi-effective stress, which is the sum of the net stress tensor and a suction associated tensor (Li 2003). Another definition is based on the concept of capillary stress (Hicher and Chang 2008).

However, because the fluid pressure in the menisci can change depending the particle separation distance and the anisotropic distribution of the partially saturating fluid, neither of these equations take into account the particle packing geometry, which is important in anisotropic packings.

2.3. Menisci geometry

The shape of the meniscus between two soil particles is a function of the saturation of the porous media, and can be concave, convex, or flat. If the pressure in the water phase is greater than atmospheric pressure, the meniscus will assume a convex shape; if the pressure in the water phase is equal to the atmospheric pressure, the meniscus will be flat, while pressure in the water phase that is lower than atmospheric pressure will result in a concave meniscus. For the case of a concave meniscus, the lower pressure in the water phase results from the three phase interaction of the water, air, and soil particle surface (Lu and Likos 2004). Attraction of the water to the particle surface and the pressure differential results in a tensile force on the air-water interface; however, in order to maintain equilibrium and to prevent an increase in the area of the air-water interface, the pressure inside the meniscus water must decrease. This effect can be so pronounced that the pressure can drop until cavitation in the occurs in the water phase (Trevena 1984). The pressure differential between the air and water interface is the mechanism driving the tensile force on the interfacial membrane, which in turns exerts an attractive force between two particles bound by the meniscus.

Moving from a state of high water content to lower water content in air-water systems, a meniscus that is initially convex will change shape due to equilibration between the fluid pressure and atmospheric pressure. The convex meniscus will assume

a flat geometry, with an increase in the radius of the meniscus as water drains toward the interface between the particles. Ultimately, as evaporation continues, the surface radius will decrease and the meniscus will become concave, and can be modeled in the pendular regime (Figure 2-2). Continued shrinkage of the concave meniscus will result in a decrease in water volume, and the wetted contact area between the particle and the water in the meniscus decreases. Simultaneously, as the radius of the meniscus and gas/water interfacial surface area decreases, the water pressure in the meniscus must also decrease, resulting in an increased difference between the meniscus water pressure and the atmospheric pressure, which in turn results in a larger tensile force between the two particles. The magnitude of the increase in force due to the decrease in water pressure is always greater than the magnitude of the decrease in force due to a reduction in particle and meniscus contact area, resulting in the observed increase in tensile force as the saturation of a particulate media is decreased.

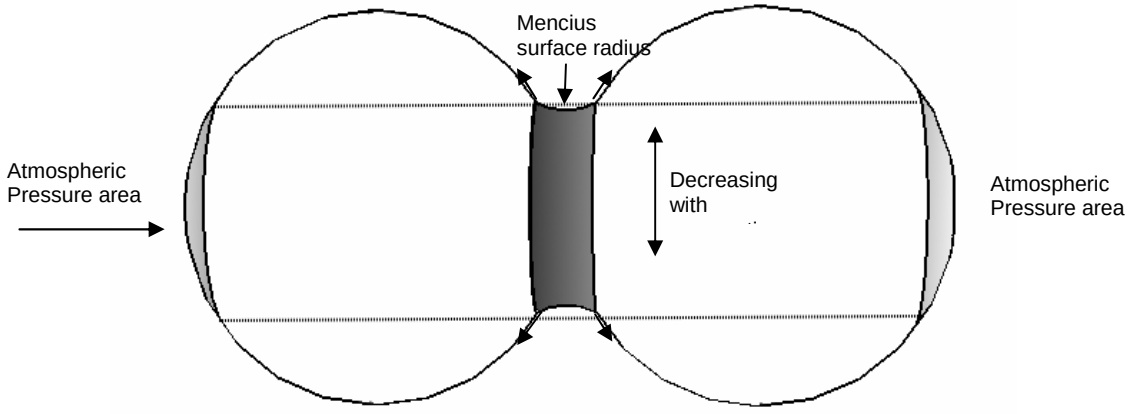

Figure 2-2. Menscius evaptionation between two sperhical particles; note the decreasing area over which the unbalanced atmospheric pressure acts.

The pore air pressure acts isotropically on the soil particles; however, the pressure force on the projected area of the meniscus labeled as atmospheric pressure area as seen in Figure 2-2 is now unbalanced due to the lower fluid pressure in the water meniscus. As a result, the component of the resultant pressure force acting normal to the meniscus is the magnitude of the tensile force (matric suction) between the particles.

If the soil particles have a flat, platy geometry, as would be the case for many clay minerals, the geometry of the meniscus will be somewhat altered. Assuming an equal separation between the two particles, the thickness of the meniscus will remain constant as evaporation proceeds (Figure 2-3), and the surface radius of the water meniscus will exhibit a much slower rate of decrease. Consequently, the surface area over which the pore air pressure is acting does not decrease as rapidly as in a system of interacting spherical or semi-spherical particles. Additionally, the volume of fluid between the two clay particles will be smaller than the volume between two sand particles, resulting in the ability to reach higher pressures without cavitation. Subsequently, the fluid is able to reach much lower pressures for interacting plate shaped minerals when compared to spherical particles, resulting in a much higher tensile force between the platey minerals (Chateau et al. 2002).

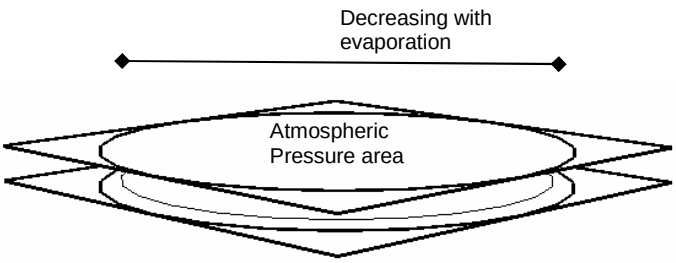

Figure 2-3. Menscius evaptionation between two platey particles, showing the area over which the unbalanced atmospheric pressure acts.

2.4. Particle packing

For assemblages of particles, the particle packing has a significant effect on the unsaturated behavior of the soil (Cho et al. 2006; Molenkamp and Nazemi 2003b). Typical packing geometries for uniform spheres illustrate a particulate material's tendencies toward volume change during shear (Figure 2-4) (Mitchell and Soga 2005). Densely packed soils (e.g., cubic tetrahedral, pyramidal, and tetrahedral) that exhibit dilative behavior under shear will exhibit reduced volume expansion when partially saturated, as the force causing dilation will have to overcome the tensile strength of the menisci that are stretched and broken in the transition to a less dense packing. However, because the menisci between contacts are mobile and do not have shear strength, only the menisci that are destroyed due to elongation during dilation will contribute resistance. In contrast, a loosely packed soil (e.g., simple cubic) with contractive tendencies will exhibit increased contractive behavior when the mensci between particles are in the partially saturated (pendular) state.

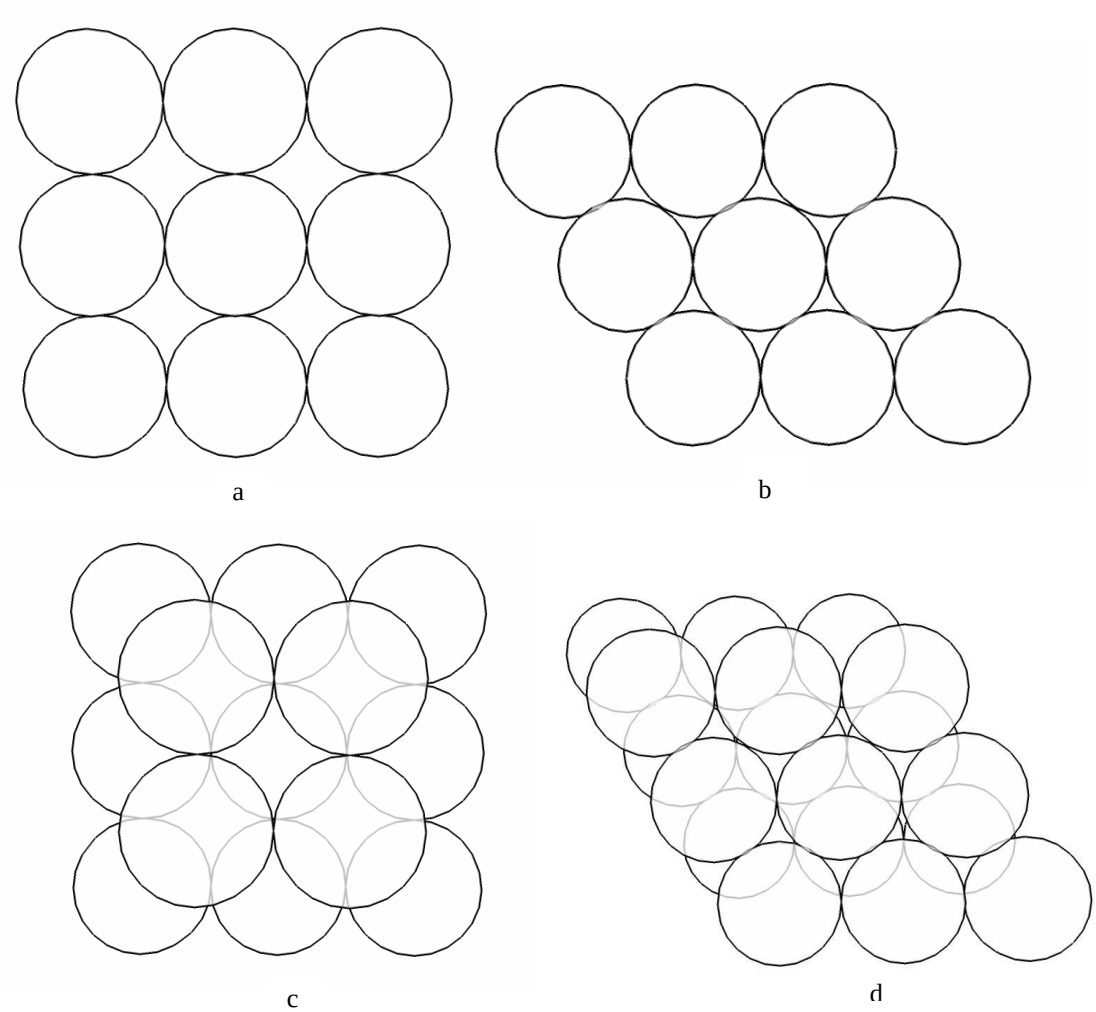

Figure 2-4. Ideal coarse-grained packings: a) simple cubic; b) cubic tetrahedral; c): pyramidal; d) tetrahedral.

2.5. Surface energy and water interaction

Surface energy is the excess energy on the surface of a material compared to the material as a whole. In a natural system such as water in air, excess surface energy is minimized, resulting in a rounded or spherical geometry, or hemi-spherical for a drop of water resting in air on a solid substrate. When a drop of fluid is at equilibrium at the air interface on the surface substrate, the following forces will be equilibrium, γ_{GL} (gas/liquid

tension or surface tension for air and water), γ_{LS} (liquid/solid surface tension or surface energy and water interaction), and the γ_{GS} (gas/solid surface tension) (Figure 2-5) (Barnes and Gentle 2005). When the drop is initially placed on the surface, the tension forces are not balanced, and the contact angle will not be at equilibrium. A net force will control until the interface reaches equilibrium and migration stops (Barnes and Gentle 2005; Israelachvili 1992; Kim et al. 2008):

$$F_h = \gamma_{GS} - \gamma_{LS} - \gamma_{GL}\cos\phi'$$

$$\gamma_{GS} = \gamma_{LS} + \gamma_{GL}\cos\phi$$

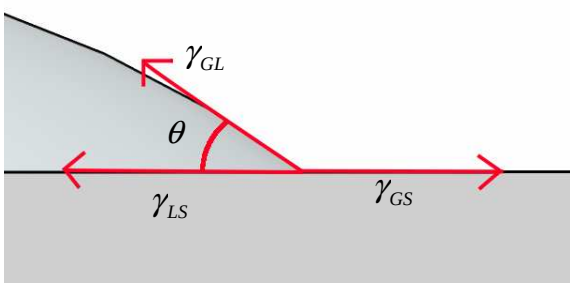

Figure 2-5. Governing forces operative at the gas/liquid/solid interface.

2.6. Properties of the solid substrate: silica

Silica (SiO_2) forms the fundamental building block for glass, the hydrophilic solid material of interest in this study. The surface charge of silica arises from pH dependent dissociation from the solid surface (Figure 2-6), and to a lesser extent from isomorphic substitution within the solid structure. Specifically, the source of the surface charge at silica surfaces (SiO_2) results from the pH dependent dissociation of the exposed silanol groups into water (Behrens and Grier 2001):

$$\equiv SiOH_2^+ \overset{k_1}{\Leftrightarrow} \equiv SiOH \overset{k_2}{\Leftrightarrow} SiO^- + H^+$$

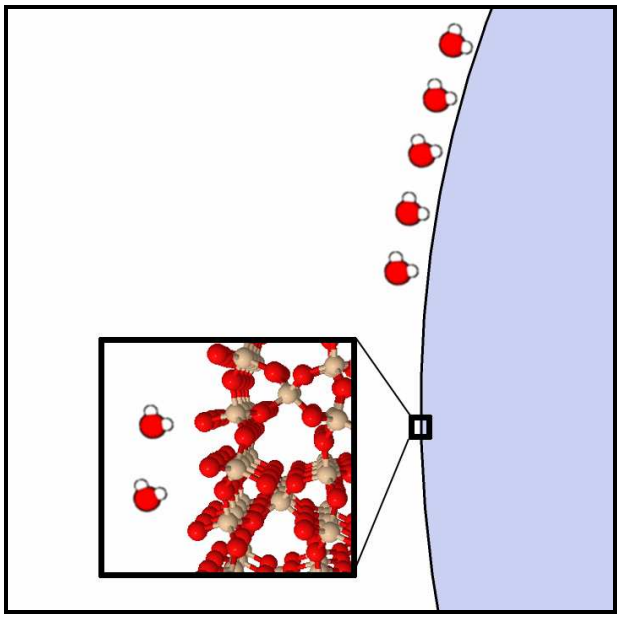

Figure 2-6. Orientation of the water molecules to the exposed silanol groups on the quartz surface (Iler 1979)

Silica exhibits a surface charge density of approximately -1 mC/m^2 at neutral pH, although the surface charge density is a function of both the ionic strength and the pH of the fluid medium (Figure 2-7).

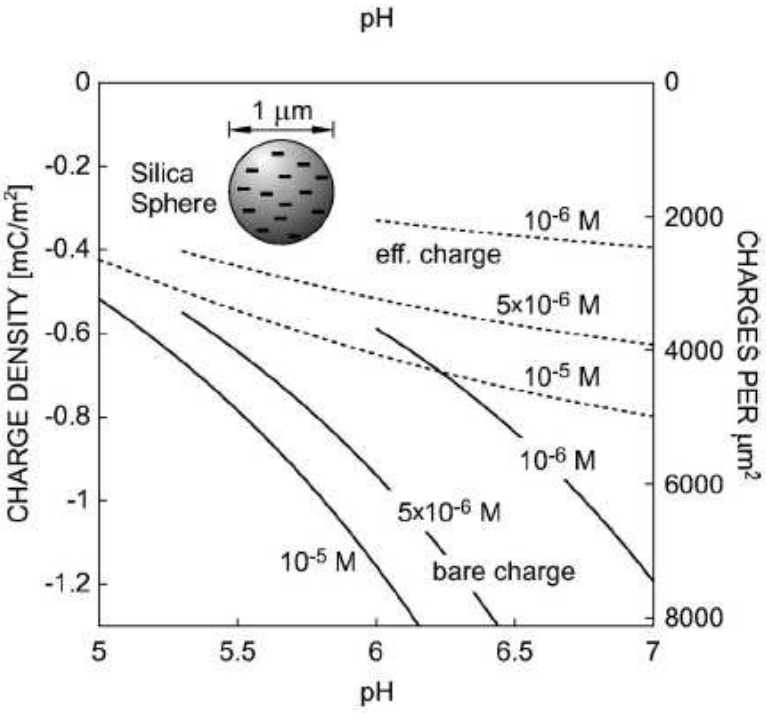

Figure 2-7. Charge densities of a 1 micron silica sphere with varing pH (firgure from Behrens and Grier 2001).

2.7. Properties of the solid substrate: polytetrafluoroethylene

Polytetrafluoroethylene (PTFE), more commonly known as Teflon, is a synthetic polymer consisting of a carbon backbone and covalently bonded fluorine atoms (C_nF_{2n+2}) (Figure 2-8). The bond strength in PTFE is quite high (482 kJ/mol), making it a relatively unreactive molecule that exhibits high corrosion resistance in extreme pH environments (Brandrup et al. 2005). Additionally, the high electronegativity of fluorine (3.980 pauline scale) reduces the induced dipole–dipole forces in non-polar liquids resulting in a hydrophobic, lipophobic, and fluorophilic behavior (Thompson et al. 2006).

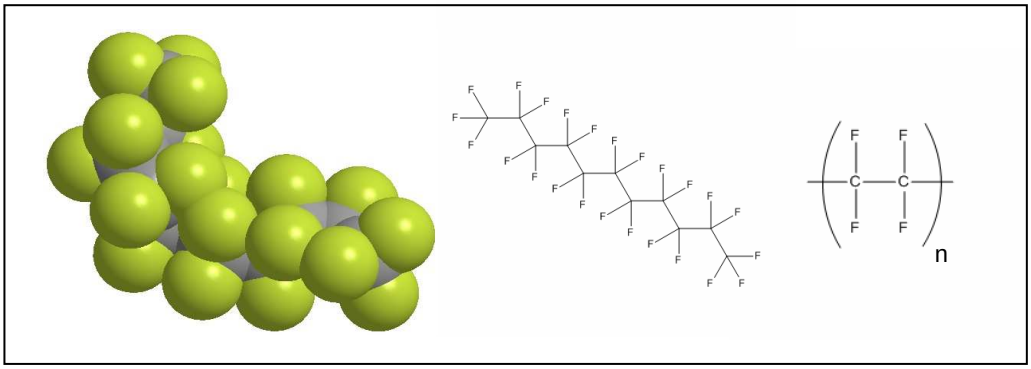

Figure 2-8. PTFE polymer and molecular structure.

2.8. Contact angle

The contact angle is the angle of the liquid and vapor interface at their intersection with a solid surface. The contact angle is controlled by, and indicative of, the fluid/solid interaction, or the attraction between the substrate surface and pore fluid. In turn, this attraction is a function of the surface charge and roughness of the solid, and the chemistry of the pore fluid (McHale et al. 2007a). The contact angle between the pore fluid and the substrate surface influences the behavior of the interparticle forces and pore fluid retention, and can be measured experimentally from a side profile of a droplet on the solid substrate (Figure 2-9).

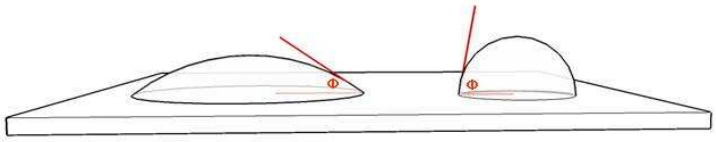

Figure 2-9. Visual location of the measured contact angle on two droplets with differing contact angles; hydrophilic versus hydrophobic.

All soils, including coarse-grained soils, can experience a change in hydrophobicity due to the deposition of a coating from human- or nature-initiated processes, such as fire volatized compounds, industrial spillages, and plant, fungi or microbial activity (Doerr et al. 2000). When a soil becomes more hydrophobic due to the presence of thin film coatings, it prevents capillary penetration, which in turn causes desiccation. Such desiccation processes contribute to increased erosion rates due to the lack of stabilizing vegetation, increased quantity of runoff, and flow velocity from the lowered frictional resistance (McHale et al. 2007b).

Contact angle hysteresis is the numerical difference in magnitude between the measured advancing and receding contact angles. The advancing contact angle results from a liquid advancing over a desiccated substrate surface, and will be larger than the contact angle of a drying liquid (receding contact angle). The contact angle is dependent on surface roughness and surface heterogeneity, and if the substrate surface has a thin water film due to pre-wetting by the previous moisture, the angle will be far lower than if the surface was desiccated (Mittal 2002). If the substrate surface is perfectly hydrophobic, then the angle for the advancing and receding will be very similar due to the surface not retaining a water layer as the liquid recedes.

The hydrophobicty of a surface can be additionally increased by altering the geometry of the surface interface independent of chemical modification (Drelich 2000). Surface roughness acts as an amplifier of surface hydrophobicity, increasing the contact angle and lowering the contact angle hysteresis. Super-hydrophobicity occurs when a hydrophobic surface chemistry is coupled with a rough surface having a small scale (1 - 10μm) geometry that entraps air (Quere 2002). Because of the small scale, surface

geometry wetting within the roughness is not possible, causing the surface fluid to lie on a patchwork of both solid and air. In these super hydrophobic conditions the typical contact angle is between 165˚ and 175˚ and the contact angle hysteresis is reduced to less than 10 degrees ($\Delta\theta < 10^{\circ}$). The reduction of the contact angle's hysteresis is likely due to the entrapped air inhibiting the surface from become wetted, resulting in reduced surface change from a receding contact angle (Nanotechnology and Interdisciplinary Research Initiative 2009).

2.9. Surface tension

Surface tension is a property of the surface of a liquid that causes the surface to behave as an elastic sheet. Surface tension only occurs at the air-water interface and is a result of the unbalanced intermolecular forces occurring on the surface of the fluid (Figure 2-10). When a salt is dissolved into water, the dissolved ions bind water within a hydration sphere (Figure 2-11), which provides additional attractive forces between the water molecules that increase the liquid-to-liquid attraction along the liquid-to-gas interface, resulting in an increase in the surface tension of water with increasing salt concentrations.

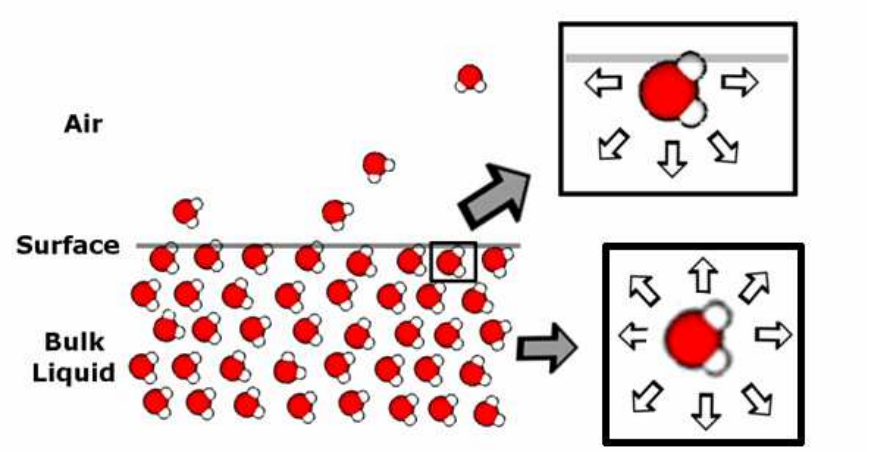

Figure 2-10. Simplified illustration of surface tension resulting from only the unbalanced forces acting on the molecules at the interface between the air and bulk liquid phases.

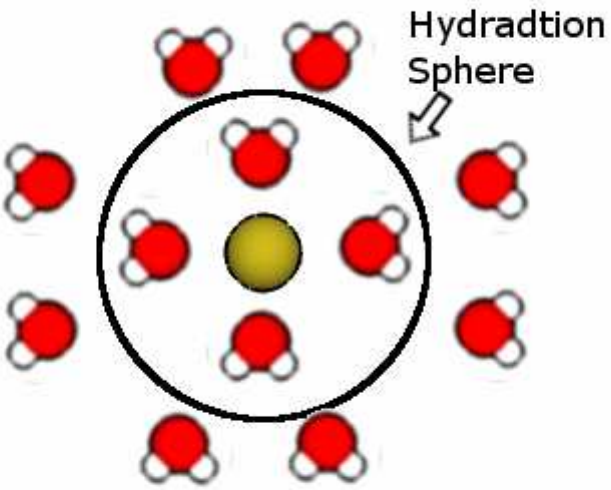

Figure 2-11. The alignment of the surrounding polar water molecules by their attraction to the positively charged ion, resulting in a hydration sphere.

2.10. Fluid phases with dissolved salts

In order to keep roads usable in the winter, many DOT's use sodium chloride or calcium chloride as a deicing compound because both salts lower the freezing point of water. Calcium chloride is beneficial in extremely cold environments, as it produces an exothermic reaction when it dissolves into water, and is able to draw moisture from the air, allowing it to start producing heat in extremely cold environments. However, sodium chloride is the most commonly used deicer as it is more readily available, less expensive, and does not require storage in a sealed environment (Wisconsin Transportation Bulletin 1997).

The deposited deicing salts can be transported off the road by runoff, splash, ploughing, and airborne transport. Most of the salt (seventy five to ninety percent) will pass into the roadside environment, and will be at least temporarily retained in the unsaturated vadaose zone of the soil (Green et al. 2008; Lundmark and Olofsson 2007). While ninety percent of the runoff salt will be deposited within 20 m of the road/source, elevated salt concentrations have been measured hundreds of meters from the original source (Blomqvist and Johansson 1999).

The salts that are retained in the pore fluid in the unsaturated vadaose zone will have an effect on the behavior of the soils present. If the soils are fine grained, the dissolved electrolytes will affect the double layer thickness, decreasing thickness as the salt concentration is increased. If there are electrolytes in excess of saturation, salt crystals can precipitate at the particle contacts yielding temporary cementation. In the case of coarse-grained soils, the presence of the additional cementation will contribute to a substantially altered stiffness of the soil matrix (Santamarina et al. 2001).

When water is in contact with a salt, dissolution of the salt occurs in three steps: first, the solute-to-solute attraction is broken, second, the solvent to solvent attraction is broken, and third, the solvent to solute attraction is formed (Figure 2-12) (Zumdahl 2003). The first two steps of dissolution are endothermic due to the breaking of the attractive forces, and the third step is generally exothermic. The heat of solution is the sum of the total heat change of the three stages of dissolution (Zumdahl 2003). The dissolution of NaCl is a slightly endothermic reaction (ΔH_{sol}=3.891 kJ/mol), while the dissolution of $CaCl_2$ is highly exothermic (ΔH_{sol}= - 81.3 kJ/mol). The endothermic reaction of NaCl dissolving in water draws heat from the fluid phase (e.g., ice cream made using rock salt), while the exothermic dissolution of $CaCl_2$ makes it a valuable deicer in extremely cold environments.

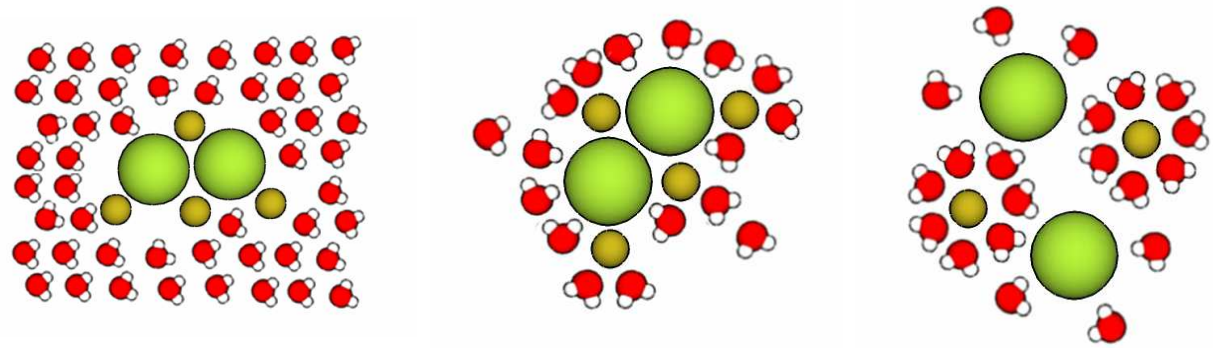

Figure 2-12. Three stages of salt dissolution: a) the solute-to-solute attraction is broken; b) the solvent to solvent attraction is broken; c) the solvent to solute attraction is formed.

The largest and most commonly studied effect of the presence of dissolved electrolytes occurs at the air/water interface; however, the solid/water interface is also influenced by electrolytes (Maheshwari et al. 2003). Increases in concentration of as little as 0.001 M resulted in measurable increases in the soild/water interfacial energy.

2.11. Vapor pressure and stability of calcium chloride solutions

The vapor pressure of a solution is a measure of the propensity of a substance to evaporate. At any temperature step, there is a pressure at which the gas of the substance is in dynamic equilibrium with its liquid or solid forms, known as the equilibrium vapor pressure (Zumdahl 2003). If a solution is at equilibrium vapor pressure based on the relative temperature and humidity, the flux of water into and out of the solution into the atmosphere will be equal, resulting in stable liquid solution.

Calcium chloride, which has a high vapor pressure at room temperature and standard pressure (Figure 2-13), is able to remain in a stable saturated calcium chloride solution, even after evaporation has removed excess water (Dow Chemical 2003). However, once the temperature increases to a threshold of 30˚C at standard pressure, precipitation will occur. Because calcium chloride is both a hygroscopic and deliquescent material, the salt is able to absorb moisture from its surrounding environment and dissolve back into a stable saturated calcium chloride solution, once the temperature is lowered below the precipitation threshold temperature.

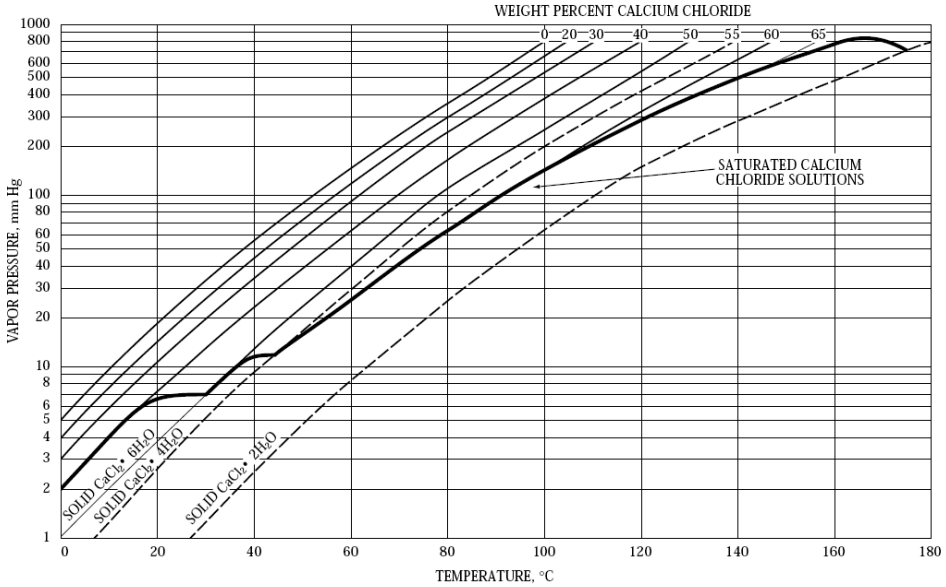

Figure 2-13. Vapor pressure of calcium chloride as a function of temperature and pressure (Dow Chemical, 2003).

Chapter 3

MATERIALS and METHODS

This experimental investigation examined the effect of the variables of solid phase hydrophobicity and fluid phase ionic concentration on the precipitation of salts and evaporation of water from coarse grain soil packings. The experimental matrix is documented in Table 3-1.

Table 3-1. Experimental Matrix

Measurement	***Phases***	***Variable***
Surface Tension	Air/Water	*Fluid Phase:* Deionized water NaCl (0, 0.125, 0.25, 0.5, 1.0, 2.0 M) $CaCl_2$ (0, 0.125, 0.25, 0.5, 1.0, 2.0 M)
Contact Angle	Air/Water/Solid	*Fluid Phase:* Deionized water NaCl (0, 0.125, 0.25, 0.5, 1.0, 2.0 M) $CaCl_2$ (0, 0.125, 0.25, 0.5, 1.0, 2.0 M) *Solid Phase:* Glass PTFE
Meniscus Evaporation – Visual	Air/Water/Solid	*Solid Phase:* Glass
Meniscus Evaporation – Mass Based	Air/Water/Solid	*Solid Phase:* Glass
Salt Precipitation	Air/Water/Solid	*Particle Packing:* 3 contact 4 contact *Fluid Phase:* NaCl (0.001, 0.5, 1.0 M) $CaCl_2$ (1.0 M) *Solid Phase:* Glass PTFE *Temperature:* $CaCl_2$ heated to >100 °C

3.1. Materials

Laboratory grade glass microscope slides and PTFE tape were used as the substrate for all experiments (Fisher Scientific). Soda lime glass beads (3 mm) and PTFE beads (3 mm) were obtained from Fisher Scientific and used after extensive cleaning. Laboratory grade hydrogen peroxide (H_2O_2, 3%), sodium chloride (NaCl), and calcium chloride

($CaCl_2$) were obtained from Fisher Scientific and were used as received. All water used in the experimentation was deionized (Barnstead Nanopure).

3.2. Methods

Contact angle measurements were performed using either a glass slide or a PTFE substrate. Each substrate was tested with deionized water, NaCl, and $CaCl_2$ solutions. Before measurement, the uncoated glass slides and PTFE substrate were cleaned by immersing in 3% H_2O_2 for approximately one minute, rinsed with deionized water, and subsequently dried with compressed nitrogen gas. Next, a 20 μl volume of fluid was placed on the test substrate for each given experimental condition. The drops were incrementally loaded on the substrate using a high performance liquid chromatography (HPLC) injection syringe and the final advancing contact angle was measured (Figure 3-1). For the advancing contact angle, a volume of 20 μl was added, and for the receding contact angle, a constant fluid volume of 5 μl was removed from the 20 μliters that was added originally. A digital image was taken of the profile of the final fluid configuration on the test substrate, taking care to place the fluid image in the center of the camera's focal plane (Canon digital camera, model A650). Approximately 5 μl of fluid was then removed, and another profile photo was captured in order to measure the receding contact angle. The images were analyzed using photo processing software (GIMP, version 2.4.6) in order to determine the contact angle between the interface of the fluid and the substrate.

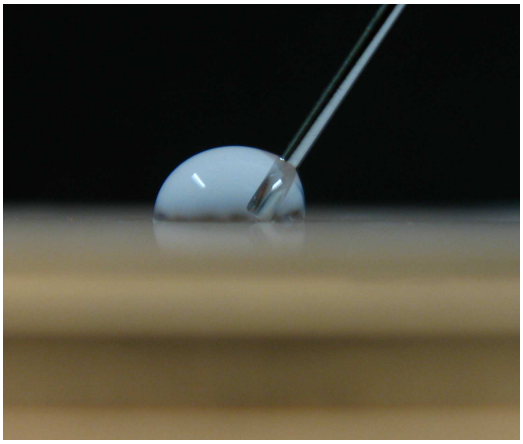

Figure 3-1. Injection of fluid for measurement of contact angle at air/water/silica interface.

Surface tension measurements (deionized water/air, aqueous sodium chloride solution/air, and aqueous calcium chloride solution/air) were performed with a surface tensiometer using the du Noüy method (Fisher Scientific, Surface Tensiomat). Before each series of experiments, the tensiometer was calibrated with a known mass. Before each reading, the platinum-iridium ring was cleaned by immersing into acetone followed by flash ignition with a propane torch. Each experiment was performed in triplicate, and the average was reported.

The crystallization of the salts from aqueous solution onto solid surfaces was observed as a function of evaporation rate, substrate hydrophobibcity, and particle packing. The particles being studied (soda lime glass or PTFE) were affixed to a glass slide substrate with a packing arrangement of either three or four contacts. The fluid (deionized water, sodium or calcium chloride solution) of interest was placed in the pore space, at the center of the each particle packing, taking care not to touch the underlying

glass substrate. Evaporation of the fluid and crystallization of the solid phase (salt experiments) was recorded using a series of time lapse images of evaporation for a given particle packing. Images were captured with an optical microscope (LEICA, MZ95, magnification 1-2x), in conjunction with time lapse control software (WinMacro, 1.2). Images were taken in 30 second time increments.

3.3. Packing model development

A series of experiments was performed to quantify the rate of evaporation of a water meniscus from the contact area between two adjacent particles. In order to apply the results of the two particle menisci evaporation to a three dimensional soil fabric, four types of coarse-grained packings were analyzed (Mitchell and Soga 2005). These packings assumed that all particles were uniform spheres, and were studied to yield insight into the coordination number and void space for different geometric arrangements. Packings studied included: simple cubic, cubic tetrahedral, pyramidal, and tetrahedral (Figure 3-2). To compare between packing types, each packing was reduced into its most basic unit of repeating structure. Because the units are repeating, they could be used to compute properties of a large uniform soil fabric simply by multiplying by the number of repeating units. This is similar to the representative elementary volume concept that has been used to analyze unsaturated pyramidal packing (Molenkamp and Nazemi 2003b).

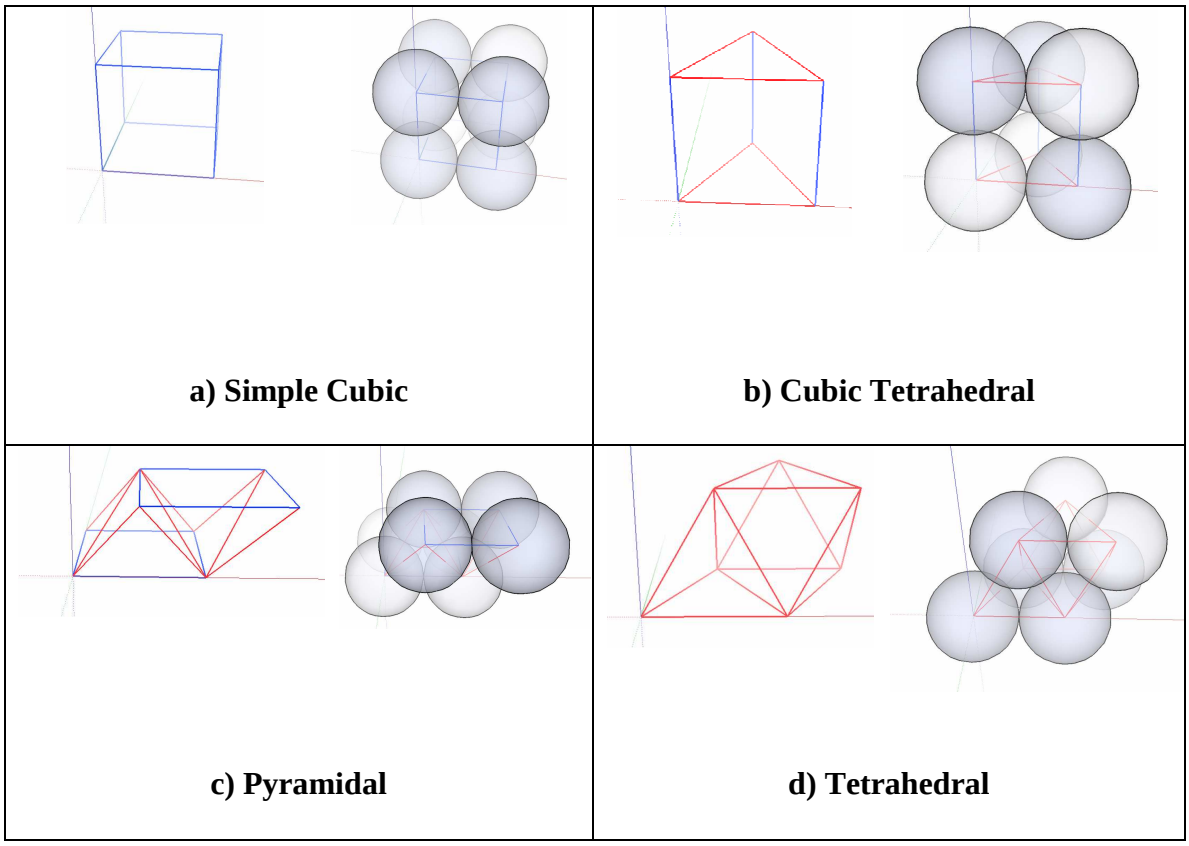

Figure 3-2. The four packing geometries modeled in this investigation.

Particle-to-particle contacts were represented as lines in the polyhedrons that define the structure of the repeating unit, and the particle contacts were represented by either two or three touching contacts between spheres (in the repeating unit). In Figure 3-2, the contacts with three spheres touching are represented in red, while the contacts with two spheres touching are represented in blue. The simple cubic packing represents an isotropic structure, while the remaining three packings are anisotropic (Lu et al. 2007).

3.4. Resultant force vectors for partially saturated soils

In the analysis, it was assumed that the fluid phase was uniformly distributed throughout the soil packing, resulting in menisci that were of uniform size; consequently, the tensile stress acting along the particle contact points would have the same magnitude

throughout the resulting fabric. Therefore, the only factor differing between particle packing geometries was the number and angle of the contacts. For each packing geometry, the three resultant force vectors were computed as the resistance if the polyhedron was pulled in one of the three principle axes (x,y,z).

Simple cubic. Because the simple cubic packing was an isotropic fabric, the resultant force vectors will be the same in the x, y, and z direction, and would be equal to $R_x = R_y = R_z = 4\sigma$, where σ = the tensile strength of water. This can be visualized by the contacts in tension marked in Figure 3-3. As a result, for any partially saturated coarse-grained soil that can be represented by spheres (including, but not limited to simple cubic), the total force required to pull the particles apart in tension can be computed by the stress at the contacts multiplied by the area and by the number of the repeating units in the fabric.

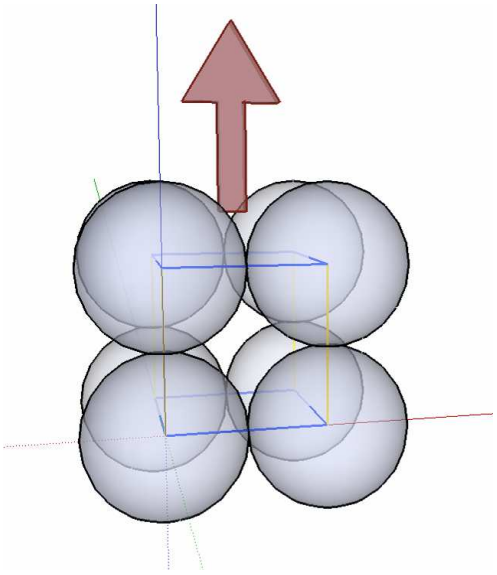

Figure 3-3. Visualization of menisci loading along vertical axis for a simple cubic packing.

Similarly, the fabrics for the remaining packing geometries can also be analyzed in terms of their resultant vectors:

Cubic tetrahedral. The resultant vectors for the cubic tetrahedral packing are:

$$R_x = 2 \cdot \sigma + 0 \cdot 3 \cdot \sigma + 4 \cdot \cos(60^\circ) \cdot \sigma = 4\sigma$$

$$R_y = 0 \cdot 2 \cdot \sigma + 0 \cdot 3 \cdot \sigma + 4 \cdot \sin(60^\circ) \cdot \sigma = 3.46\sigma$$

$$R_z = 0 \cdot 2 \cdot \sigma + 0 \cdot 4 \cdot \sigma + 4 \cdot \sigma = 3\sigma$$

Pyramidal. The resultant vectors for the pyramidal packing are:

$$R_x = 4 \cdot \sigma + 0 \cdot 4 \cdot \sigma + 9 \cdot \sin(45^\circ) \cdot \sin(45^\circ) \cdot \sigma = 8.5\sigma$$

$$Ry = 0 \cdot 4 \cdot \sigma + 4 \cdot \sigma + 9 \cdot \sin(45^\circ) \cdot \cos(45^\circ) \cdot \sigma = 8.5\sigma$$

$$R_z = 0 \cdot 4 \cdot \sigma + 4 \cdot 0 \cdot \sigma + 9 \cdot \cos(45^\circ) \cdot \sigma = 6.36\sigma$$

Tetrahedral. The resultant vectors for the tetrahedral packing are:

$$R_x = 3 \cdot \sigma + 5 \cdot \cos(60^\circ) \cdot \sigma + 5 \cdot \cos(30^\circ) \cdot \sigma + 0 \cdot 2 \cdot \sigma = 9.83\sigma$$

$$Ry = 0 \cdot 3 \cdot \sigma + 2 \cdot \cos(30^\circ) \cdot \sigma + 5 \cdot \sin(60^\circ) \cdot \sigma + 5 \cdot \sin(35.264^\circ) \cdot \sin(30^\circ) \cdot \sigma = 7.5\sigma$$

$$R_z = 7 \cdot \sigma \cdot \sin(54.575^\circ) + 0 \cdot 8 \cdot \sigma = 5.704\sigma$$

3.5. Coarse spherical grained soil polyhedron unit and pore space volume

Division of the packing into elementary representative units also allowed computation of void space, and approximation of water contents for the different packing geometries and saturation levels. Also, the water content at which the highest tensile strength is developed along a particular axis can be computed based on the number and geometry of the menisci formed in each packing. Finally, the model allows a dimensionless basis to compare the different packing arrangements (Table 3-2 and Table 3-3).

Table 3-2. Volume and Void Space Relationships for Studied Packings

Packing	Contacts/sphere	Unit Volume	Pore Space Volume
Simple Cubic	$12/8 = 1.5$	$= 8r^3$ 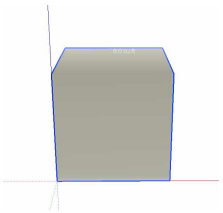	$= 3.93r^3$ 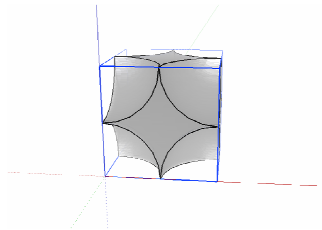
Cubic Tetrahedral	$10/6 = 1.67$	$= 3.46r^3$ 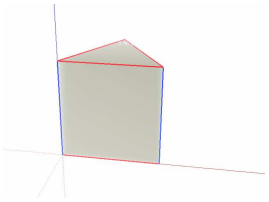	$= 1.43r^3$ 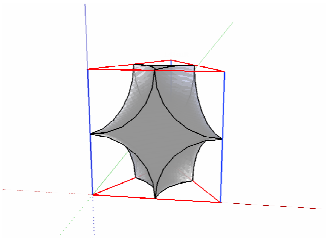
Tetrahedral	$15/7 = 2.14$	$= 4.71r^3$ 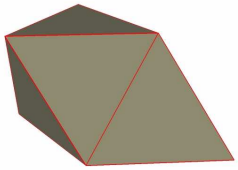	$= 1.36r^3$ 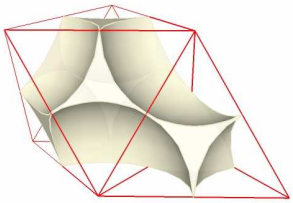
Pyramidal	$17/8 = 2.12$	$= 5.66r^3$ 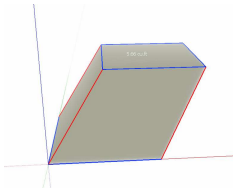	$= 1.59r^3$ 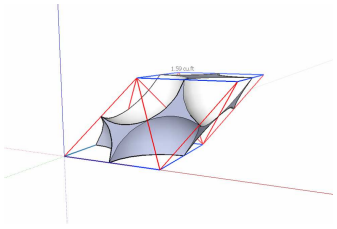

*Note: $Vol_{sphere} = 4/3\,\pi r^3$

Table 3-3. Porosity and Number of Menisci for Studied Packings

	Simple Cubic	Cubic Tetrahedral	Tetrahedral	Pyramidal
Porosity	0.49	0.41	0.29	0.28
Number of menisci	12	10	15	17

Chapter 4

RESULTS and ANALYSIS

4.1. Contact angle and wetting

The contact angle for an air/water/solid interface was measured as a function of dissolved salt concentration, interacting with either a hydrophilic glass substrate or with a hydrophobic PTFE substrate. Both the advancing and receding contact angles were measured on each substrate at concentrations of NaCl and $CaCl_2$ equal to 0, 0.125, 0.25, 0.5, 1.0, to 2.0 M (Table 4-1 and Figure 4-1). The advancing contact angles for deionized water interacting with clean uncoated glass and PTFE were 37.4° and 110.5°, respectively, while receding contact angles were 18.6° and 88.1°, respectively (Table 4-1). As anticipated, in all cases, the contact angles measured for the hydrophobic PTFE substrate were higher than those measured for the hydrophilic glass substrate, and all advancing contact angles were higher than the measured receding contact angle (Figure 4-2 through Figure 4-5). Although the data are scattered, comparison of the data in terms of salt concentration and ionic strength demonstrated that the presence of dissolved salt ions had a tendency to raise the contact angle on glass, while decreasing the contact angle on PTFE (Figure 4-6 and Figure 4-7).

Table 4-1. Advancing and Receding Contact Angles Measured on Glass and PTFE

Solution Phase	Salt Concentration (M)	Contact Angle Uncoated Glass		Contact Angle PTFE	
		Receding (°)	Advancing (°)	Receding (°)	Advancing (°)
De-I H_2O	0	18.59	37.37	88.07	110.51
NaCl	0.125	23.36	51.11	104.73	104.93
	0.25	18.67	45.75	76.65	98.75
	0.5	28.39	51.59	96.12	102.76
	1.0	19.27	42.27	93.90	109.61
	2.0	17.08	47.70	83.40	91.35
$CaCl_2$	0.125	17.38	41.05	101.23	105.80
	0.25	32.41	45.00	101.78	105.80
	0.5	8.92	37.73	85.06	106.58
	1.0	23.76	50.31˚	86.39	102.89
	2.0	27.67	45.69	80.60	106.53

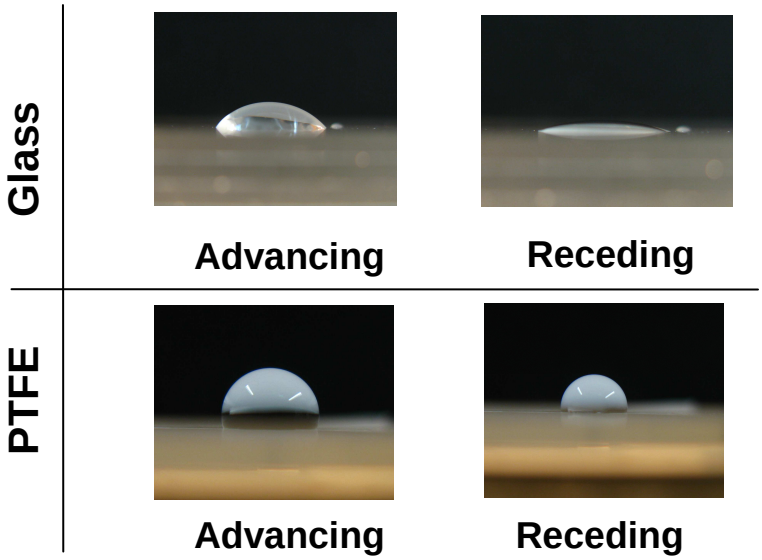

Figure 4-1. Contact angles measured at the air/water/solid interfaces for glass and PTFE.

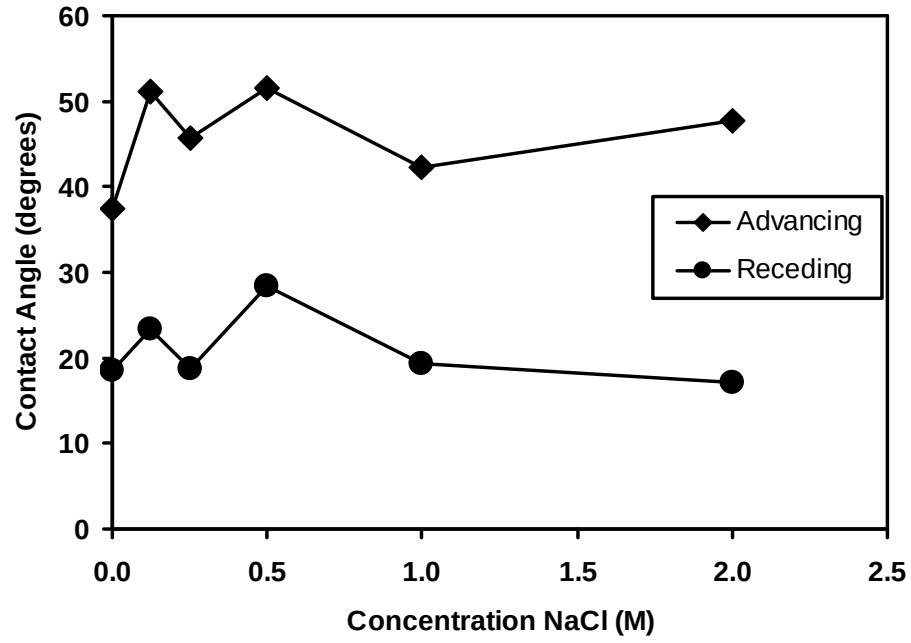

Figure 4-2. Contact angle on glass substrate, measured as a function of sodium chloride concentration.

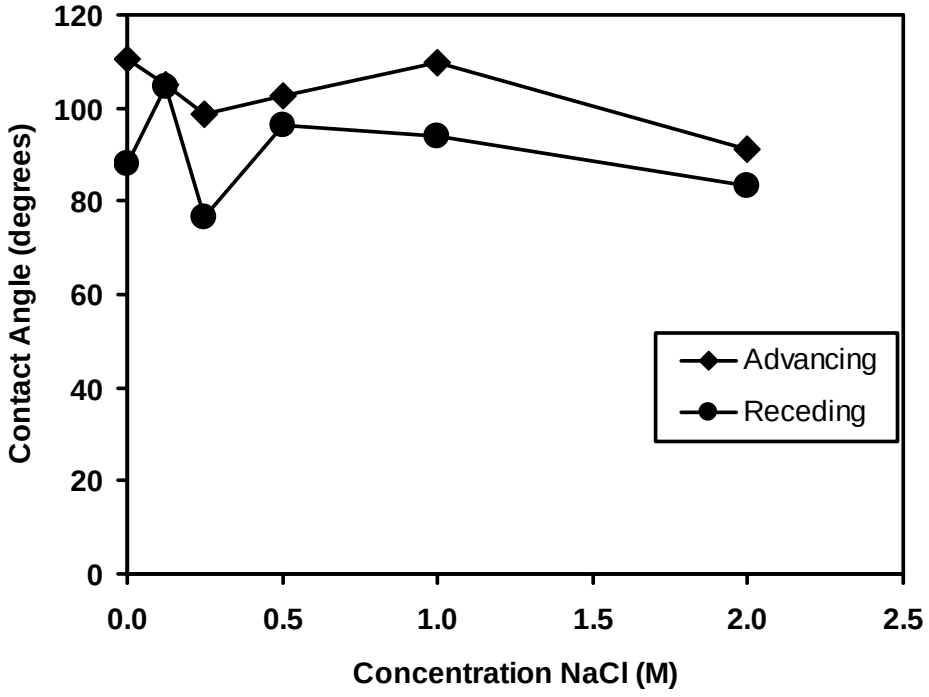

Figure 4-3. Contact angle on PTFE substrate, measured as a function of sodium chloride concentration.

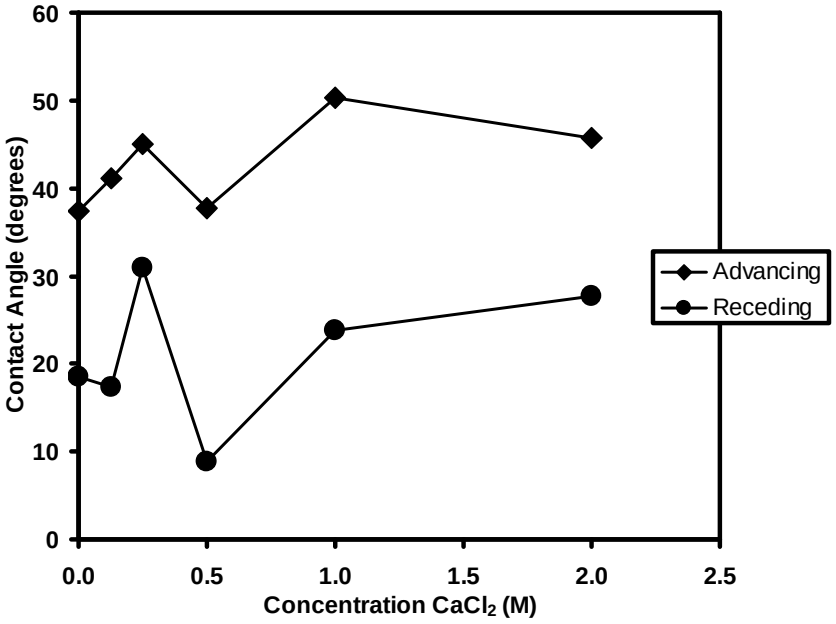

Figure 4-4. Contact angle on lime glass substrate, measured as a function of calcium chloride concentration.

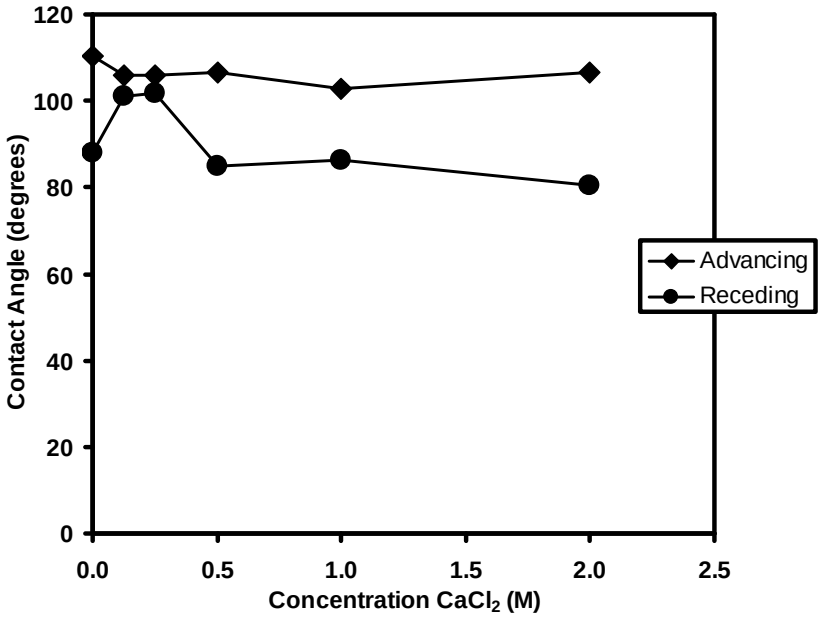

Figure 4-5. Contact angle on PTFE substrate, measured as a function of calcium chloride concentration.

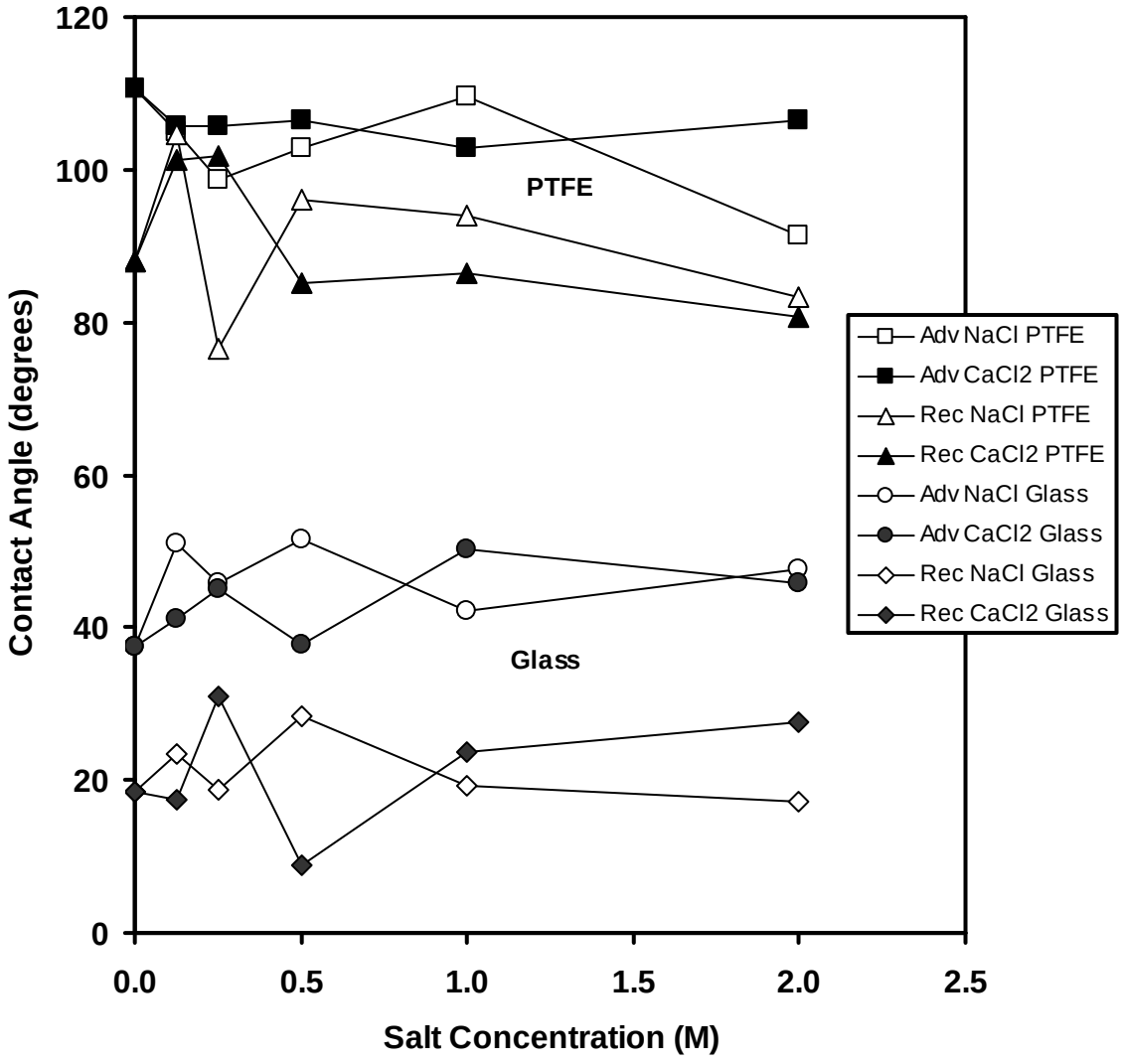

Figure 4-6. Measured contact angles as a function of salt concentration.

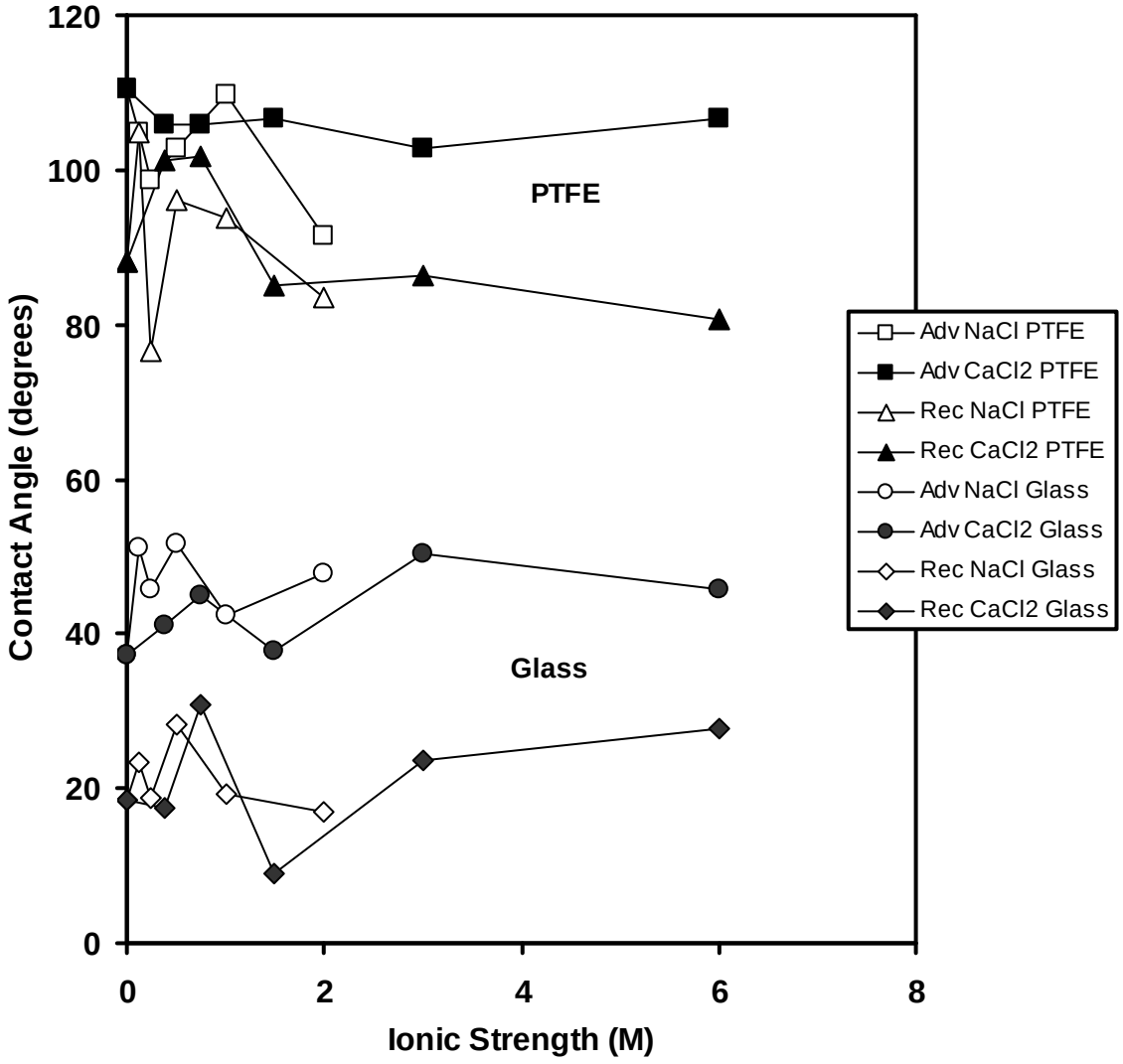

Figure 4-7. Measured contact angles as a function of ionic strength.

4.2. Surface tension

The surface tension of deionized water and aqueous solutions of NaCl and $CaCl_2$ was measured as a function of salt concentration (Figure 4-8). The surface tension measured for deionized water ranged from 74 – 76 dynes/cm, which agrees well with published literature values (Washburn 2003). For both salts tested, the surface tension

increased as the concentration of salt was increased, with an overall increase in the surface tension of 5-7%, when compared to deionized water. Differences in the initial surface tension measured in the two experiments resulted from temporal variation in the conductivity of the laboratory deionized water and ambient temperature.

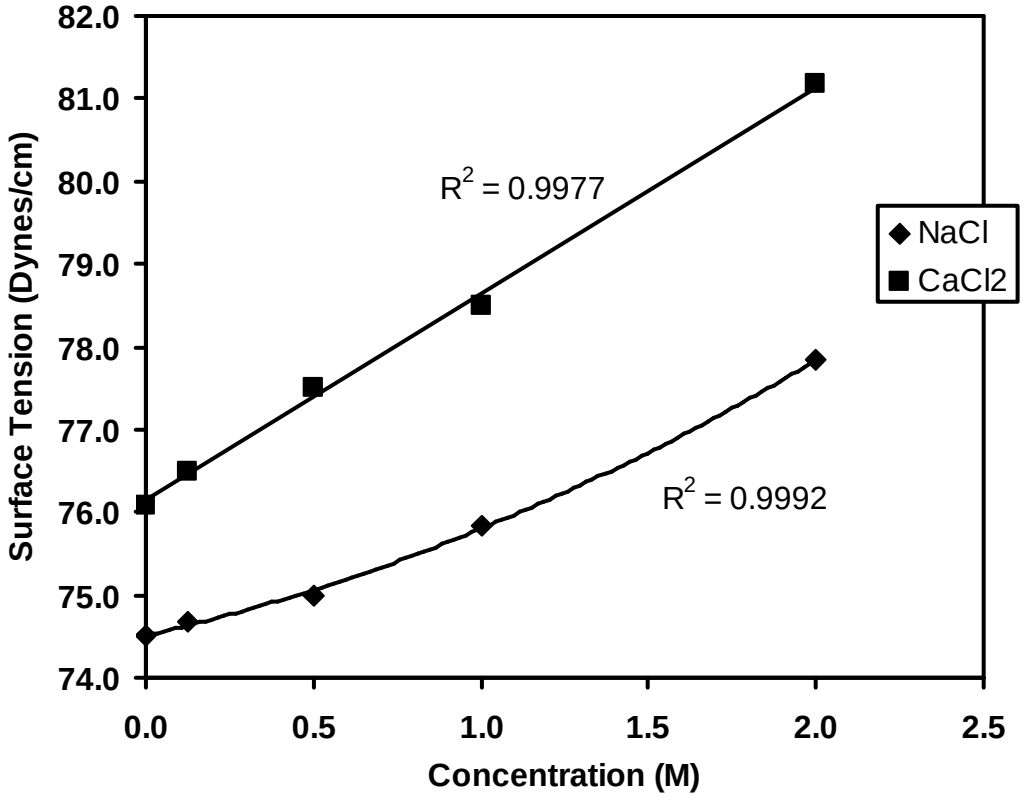

Figure 4-8. Surface tension at the air water interface, measured as a function of sodium chloride and calcium chloride concentration.

4.3. Meniscus modeling: optical analysis

An optical microscope was used to visually image an evaporating meniscus between two 3 mm glass beads in time increments of 1 minute. The images were then analyzed

using Gimp (version 2.6.6), a photo editing and analyzing tool, to measure the radius, thickness and length of the meniscus. The measured parameters were then used to fit an equation to predict the rate of change of the dimensions of the meniscus, including surface radius, thickness, and meniscus radius (Figure 4-9). For this model, a torus geometry was used, as literature has shown that this provides fairly accurate numerical results even though the correct geometry is closer to a catenoid (Cho and Santamarina 2001; Lian et al. 1993).

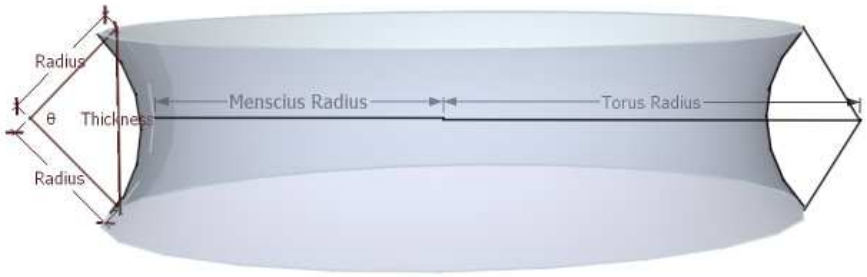

Figure 4-9. Geometry used to model the evaporating water meniscus.

The relevant geometric properties are as follows:

Surface area of torus=SA

$$\vec{R}(u,v) = [(tr + \cos(u)\cdot r)\cdot\cos(v),\cdot(tr + \cos(u)\cdot r)\cdot\sin(v), r\cdot\sin(u)]$$

$$\vec{R}_u = (\frac{dR}{du})$$

$$\vec{R}_v = (\frac{dR}{dv})$$

$$T = cross(\vec{R}_u, \vec{R}_v)$$

$$Norm = abs(\sqrt{(T_x^{\,2} + T_y^{\,2} + T_z^{\,2})})$$

$$SA = \int_{\pi-.5\theta}^{\pi+.5\theta} \int_{0}^{2\pi} Norm \quad | \, du \quad dv$$

Volume of meniscus=Vm:

$$twospherevol = 2 \cdot ((\pi \cdot (t/2)^2 \cdot rs) - (\frac{\pi (t/2)^3}{3})$$

$$mensciusvol = \pi \int_{-0.5t}^{0.5t} (r + mr)^2 - (\sqrt{r - x^2})^2 dx$$

$$Liquidvol = mensciusvol - twospherevol$$

Where:

$MenscuisRaduis = mr$
$Torusraduis = tr$
$Raduis = r$
$Thickness = t$

Angle of curvature:

$$\theta = \text{acos}(\frac{2 \cdot \text{r}^2 - t^2}{2 \cdot r^2})$$

4.4. Meniscus modeling: mass-based analysis

In addition to the optical measurements of meniscus evaporation, a highly sensitive balance was used to measure the mass of an evaporating meniscus between two 3 mm glass beads at time increments of 30 seconds, and the data were compared to the results from the optical experiments. While there were fundamental differences between the experimental setups, the overall trends in evaporation were similar in the two test procedures (Figure 4-10 and Figure 4-11). Also, a mass-based rate of evaporation rate of NaCl solution was compared to the rate of evaporation measured for deionized water

(Figure 4-12). As seen in the figure, the rate of evaporation from the salt water curve had two distinct slopes. The first slope was similar to that of the deionized water curve, as the concentration of salt was not yet at saturation. After complete salt crystallization, the evaporation rate decreased as the water pore fluid was attracted to the precipitated salt ions (Santamarina et al. 2001).

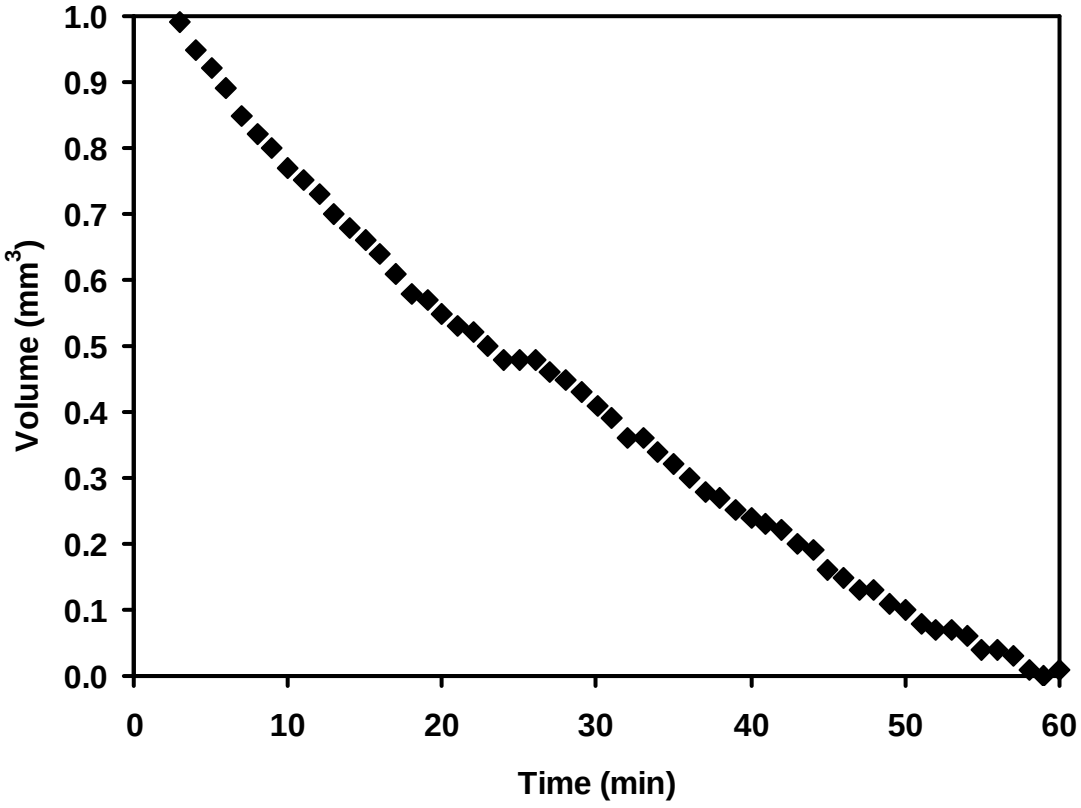

Figure 4-10. Meniscus volume change measurements based on measurements of mass (.00 mg sensenstivity) reduction due to evaporation.

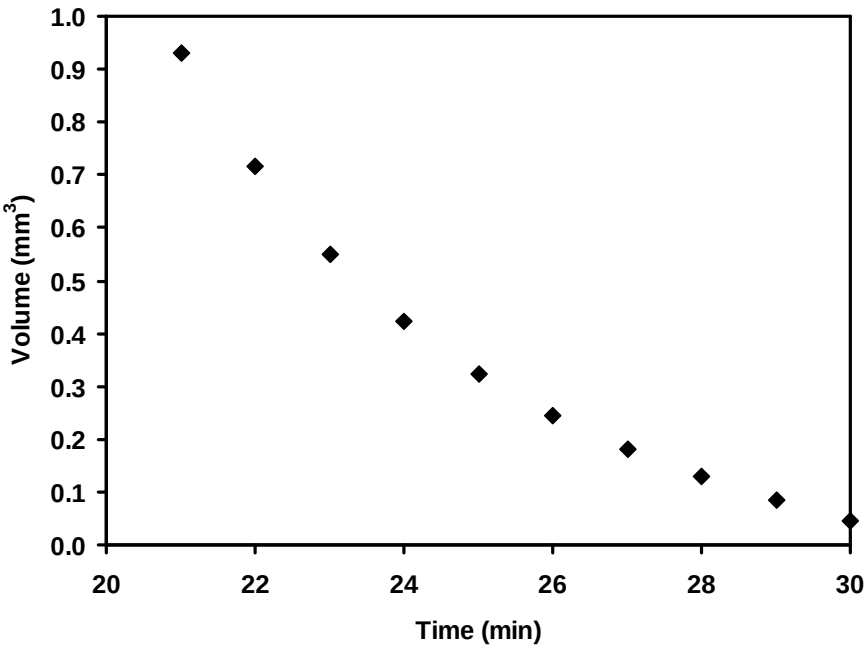

Figure 4-11. Meniscus volume change measurements based on optical imaging of the reduction of meniscus dimensions due to evaporation.

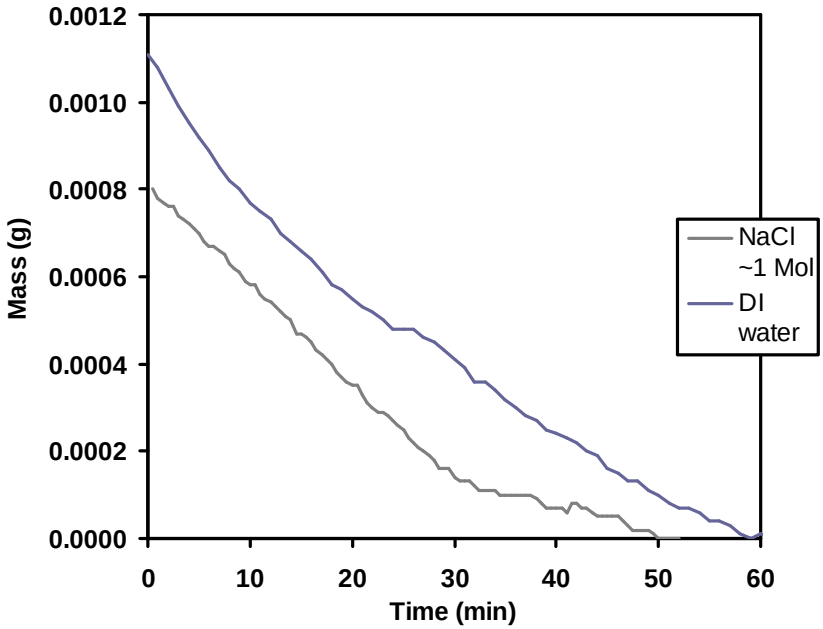

Figure 4-12. Rate of mass change for NaCl solution and deionized water menisci evaporation.

4.5. Empirical modeling of meniscus evaporation between two spherical glass beads

Matlab (version 7.5.0) was used to model the meniscus evaporation using the experimentally derived relationships for the meniscus thickness, radius and length (Figure 4-13 and Figure 4-14). With these parameters, the volume and surface area of the meniscus was computed at any desired time step, yielding changes in surface radius, thickness, and meniscus diameter as a function of time (Figure 4-15 through Figure 4-18).

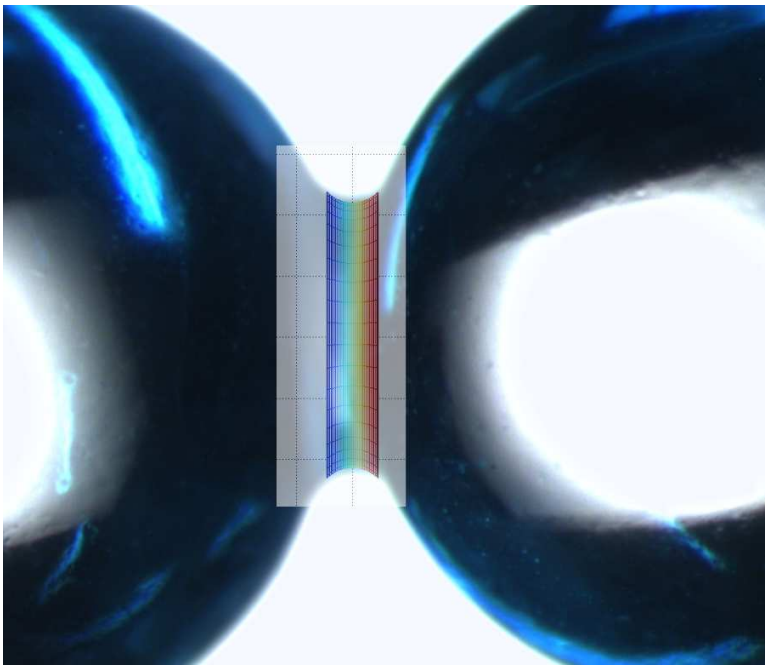

Figure 4-13. Optical image of meniscus during two particle evaporation experiment.

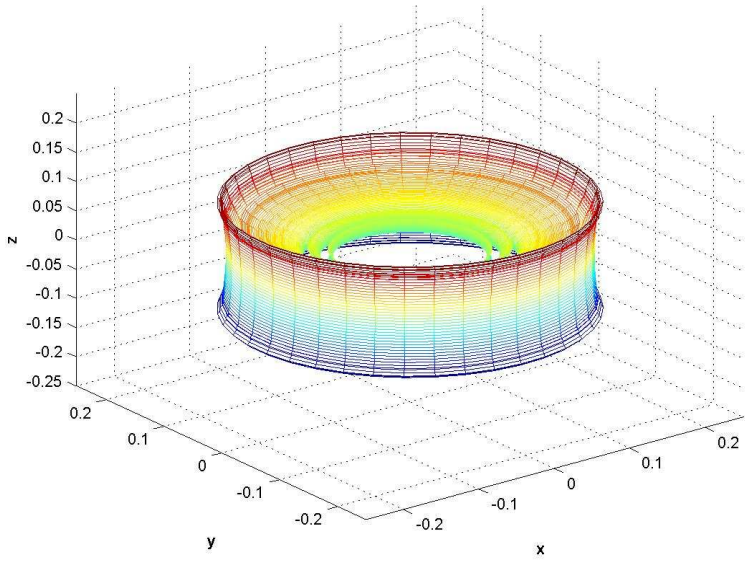

Figure 4-14. Empirical model developed from fitting experimental data with Matlab.

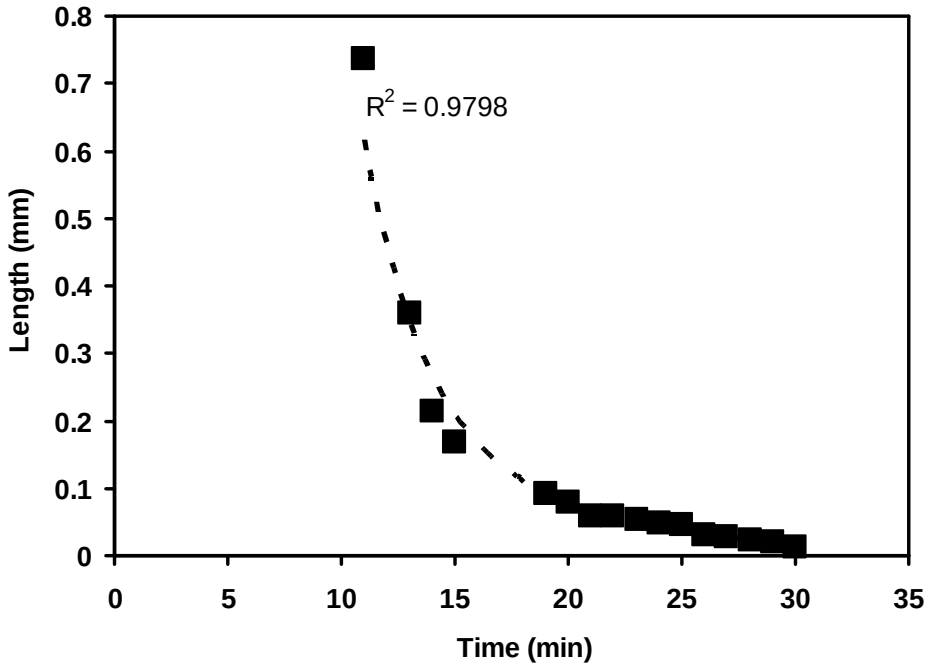

Figure 4-15 Curve fitting for meniscus surface radius.

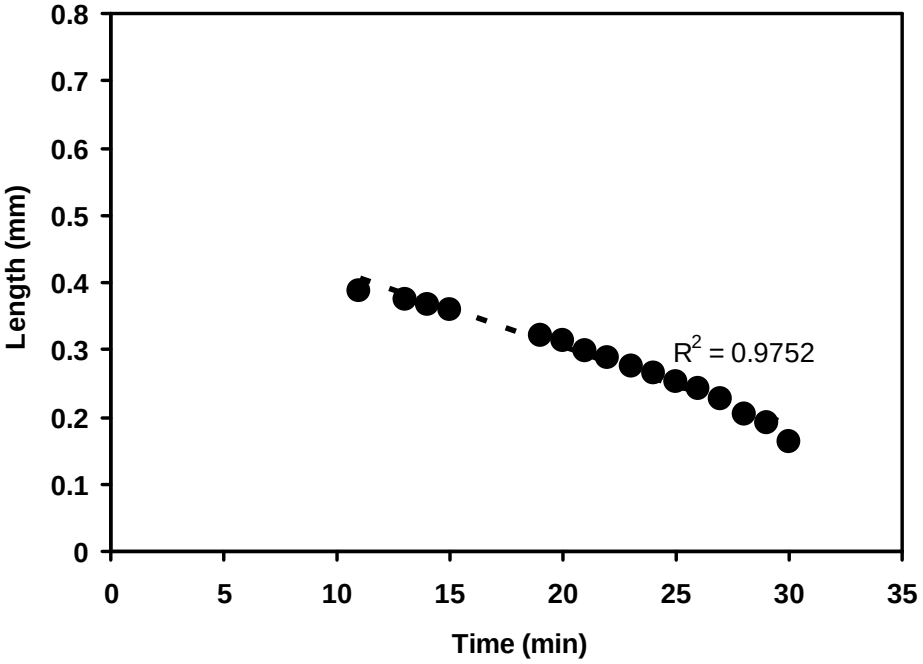

Figure 4-16 Curve fitting for meniscus diameter.

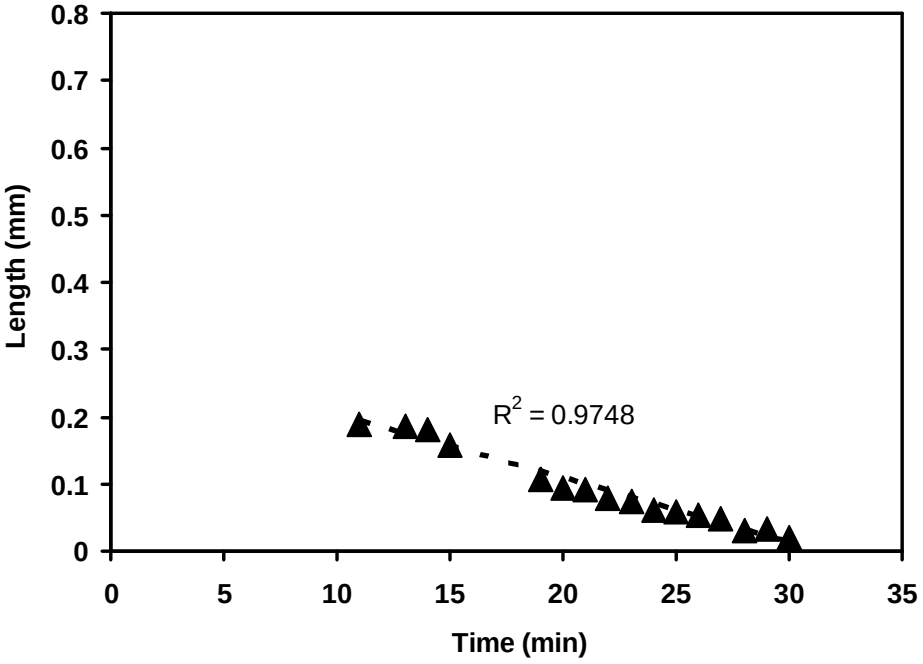

Figure 4-17. Curve fitting for meniscus thickness.

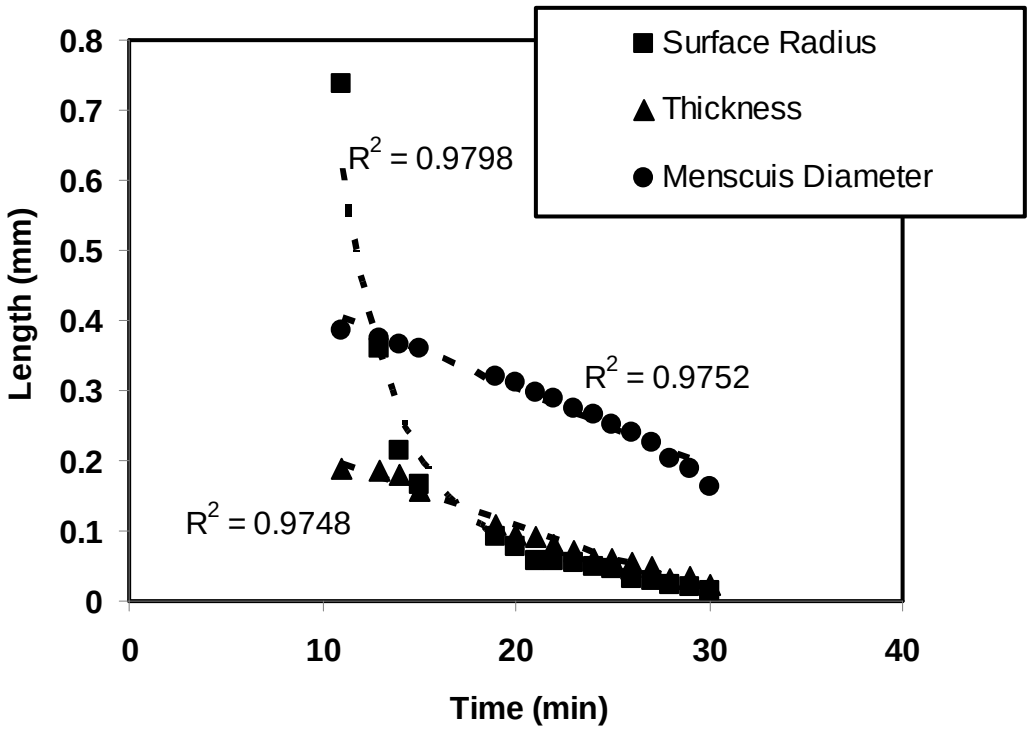

Figure 4-18. Curve fitting varibles combined.

Combining this model with Laplace's equation ($\Delta u = (u_a + u_w) = T_s\left(\frac{1}{r_1} + \frac{1}{r_2}\right)$),

facilitated the determination of the pressure difference $(u_a + u_w)$, and the development of the empirical soil water characteristic curve for a single menisci (Figure 4-19) (Lu et al. 2007). When this curve is combined into the resultant vectors for the individual packings, it yields the magnitude and direction of the tensile strength acting on the packing at any given uniform water content

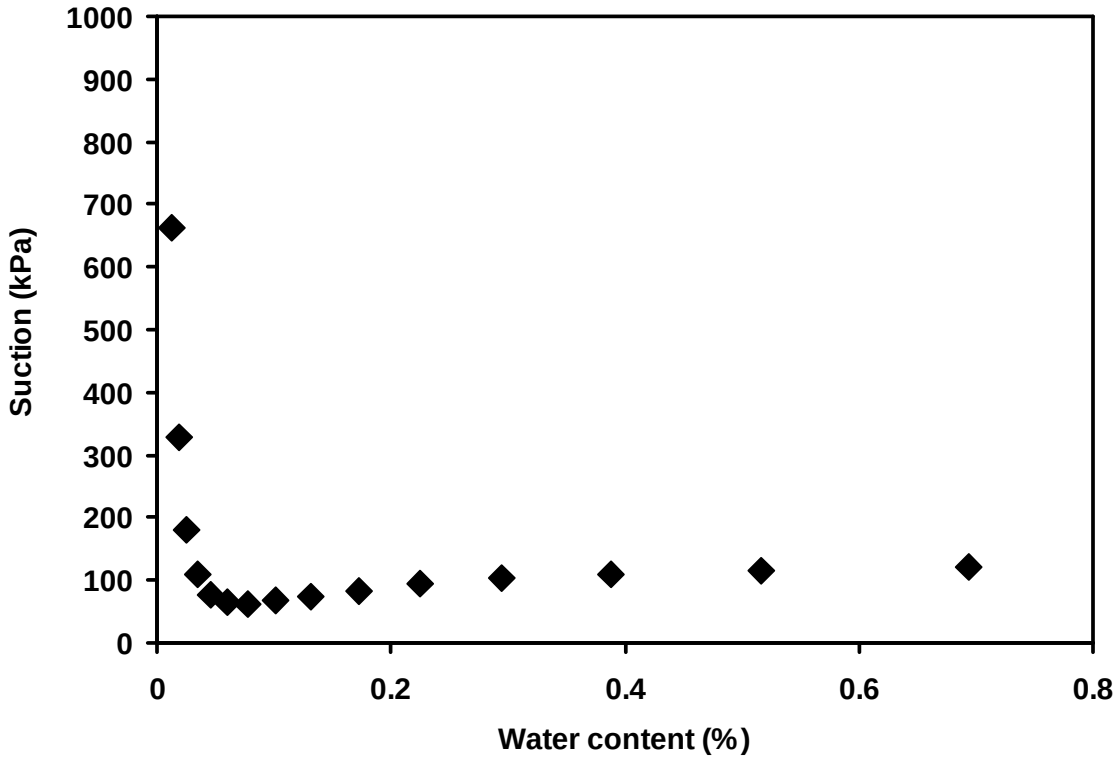

Figure 4-19. Empirical soil water characteristic curve for a single menisci based on evaporation rates determined in two particle evaporation study.

4.6. Salt precipitation and cementation

The pattern of salt precipitation (NaCl and $CaCl_2$) was measured in a three-sphere and four sphere packing geometry, using both optically based (Figure 4-20) and mass-based measurements on glass and PTFE beads (Figure 4-21 through Figure 4-35). Visual analysis of the NaCl salt precipitation patterns demonstrated that the salt initially precipitated along the air/liquid/solid interface of the meniscus where salt concentration would be highest due to rapid evaporation. Additionally, crystals that did not directly precipitate along the menisci boundary were eventually moved to the boundaries (and often displaced) due to meniscus shrinking by evaporation. Ultimately, the salts were

deposited at the particle interface as evaporation proceeded and the meniscus contracted, resulting in a light cementation. Due to the nature of this process, it can only occur in the pendular regime (Santamarina 2003).

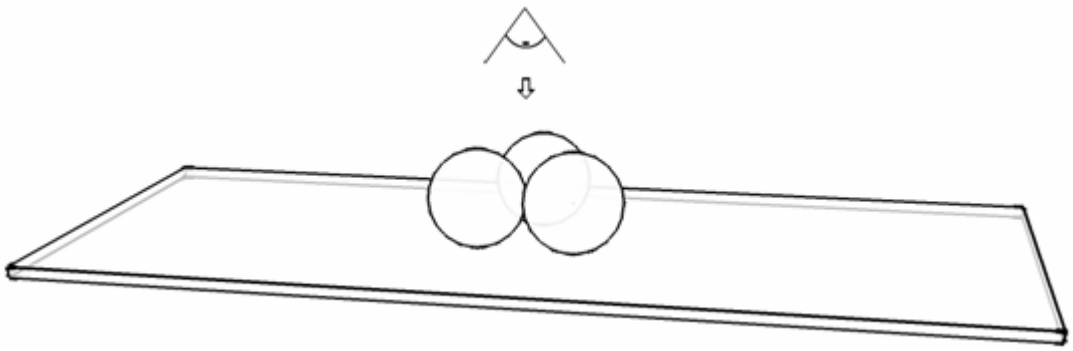

Figure 4-20. Configuration for optical observation of salt crystallization from fluid meniscus.

Starting from equal initial solution concentrations of salt, the crystallized mass was deposited relatively uniformly between particle contacts. As a result, the number of contacts controlled the mass of salt per menisci, which in turn controlled the amount of cementation and additional stiffness that would be developed per contact. Denser packings have a higher coordination number, resulting in a stronger packing, but with less cementation per contact. If the mass of crystallized salt that was deposited in a contractive and dilative packing was equal, the evaporation process would deposit more salt per contact on the contractive packings then the dilative packings due to the lower coordination number in the contractive packing. Ultimately, the orientation of loading and packing configuration would control how the salt crystal at each contact was loaded.

In a contractive packing (e.g., simple cubic) being loaded parallel to the cemented contact, the majority of the crystals would be in shear due to the 90˚ separation between contacts; however, in a dilative packing, the 60˚ separation would have a higher number of contacts, with less salt and a higher percentage of contacts in compression and tension than shear.

Increasing the concentration of NaCl in the pore fluid significantly influenced the crystallization pattern of the salt on glass. At low concentrations, the salt crystals precipitated primarily at the particle contacts (Figure 4-21 through Figure 4-26). However, as the NaCl concentration increased, the salt precipitated as a film, coating the particles away from direct particle to particle contact (Figure 4-27 through Figure 4-29).

In contrast, the crystallization pattern of NaCl on the hydrophobic PTFE surface was substantially different from that observed on glass (Figure 4-30 and Figure 4-31). Unlike the pattern on the glass beads where NaCl crystallized in a coating that diffused to areas were not initially wetted, the NaCl precipitated as a single crystal within the wetted perimeter of the meniscus on the PTFE. The crystallization pattern observed for NaCl on glass was likely due to the salt water migrating along the surface of the particle due to the increase in solid/water interfacial energy due to the presence of electrolyte ions (Butkus and Grasso 1998). However, for a hydrophobic material, such as PTFE, the NaCl solution was unable to migrate from the initial meniscus due to the low solid/water interfacial energy. As the initial meniscus remained relatively stationary, NaCl crystals formed monolithically and essentially in place when evaporation occurred (Figure 4-30 and Figure 4-31).

In deliquescent salts such as $CaCl_2$, crystallization can only occur if the temperature and energy are high enough to overcome the hygroscopic strength of the salt, and will not crystallize at standard laboratory temperature and pressure (Figure 4-32 through Figure 4-35). If the ambient temperature is below the minimum temperature required for precipitation, the solution will evaporate until the saturation is reached, and remain at equilibrium between the hygroscopic strength of the salt, and the temperature and pressure of the system. However, if the ambient temperature is raised above the precipitation temperature, then the salt crystallization will follow the similar behaviors as the non-deliquescent salts (Figure 4-36). Subsequent return to room temperature will be followed by reabsorption of moisture and an aqueous equilibrium (Figure 4-37).

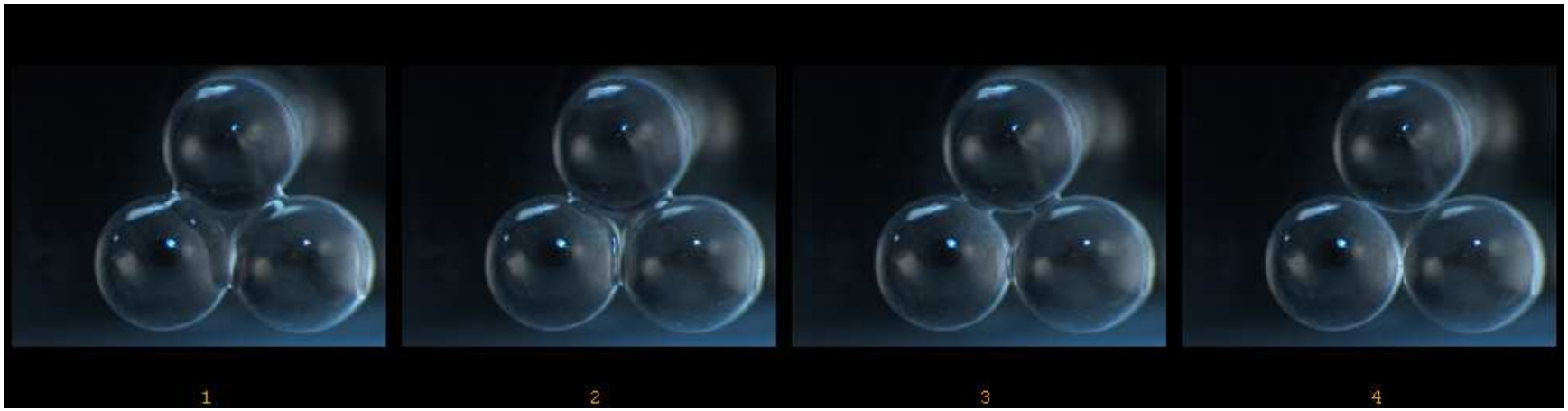

ΔT=10 min

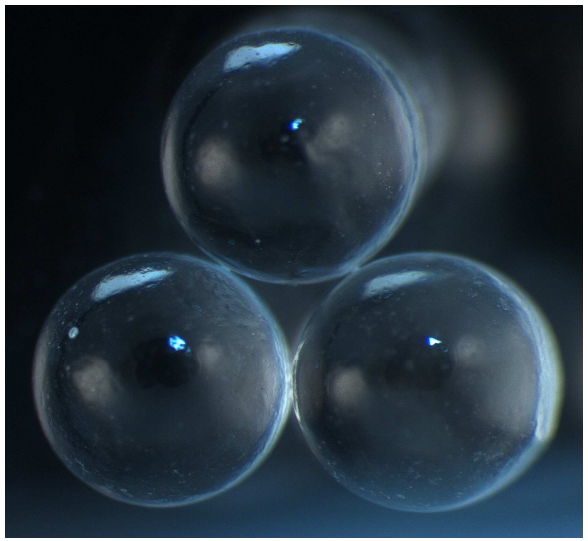

Figure 4-21. NaCl (0.0001 M) crystallization on 3 contact packing (soda lime glass, 3 mm diameter).

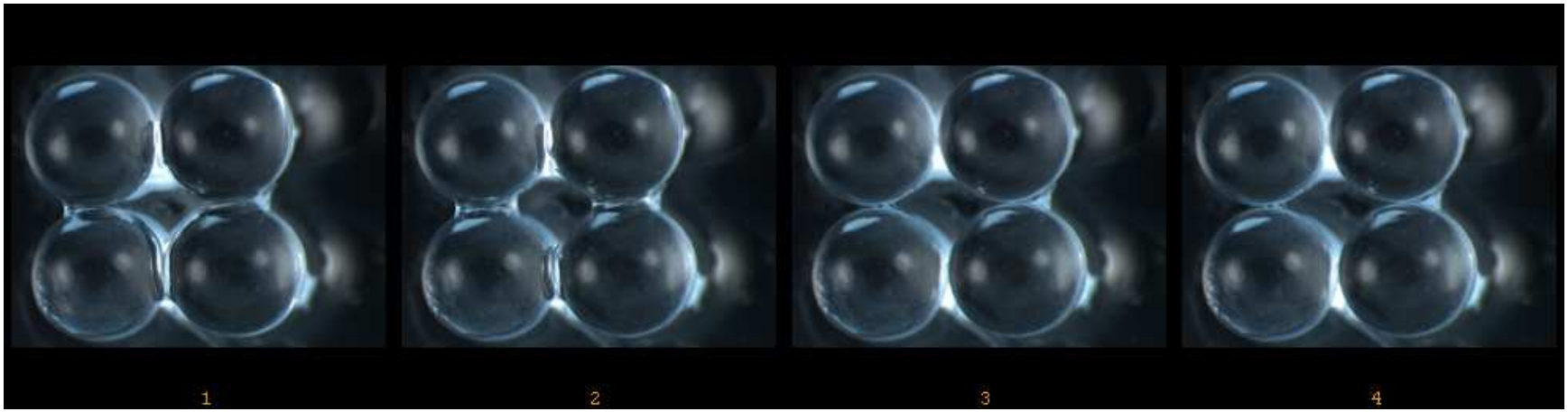

ΔT=10 min

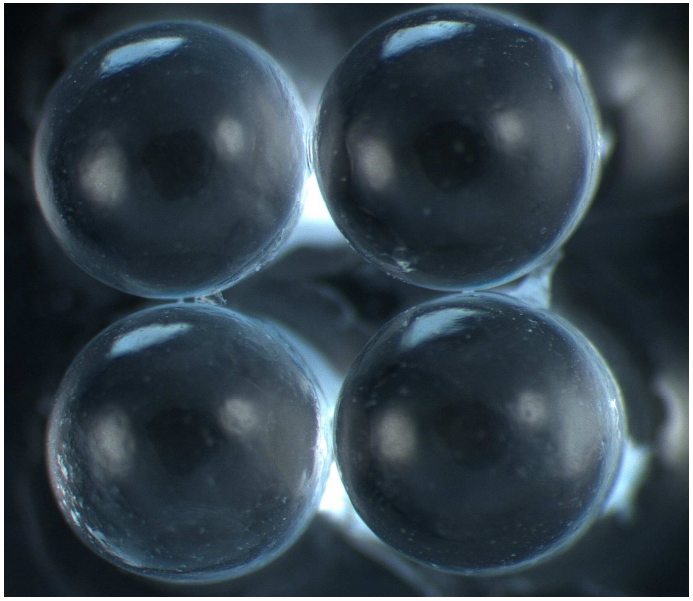

Figure 4-22. NaCl (0.0001 M) crystallization on 4 contact packing (soda lime glass, 3 mm diameter).

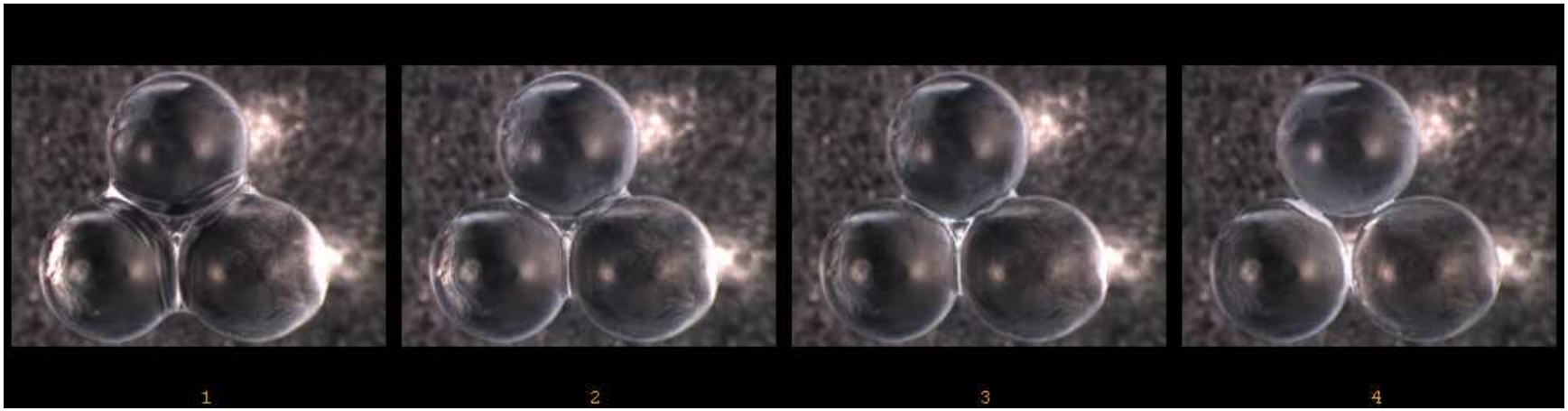

ΔT=20 min

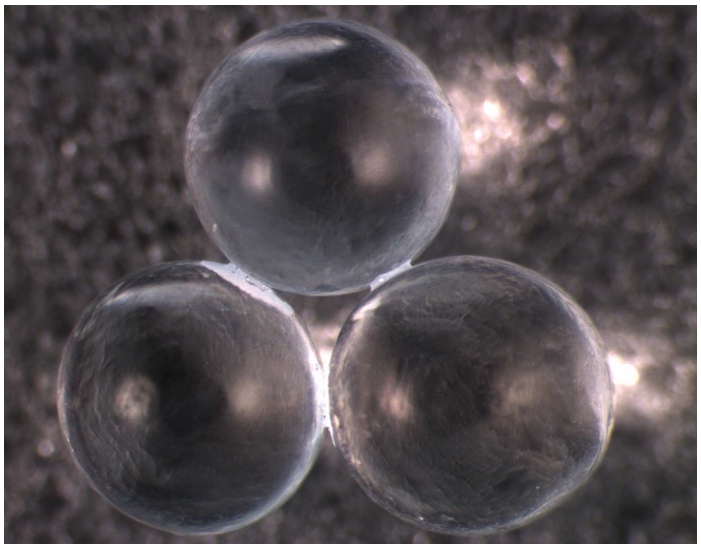

Figure 4-23. NaCl (0.1 M) crystallization on 3 contact packing (soda lime glass, 3 mm diameter).

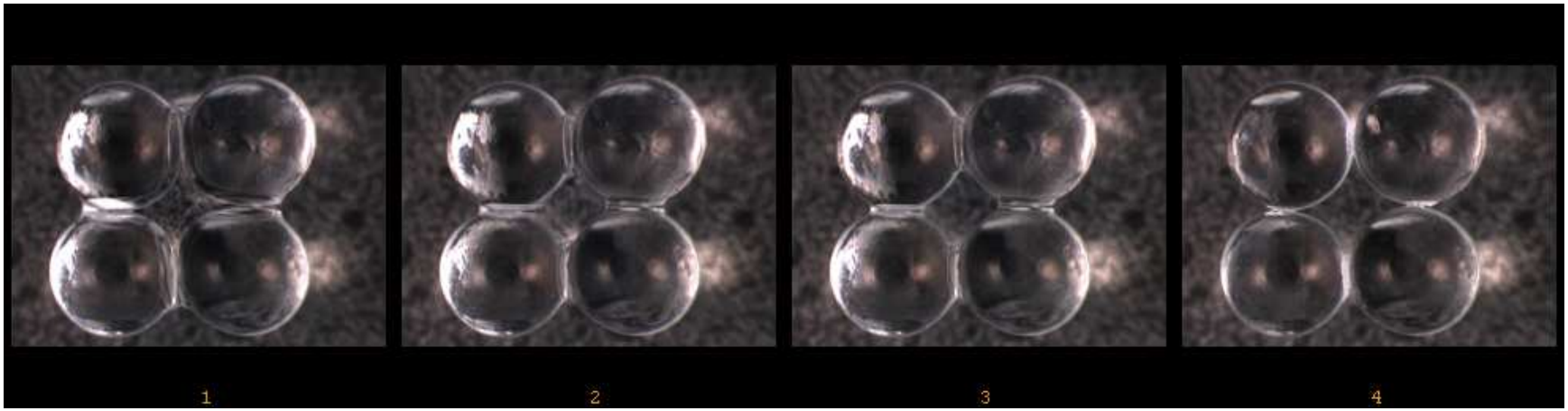

ΔT=20 min

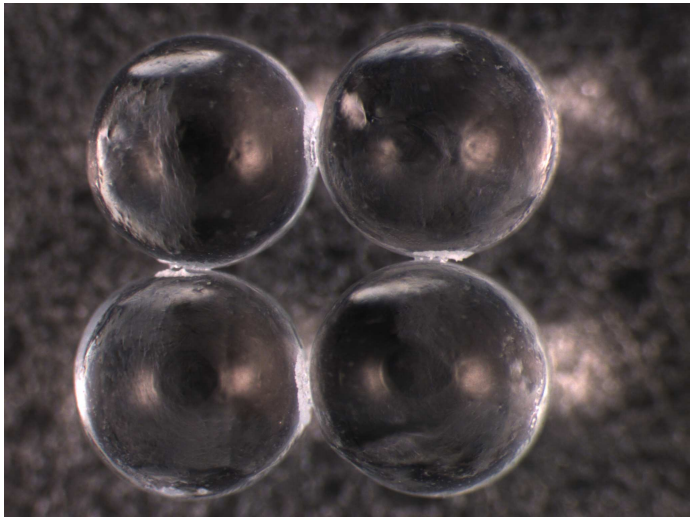

Figure 4-24. NaCl (0.1 M) crystallization on 4 contact packing (soda lime glass, 3 mm diameter).

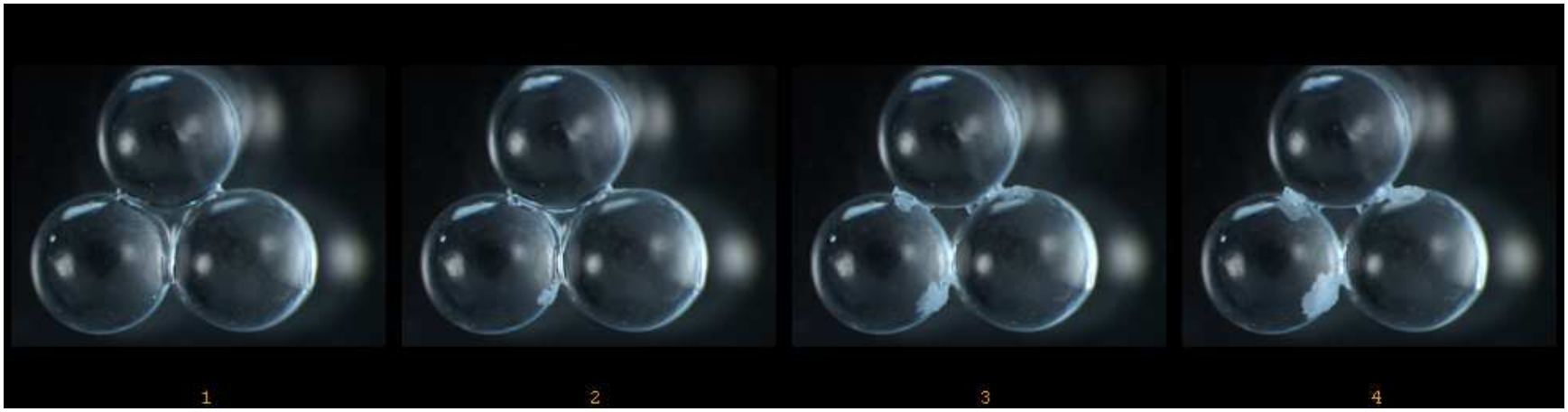

ΔT=10 min

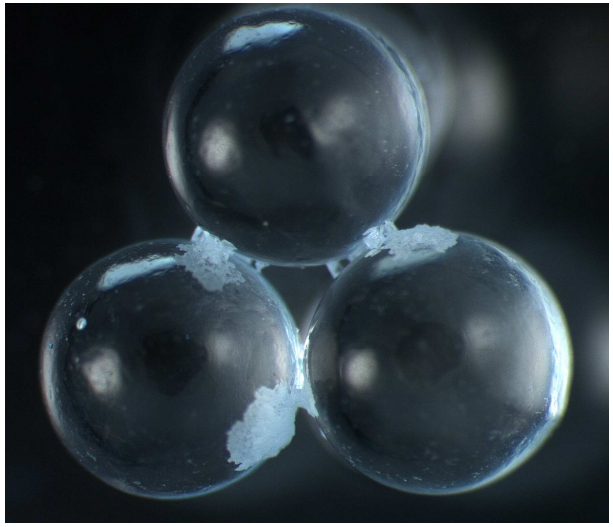

Figure 4-25. NaCl (0.5 M) crystallization on 3 contact packing (soda lime glass, 3 mm diameter).

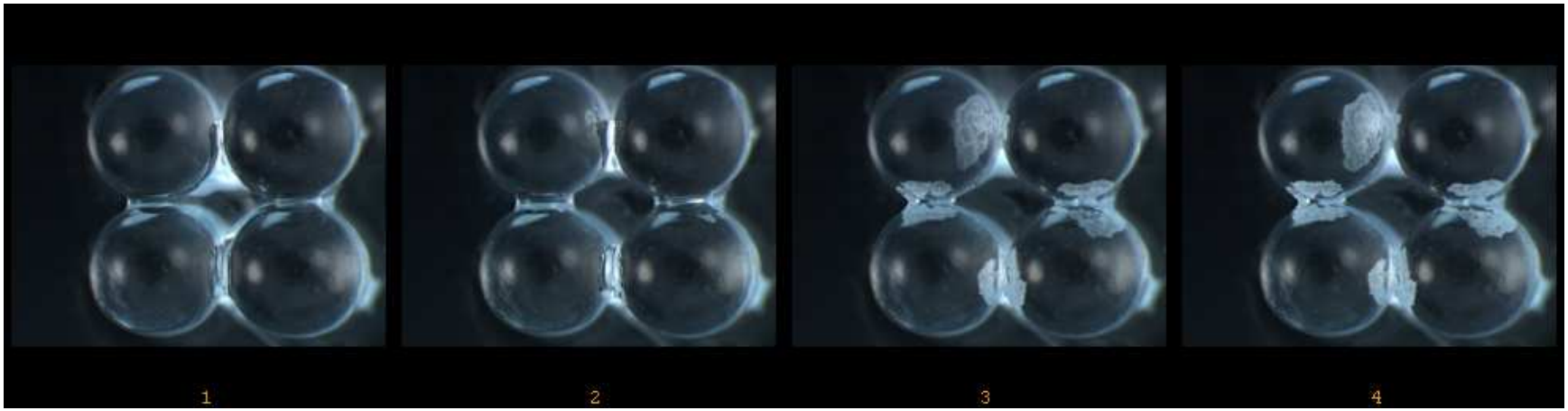

ΔT=10 min

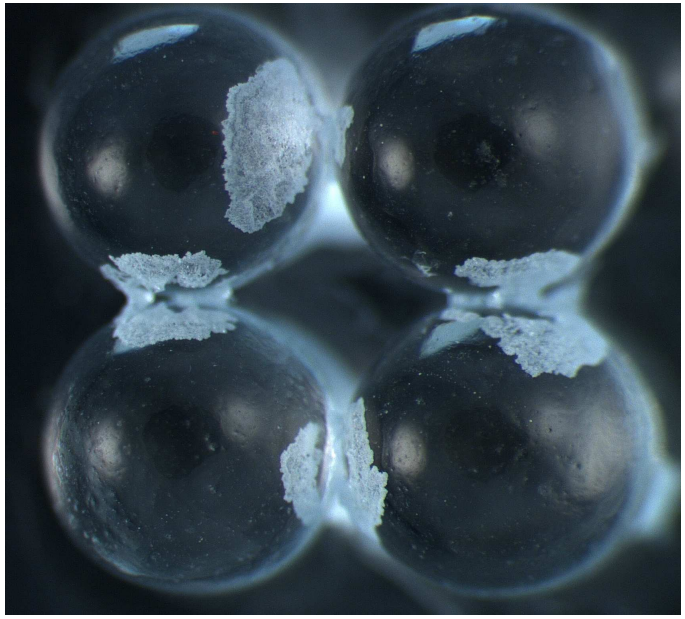

Figure 4-26. NaCl (0.5 M) crystallization on 4 contact packing (soda lime glass, 3 mm diameter).

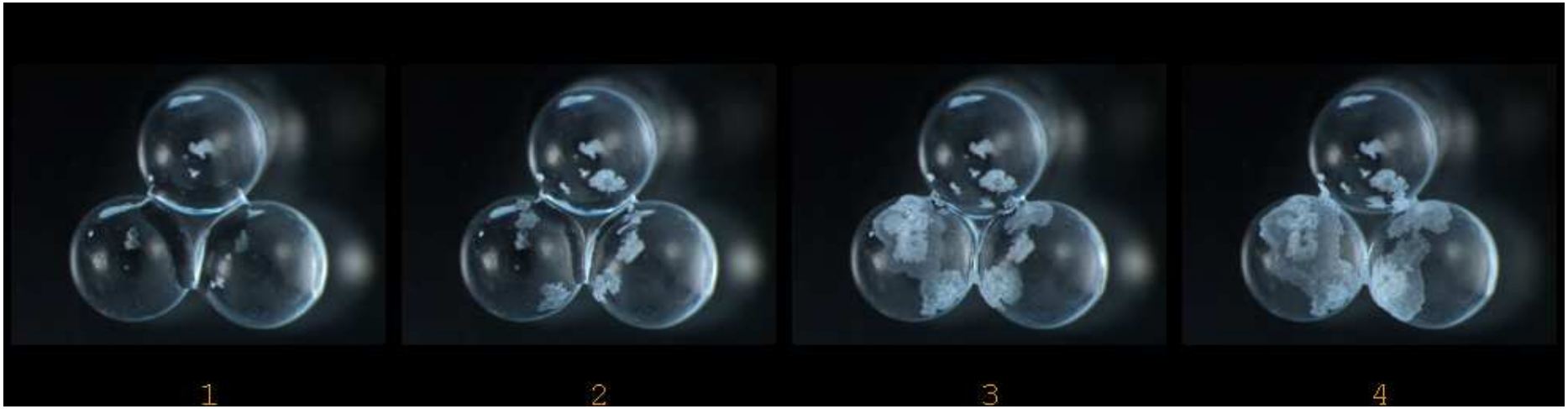

ΔT=5 min

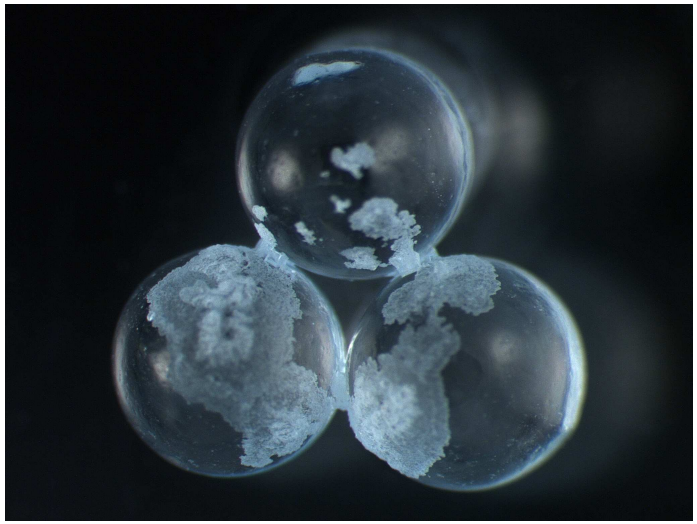

Figure 4-27. NaCl (1 M) crystallization on 3 contact packing (soda lime glass, 3 mm diameter).

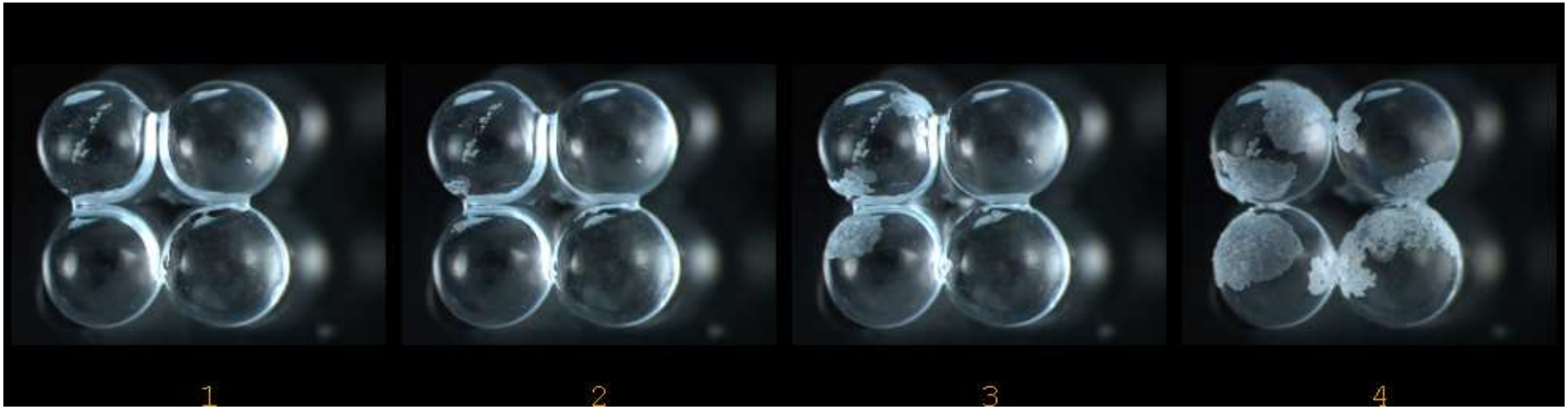

ΔT=5 min

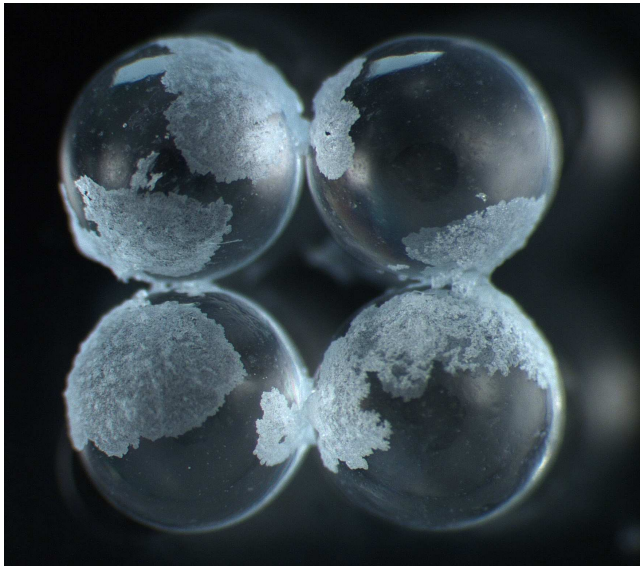

Figure 4-28. NaCl (1 M) crystallization on 4 contact packing (soda lime glass, 3 mm diameter).

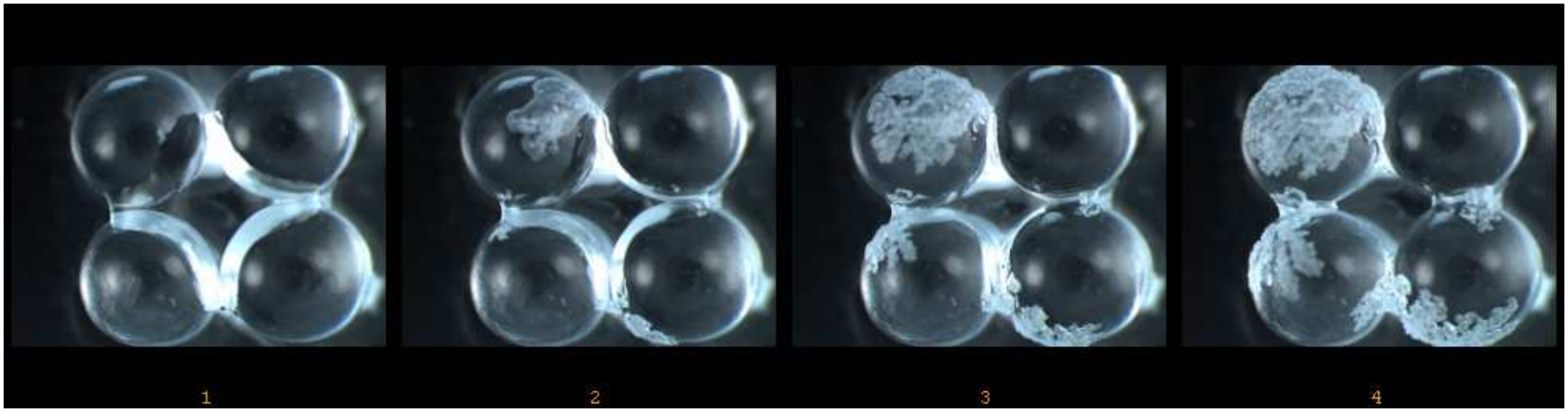

ΔT=5 min

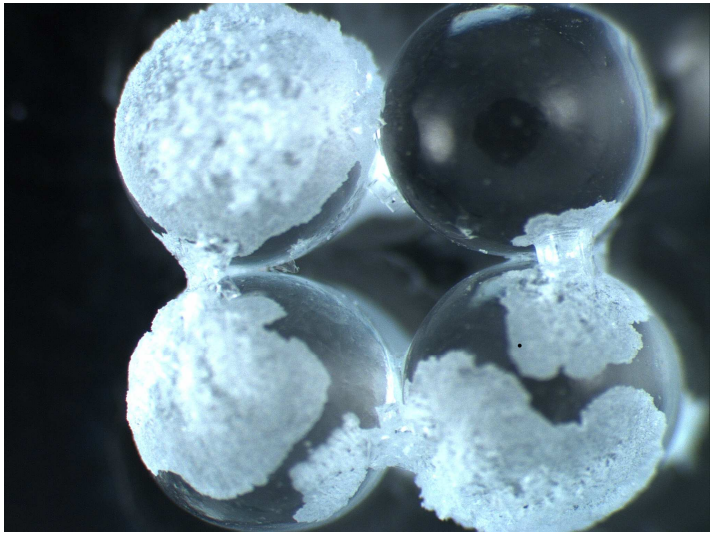

Figure 4-29. NaCl (at saturation) crystallization on 4 contact packing (soda lime glass, 3 mm diameter).

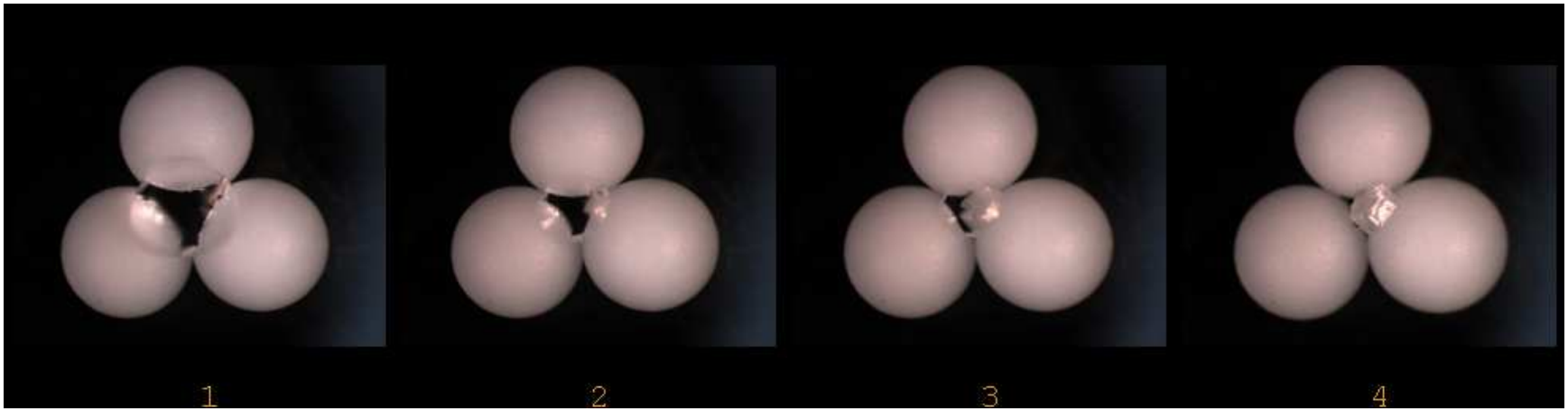

ΔT=5 min

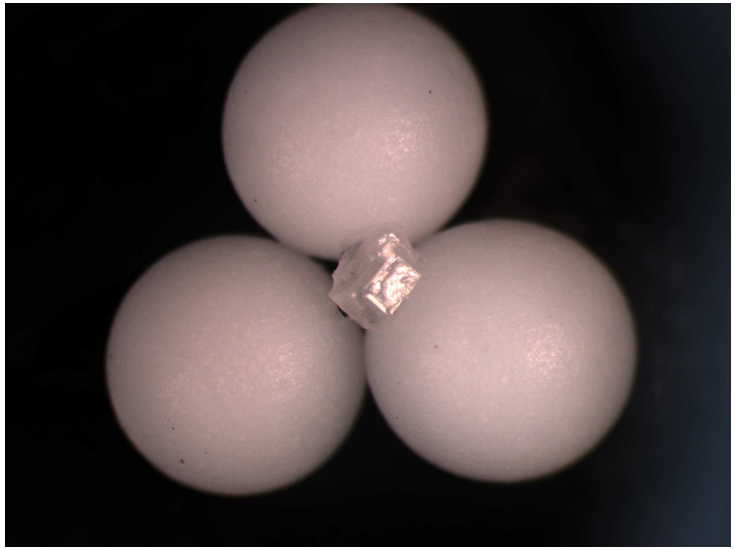

Figure 4-30. NaCl (1 M) crystallization on 3 contact packing (PTFE, 3 mm diameter).

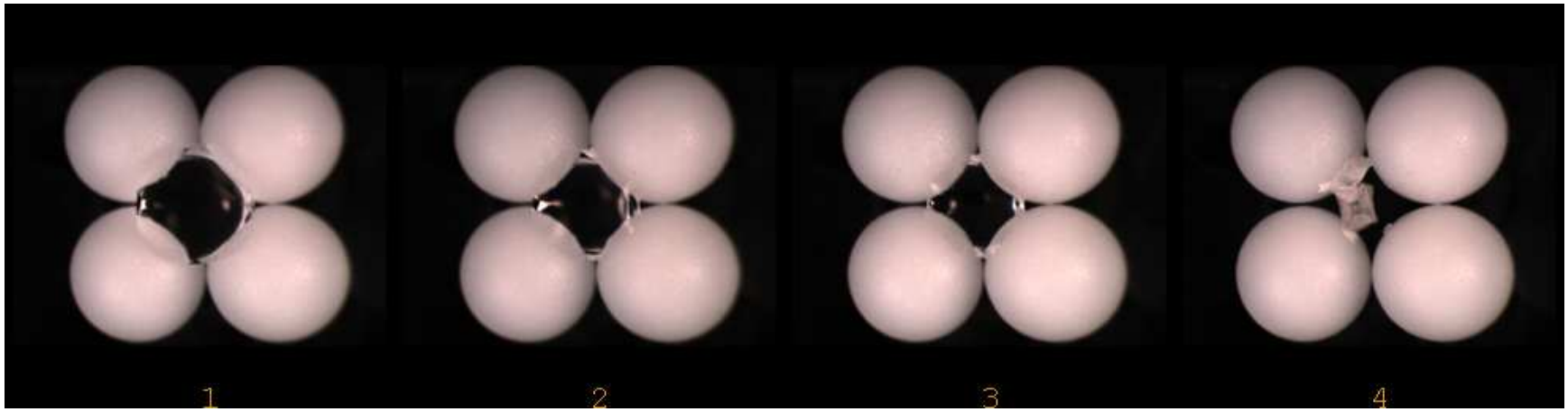

ΔT=10 min

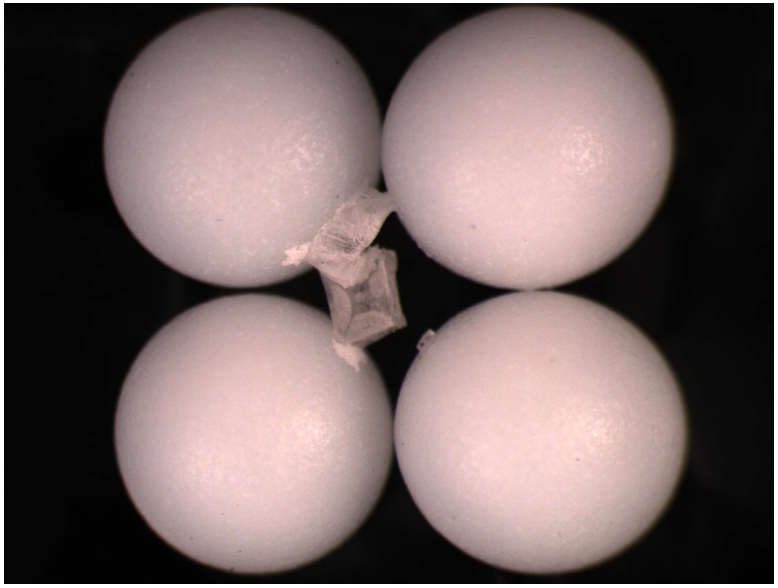

Figure 4-31. NaCl (1 M) crystallization on 4 contact packing (PTFE, 3 mm diameter).

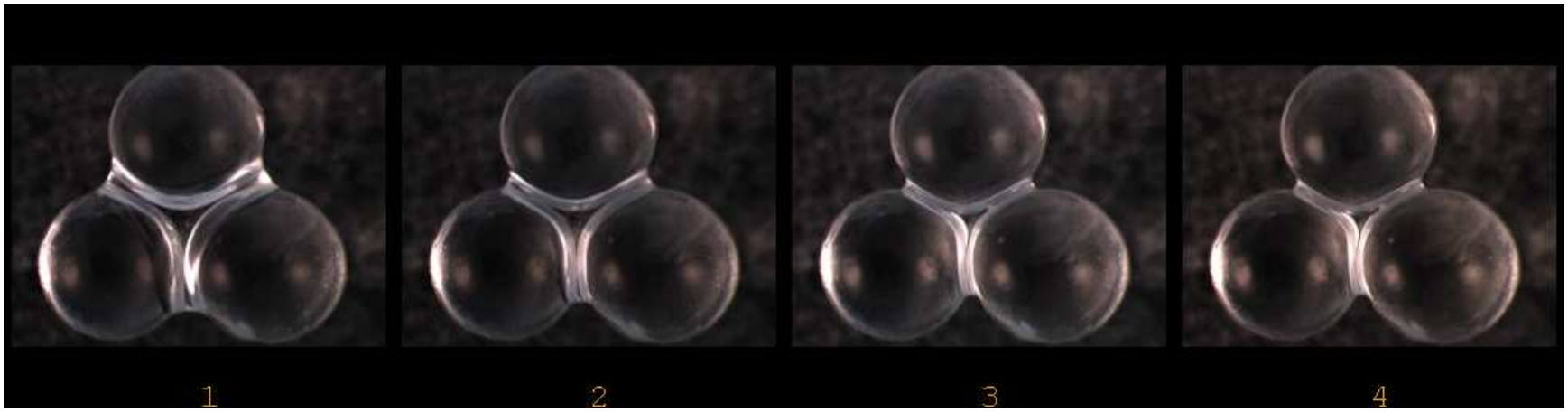

ΔT=5 min

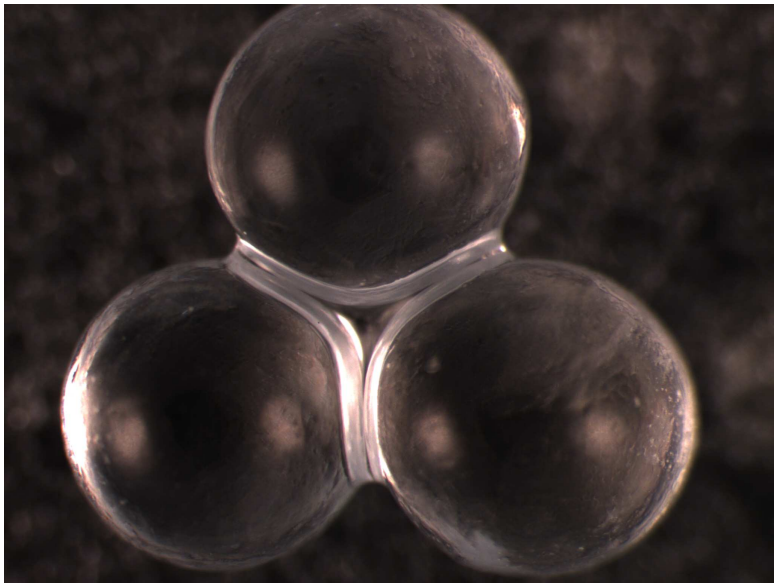

Figure 4-32. $CaCl_2$ (1 M) crystallization on 3 contact packing (soda lime glass, 3 mm diameter).

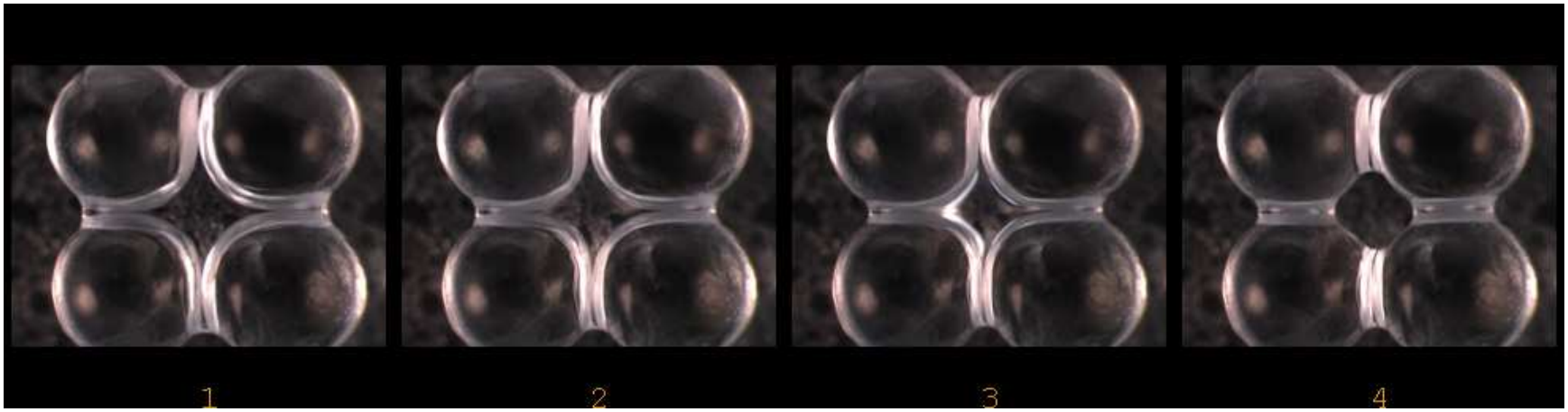

ΔT=10 min

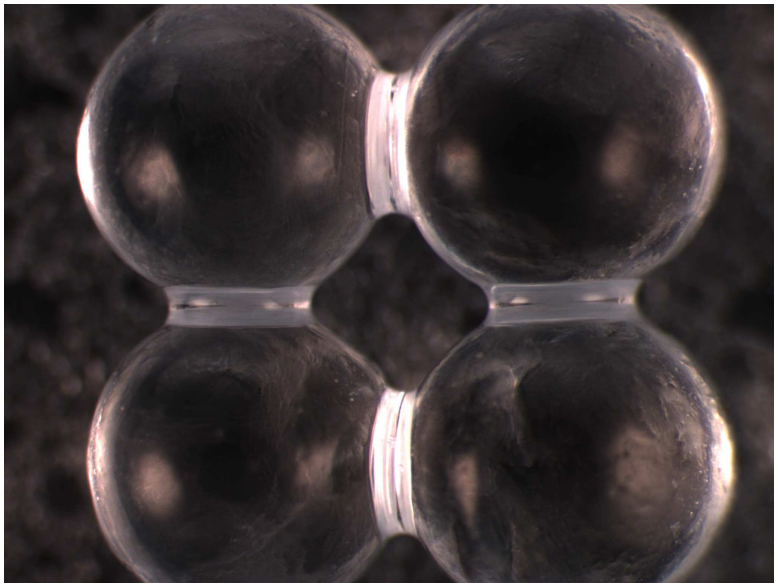

Figure 4-33. $CaCl_2$ (1 M) crystallization on 4 contact packing (soda lime glass, 3 mm diameter).

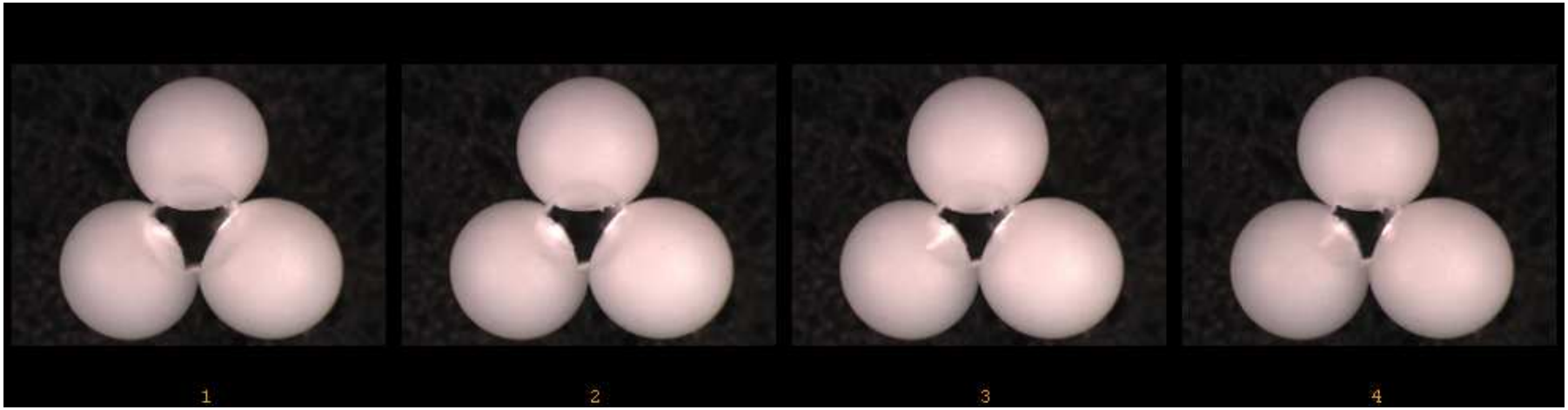

ΔT=20 min

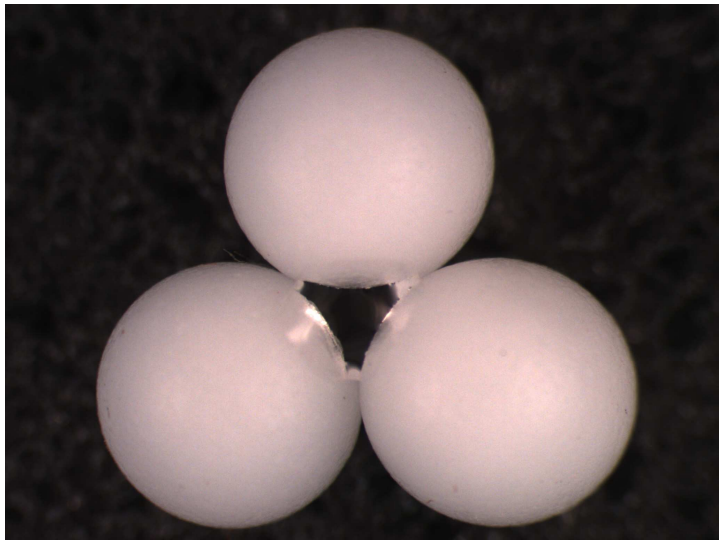

Figure 4-34. $CaCl_2$ (1 M) crystallization on 3 contact packing (PTFE, 3 mm diameter).

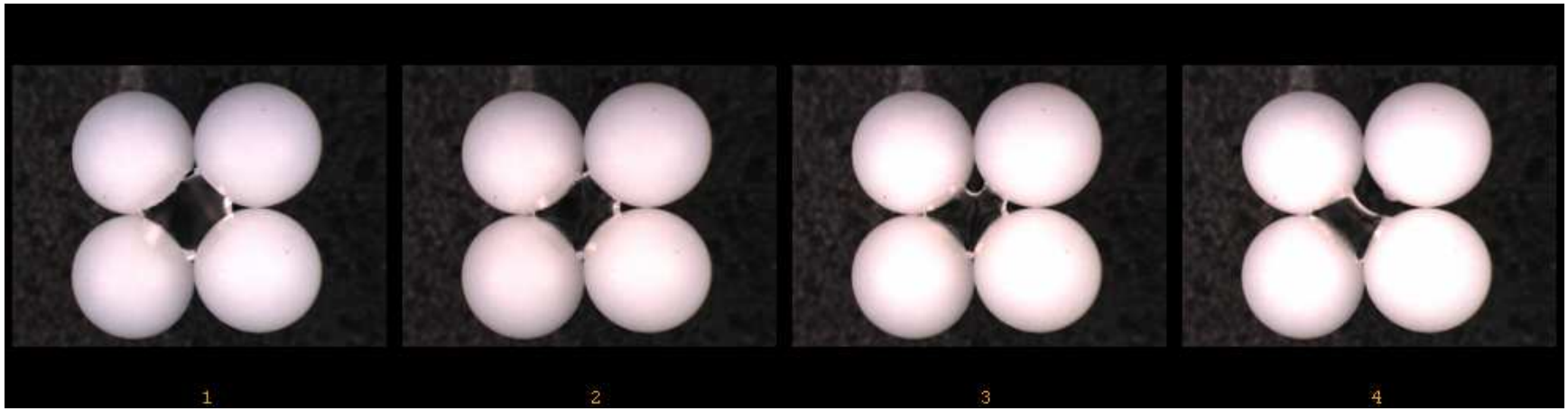

ΔT=20 min

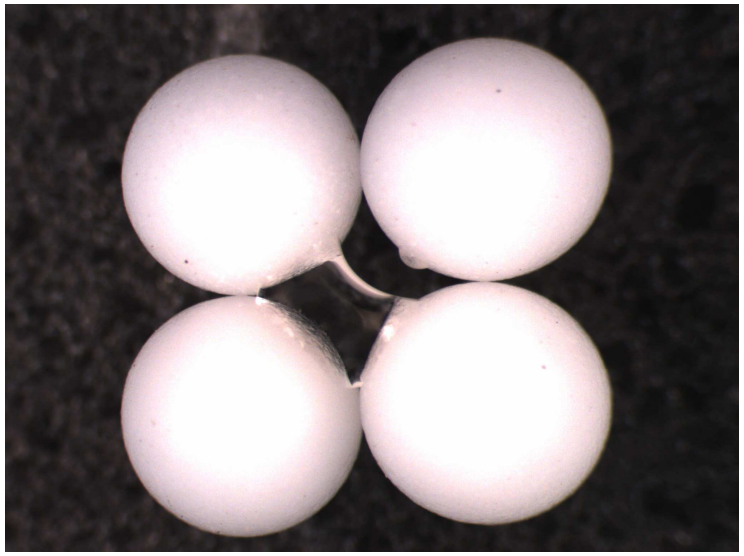

Figure 4-35. $CaCl_2$ (1 M) crystallization on 4 contact packing (PTFE, 3 mm diameter).

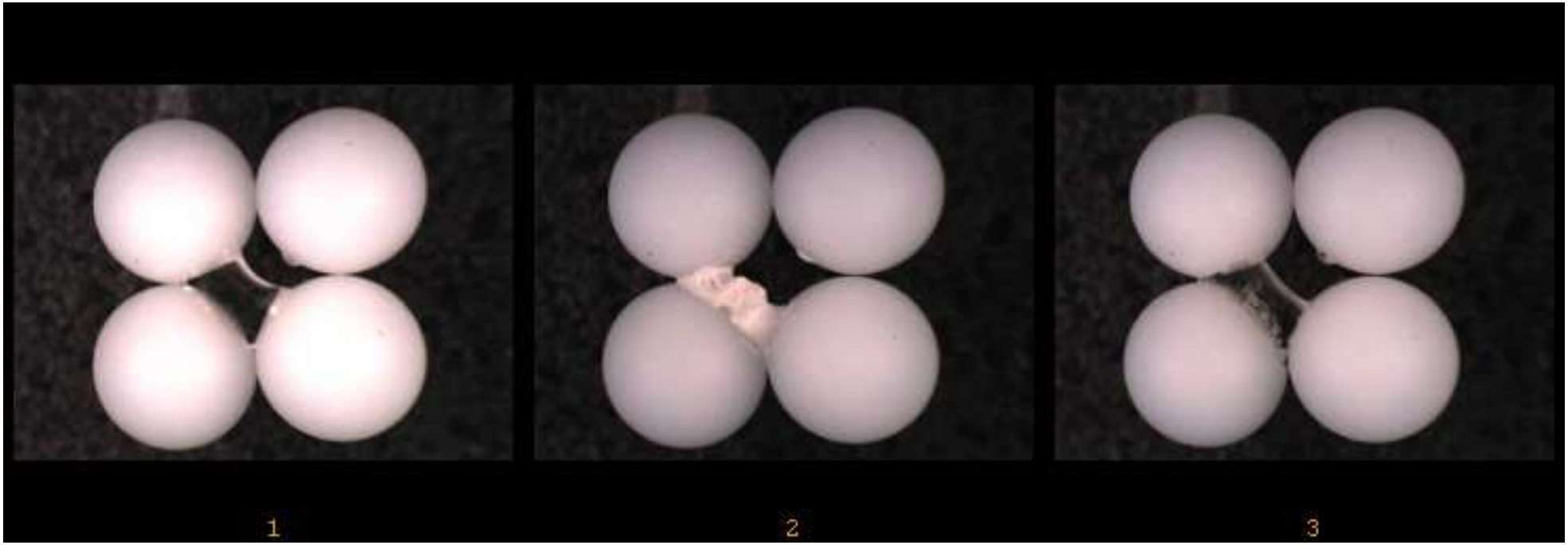

Figure 4-36. Heated evaporation of $CaCl_2$ solution on PTFE surface, and subsequent hygroscopic saturation.

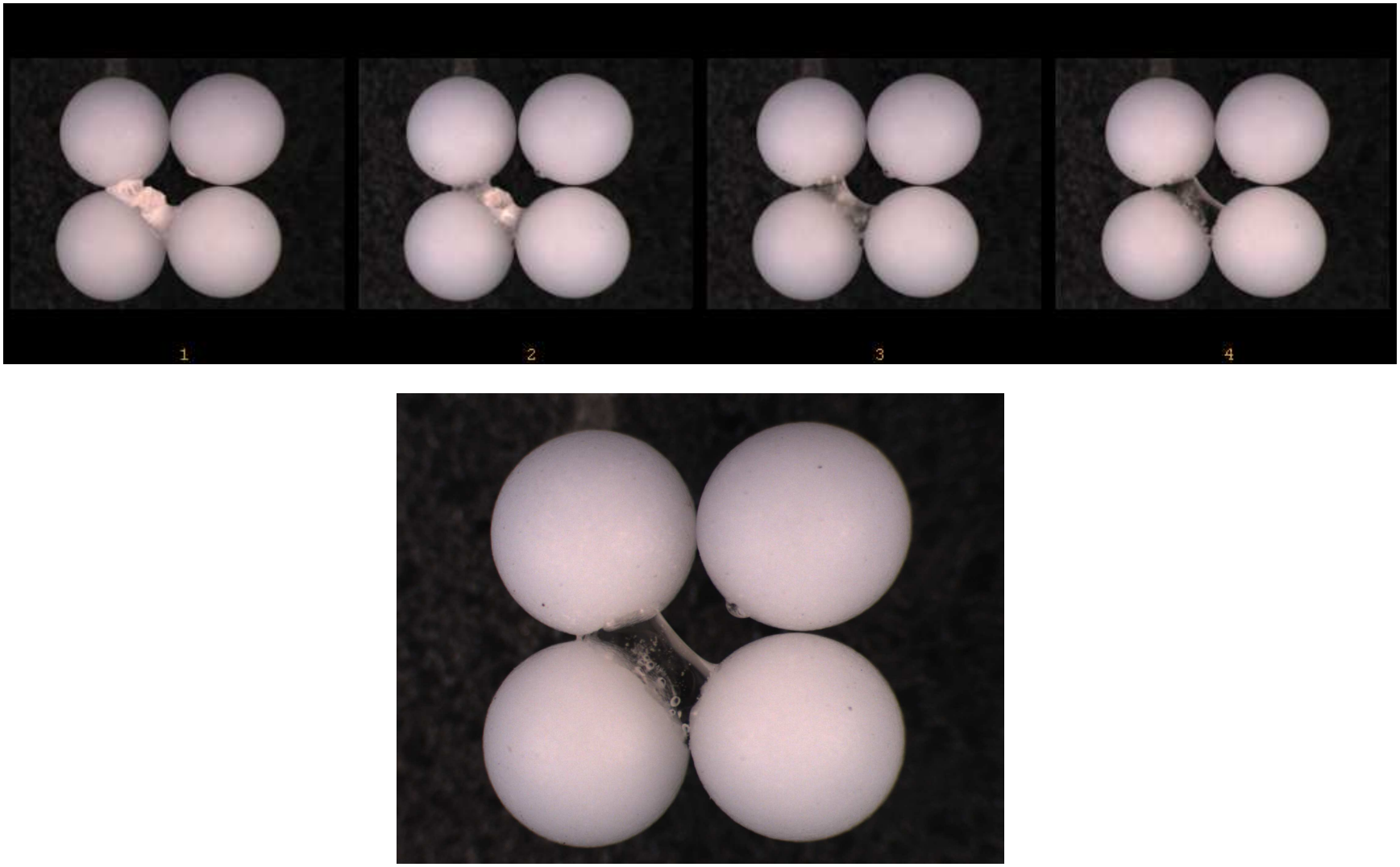

Figure 4-37 $CaCl_2$ (1 M) hygroscopic satruation at atmospheric humidity on 4 contact packing (PTFE, 3 mm diameter).

4.7. Capillary Rise

An estimate of the capillary rise for a coarse-grained soil fabric can be approximated by the Laplace equation (Barnes and Gentle 2005):

$$P_{atm} - P_{fluid} = \frac{2\gamma \cos\theta}{r_c}$$

$$P_{atm} - P_{fluid} = \Delta\rho g h$$

$$h = \frac{2\gamma \cos\theta}{\Delta\rho g r_c}$$

h=capillary rise
r_c=radius of the capillary
$\Delta\rho$=density difference between the liquid and gas
θ=contact angle
γ=surface tension
g=gravity

Estimates of capillary rise were determined for the four studied packings, coupled with the measured solution parameters. Two methods were used to compute the smallest internal radius within each packing. The lower bound (smaller area) estimate was measured by fitting the largest circle possible within the plane of minimal area in each repeating unit (Table 4-2), and the upper bound (larger area) was measured by finding the total area of each minimal plane and calculating the equivalent circle radius (Table 4-3). The calculated minimal internal radius was used for the capillary radius r_c and coupled with the measured surface tension and contact angle to give an estimate of the maximum capillary rise produced in each pore exit of the repeating units as a function of salt concentration and the radius of the particle (Figure 4-38 through Figure 4-45).

Table 4-2. Lower Estimate for Minimal Pore Radii for Studied Packings

Packing	Minimal Pore Radii	Total Minimal Pore Radius (comparison only)
Simple Cubic	6 pores = 0.414r 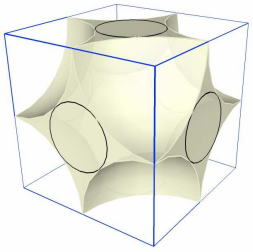	=2.48r
Cubic Tetrahedral	2 pores = 0.164r 3 pores = 0.414r 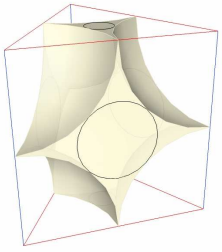	=1.54r
Tetrahedral	10 pores = 0.164r 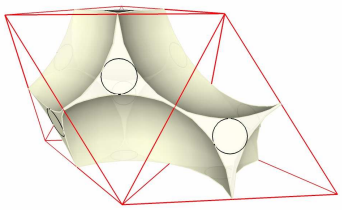	=1.64r
Pyramidal	8 pores = 0.164r 2 pores = 0.414r 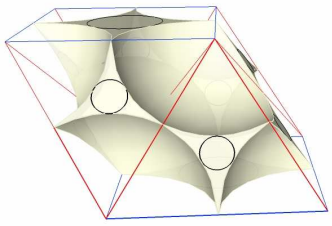	=2.14r

Table 4-3. Upper Estimate for Minimal Pore Radii for Studied Packings

Packing	Minimal Pore Area	Equivalent Radius	Total Equivalent Pore Radius (comparison only)
Simple Cubic	6 pores = $0.894r^2$ 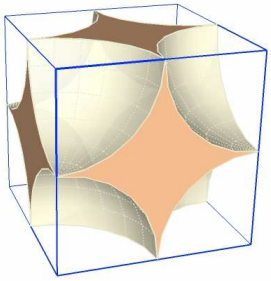	6 large pores= 0.533r	=3.318r
Cubic Tetrahedral	2 pores = $0.192r^2$ 3 pores = $0.894r^2$ 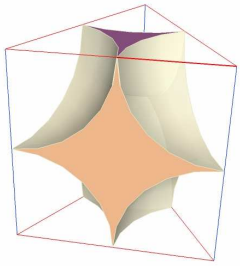	2 small pores= 0.247r 3 large pores= 0.533r	=2.093r
Tetrahedral	10 pores = $0.192r^2$ 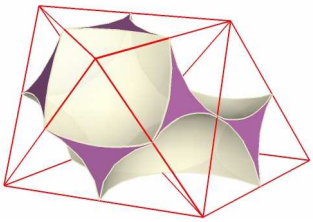	10 small pores= 0.247r	=2.47r
Pyramidal	8 pores = $0.192r^2$ 2 pores = $0.894r^2$ 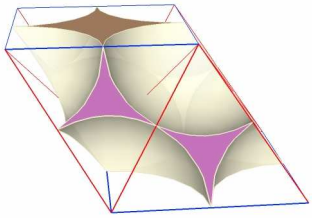	8 small pores= 0.247r 2 large pores= 0.533r	=3.042r

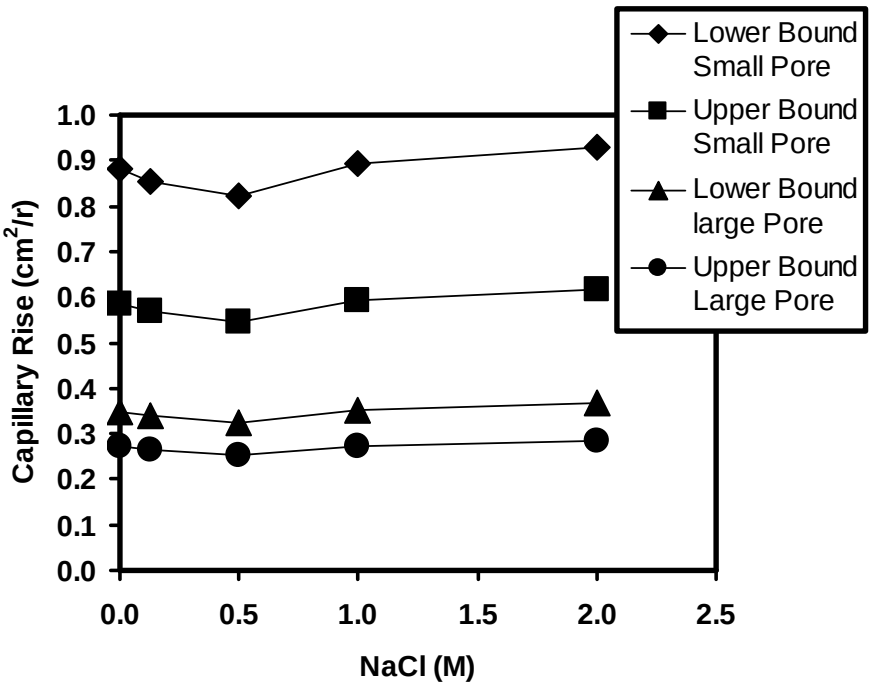

Figure 4-38. Capillary rise for pre-wetted soda lime glass substrate in large and small pores as a function of NaCl concentration.

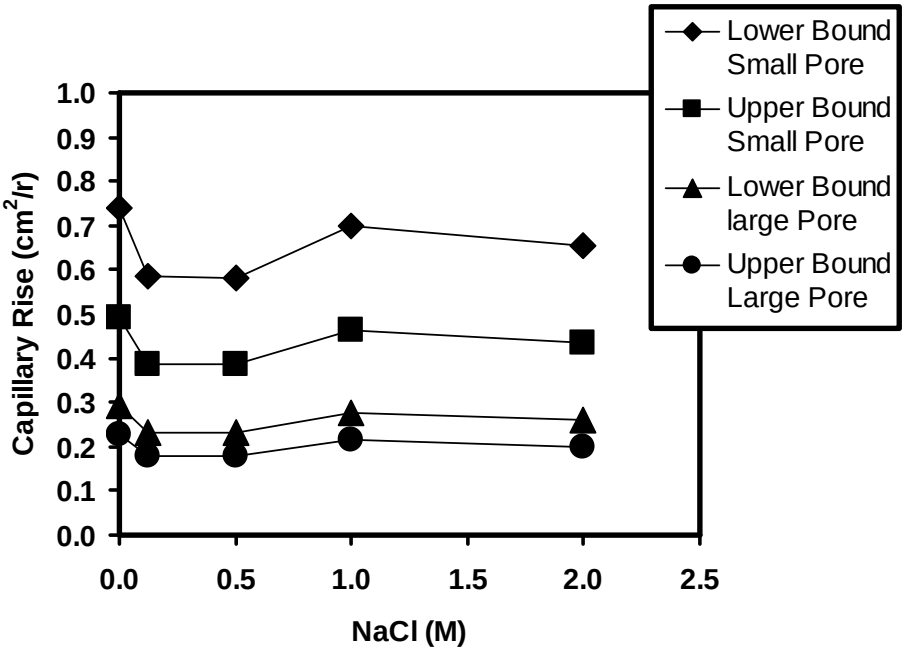

Figure 4-39. Capillary rise for desiccated soda lime glass substrate in large and small pores as a function of NaCl concentration.

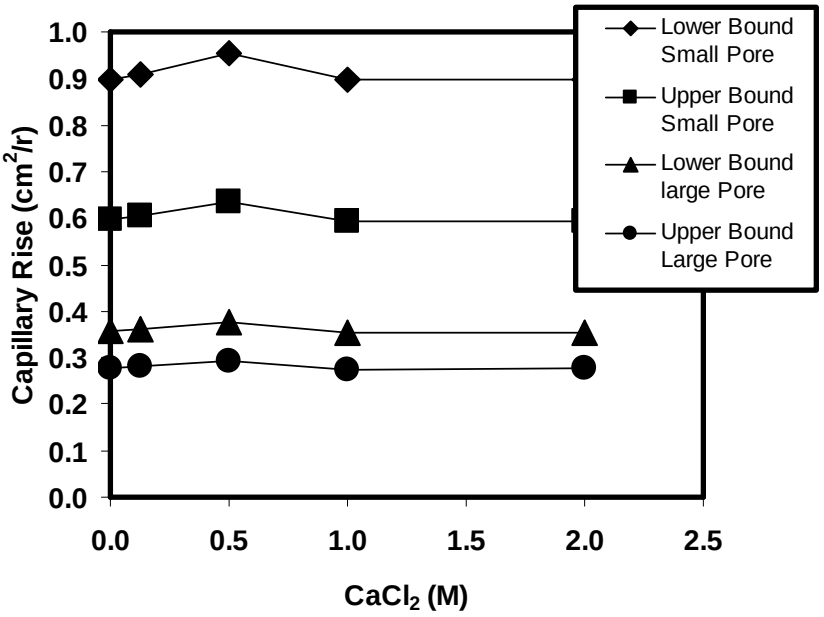

Figure 4-40. Capillary rise for pre-wetted soda lime glass substrate in large and small pores as a function of $CaCl_2$ concentration.

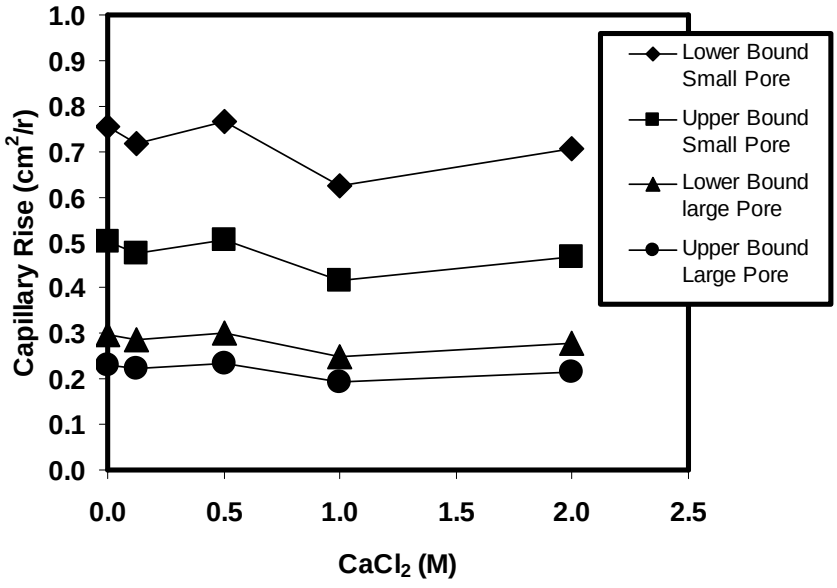

Figure 4-41. Capillary rise for desiccated soda lime glass substrate in large and small pores as a function of $CaCl_2$ concentration.

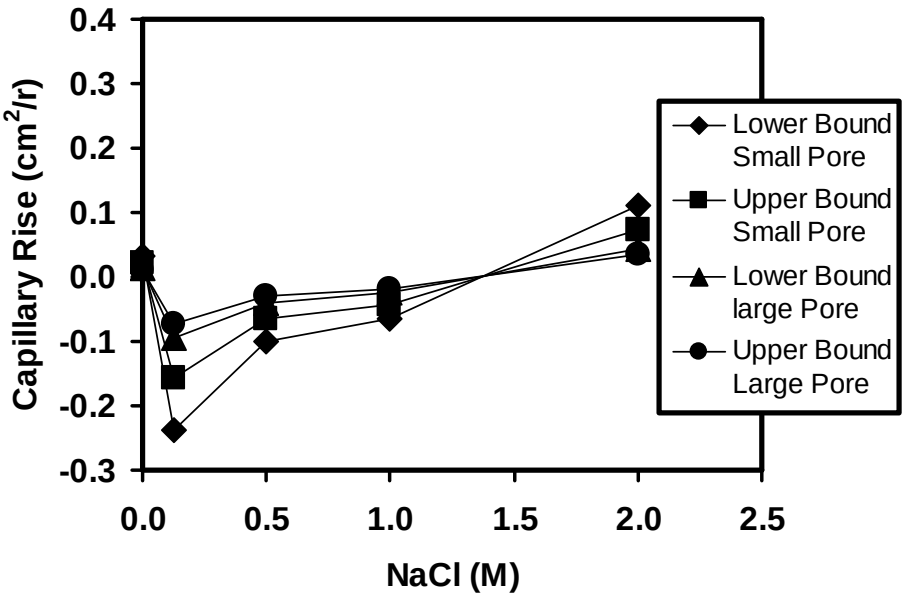

Figure 4-42. Capillary rise for pre-wetted PTFE substrate in large and small pores as a function of NaCl concentration.

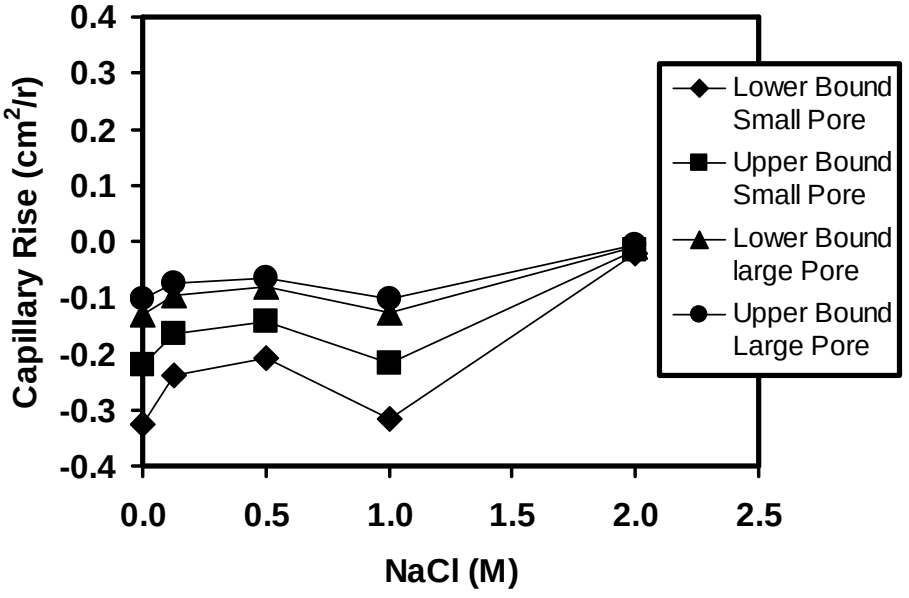

Figure 4-43. Capillary rise for desiccated PTFE substrate in large and small pores as a function of NaCl concentration.

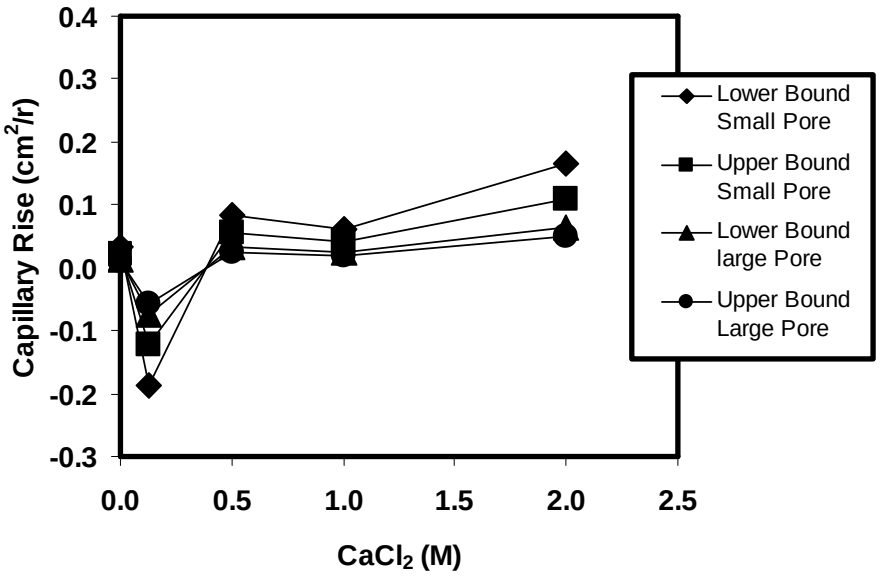

Figure 4-44. Capillary rise for pre-wetted PTFE substrate in large and small pores as a function of $CaCl_2$ concentration.

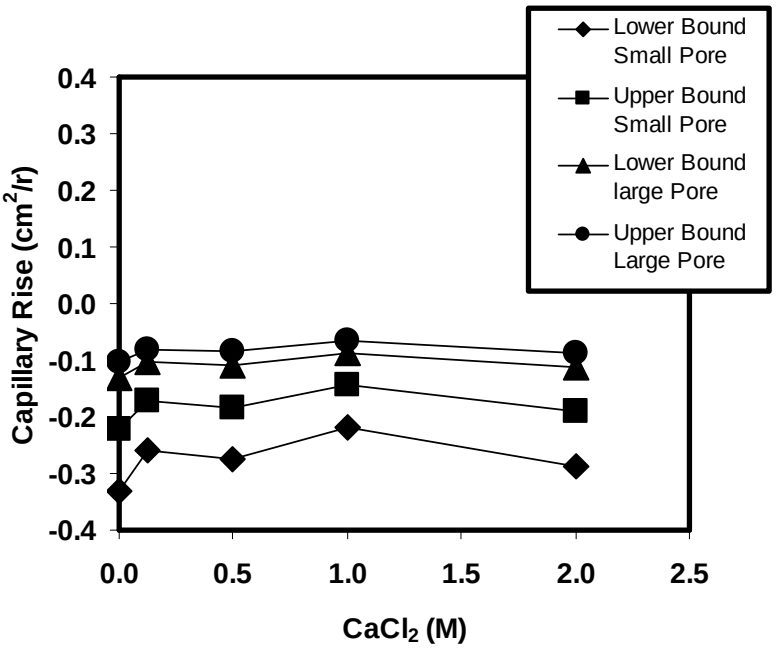

Figure 4-45. Capillary rise for desiccated PTFE substrate in large and small pores as a function of CaCl2 concentration.

Comparison of the height of capillary rise as a function of salt concentration within the pore fluid demonstrated that increasing dissolved salt concentration as high as 2M had little effect on the ultimate capillary rise within the soil fabric in the case of an advancing fluid interface (i.e., wetting front) (Figure 4-46 and Figure 4-47); however, in conditions where the receding contact angle was operable, the height of capillary rise could be influenced (Figure 4-48 and Figure 4-49). The hydrophobicity of the solid surface had a significant effect on the height of capillary rise, with of fluid rise decreasing as the hydrophobicity was increased. The presence of dissolved salts substantially altered the contact angle with the PTFE surface, which in turn substantially reduced the predicted height of capillary rise at low salt concentrations, but increased the predicted rise at high salt concentrations (Figure 4-46 through Figure 4-49).

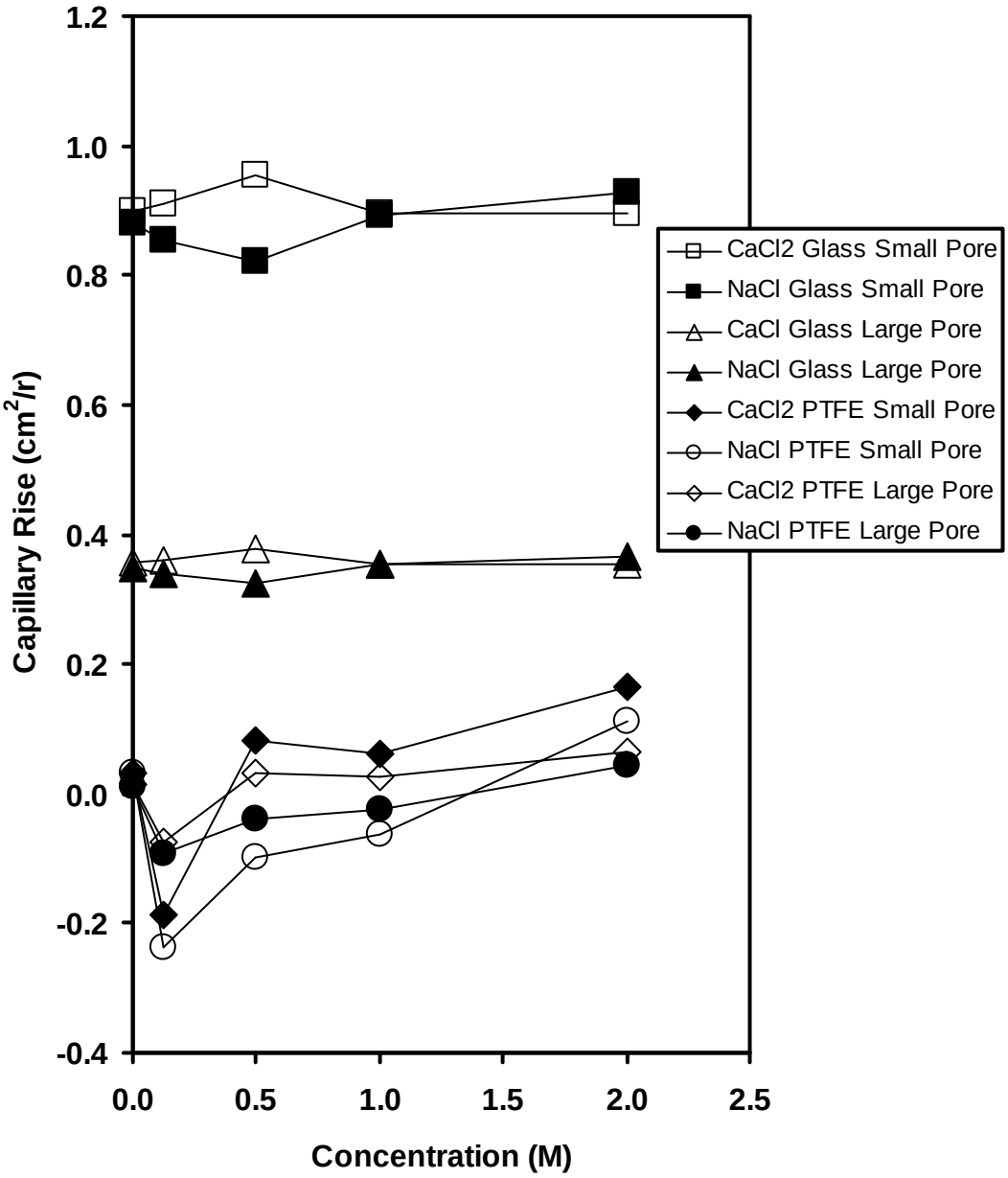

Figure 4-46. Lower bound capillary rise for pre-wetted substrates.

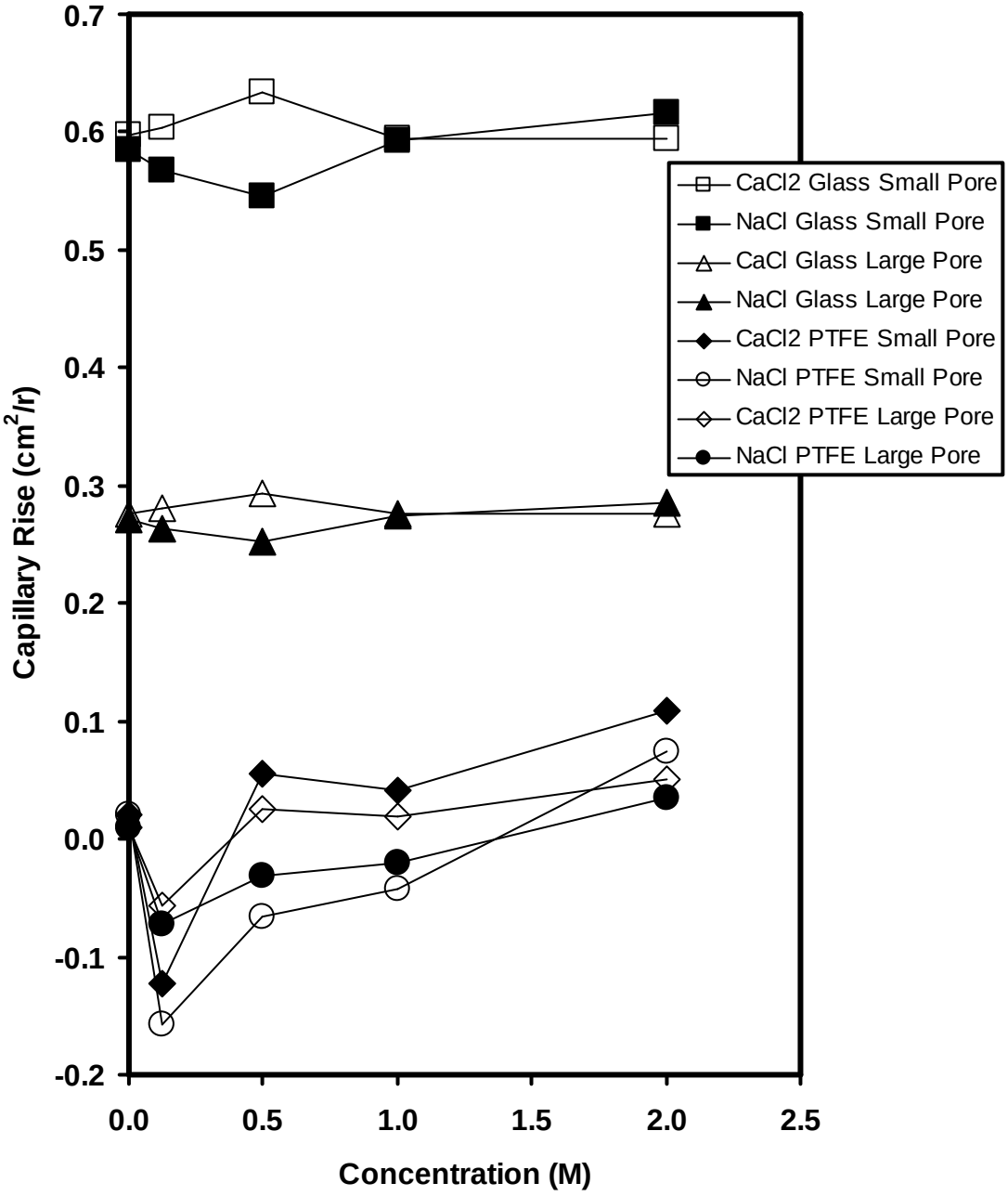

Figure 4-47. Upper bound capillary rise for pre-wetted substrates.

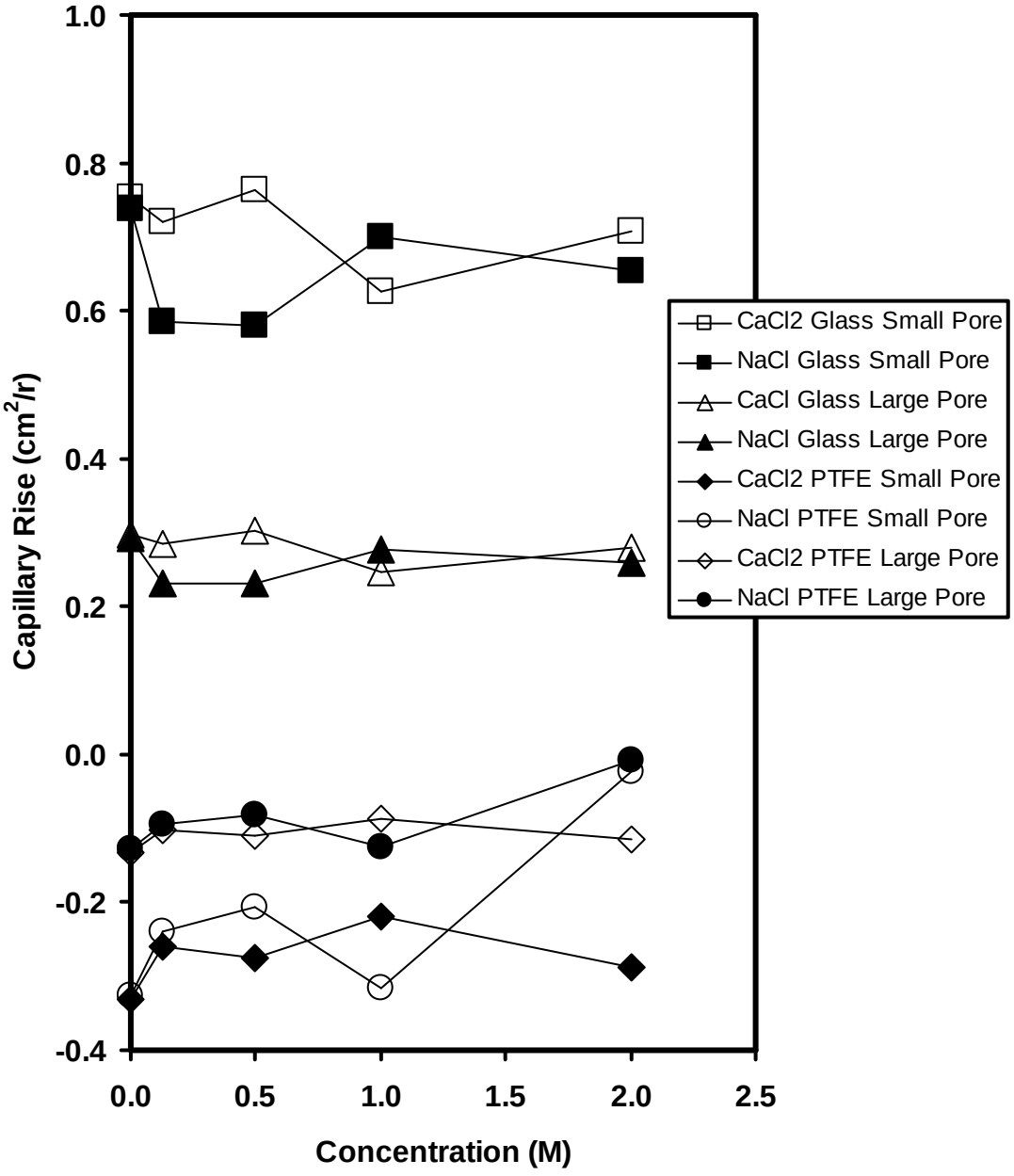

Figure 4-48. Lower bound capillary rise for desiccated substrates.

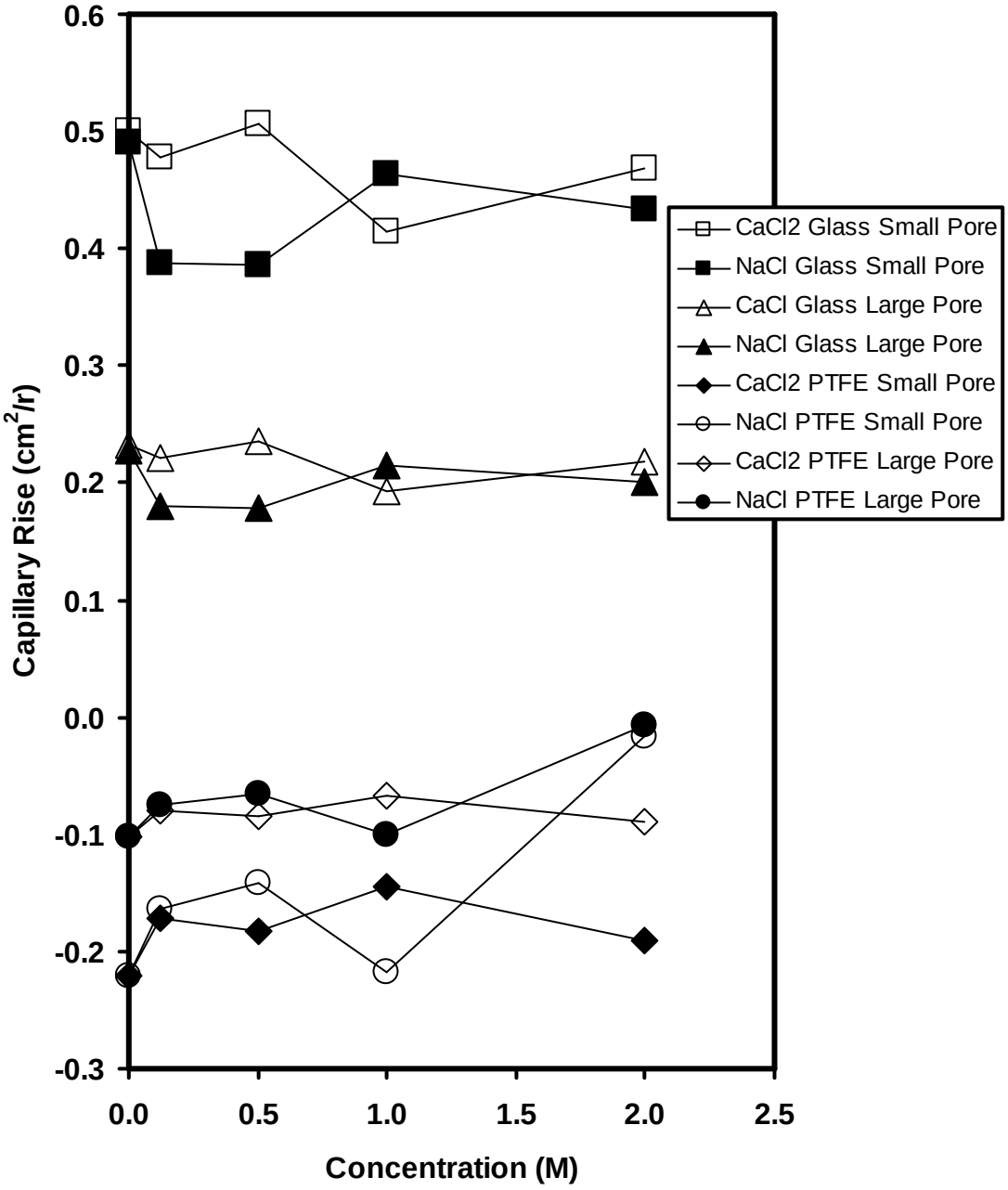

Figure 4-49. Upper bound capillary rise for desiccated substrates.

4.8. Discussion

Because the menisci act between particles, the overall behavior due to the menisci will depend on the soil packing and fabric (Lu et al. 2007). Through the study of the two sphere menisci system, the behavior of menisci in different packings can be extrapolated; however, this model does make some assumptions that need to be addressed. It was assumed that each meniscus was independent of all other menisci. While this may be true late in the pendular stage, it does not hold true at higher levels of saturation when the menisci are continuously connected by a thin water film that covers all of the particles, even after the air infiltration. This thin water film allows dissolved air to diffuse between the connected menisci (Gili and Alonso 2002). However, because this model also assumed that the pore air and menisci pressures were at equilibrium and uniform between menisci and pores, the model would still give a reasonable approximation, as connected menisci would be at equilibrium, allowing comparison between the different packing geometries. Because this model assumed that all particles in the packings were in contact with one another, it only predicted the maximum principle loadings before deformation occurred, and not menisci breakage. Because the tensile strength of meniscus was dependent on the distance between the anchored particles (Lian et al. 1993; Molenkamp and Nazemi 2003a), the decrease in the resultant principle tensile strengths would change as function of the new geometry, due to deformation which is unique to each packing and loading circumstance.

4.9. Engineering implications

Matric suction has a significant effect on the behavior of coarse-grained soils, and the coarse-grained soil packing also exerts a significant effect on the frictional strength characteristics of the soil. While uniform, perfect packing of spheres does not occur in

natural systems, insight into the trends that are observable from experimental study of these model systems is useful. Clearly, packing and the arrangement of pore space is also an important consideration in the ability of water to flow through a porous medium, which in turn will alter the strength of a soil (before and after a wetting event) due to a temporal dependence on tensile strength attributable to partial saturation (Gili and Alonso 2002).

For example, the partial wetting of an expansive soil acts to create tensile stress in the soil which can reduce the degree of swell. However, because menisci are free to rotate and slide along the surface of particles, only the menisci that are being deformed due to an increasing contact length will act against the expansion. Likewise, if a contractive soil is wetted when the contacts of the particles are close enough for menisci to form, then the menisci with particles that are not touching may help to accelerate the volume decrease. Also, because cementation can occur due to the precipitation of salts and minerals, the concept of loading before cementation and cementation before loading becomes important (Fernandez and Santamarina 2001).

When electrolytes are added into the pore fluid, both the liquid-air interfacial energy (surface tension), and liquid-solid interfacial energy increase. These interfacial energy increases result in a magnification of the hydrophilic or hydrophobic behavior of the particle medium. Additionally, any coatings that are present on the soil particles can have a significant impact on the behavior of the soil because the coatings alter the interfacial energy between the solid/liquid/gas phases, and may also alter the surface tension and contact angle of the fluid phase. Tests to compare salt precipitation patterns for beads that had been prerinsed with hydrogen peroxide to beads that had not been

prerinsed demonstrated that the presence of the light atmospheric deposited organic coating resulted in clumping and isolated crystallization, when compared to the relatively well distributed crystals that formed after H_2O_2 washing (Figure 4-50 and Figure 4-51).

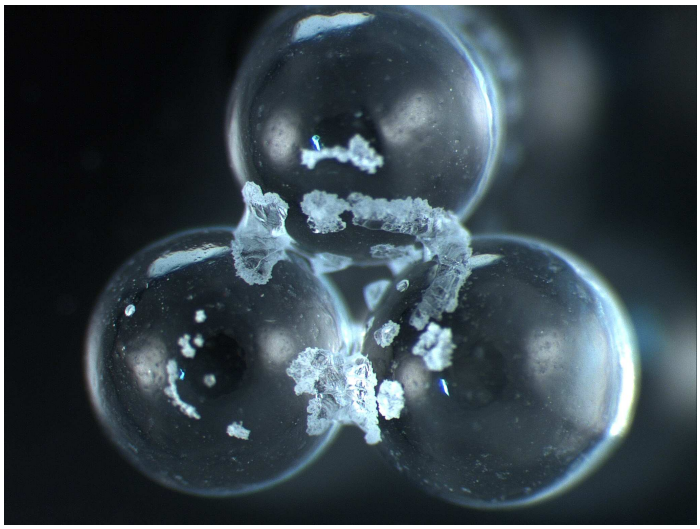

Figure 4-50. Salt crystallization patterns with no hydrogen peroxide prerinse.

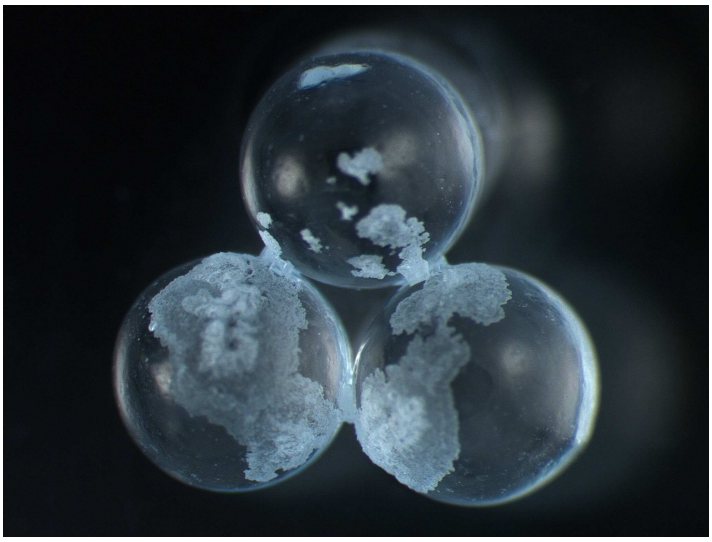

Figure 4-51. Salt crystallization patterns with hydrogen peroxide prerinse.

Chapter 5

CONCLUSIONS

5.1. Overview

In this study, the behavior of partially saturated coarse-grained soil packings was studied as a function of solid surface composition and aqueous salt concentration. The substrates tested were PTFE and soda lime glass, while the aqueous electrolytes consisted of NaCl and $CaCl_2$ in differing concentrations. In order to gain a fundamental understanding of the unsaturated soils system, the two-phase intersections of gas-liquid and solid-liquid were studied. The effect of varying aqueous electrolytes on the gas-liquid interface was analyzed by testing the surface tension while systematically varying the electrolyte concentration, while the effect on the solid/liquid/gas interface was studied by altering the surface hydrophobicity and aqueous solution concentration. In order to extend the analysis to soil fabrics, four ideal coarse gained packings were subdivided into their smallest repeating units. These repeating units, along with the measured dependence of the contact angles and surface tension on salt types, allowed an estimation of the equilibrium behavior of the capillary rise and tensile strength within a uniform coarse-grained fabric. The major findings of this study include:

- Increasing the hydrophobicity of the solid surface increased both the advancing and receding water contact angles
- Differences between advancing and receding contact angles were more pronounced for hydrophilic substrates

- Increasing salt concentration decreased contact angles for hydrophobic surfaces, but had relatively little effect on hydrophilic surfaces
- Increased salt concentration increased the surface tension of aqueous salt solutions
- Development of representative elementary volumes for four soil packing geometries were developed
- Empirical estimation of the rate of water evaporation between a two-particle contact (visual and mass-based approaches) was developed
- Height of capillary rise is relatively unaffected by the aqueous concentration of salt in contact with hydrophilic surfaces, but substantially altered in the case of hydrophobic surfaces

5.2. Limitations

The primary difficulty in modeling geotechnical engineering systems results from the high variability and complexity of natural systems. In this study, a uniform and ideal packing and particle shape and composition was assumed, in order to simplify the complexity of the natural system and to allow analysis of governing trends. The presence of aqueous electrolytes and differing surface compositions (mineral or chemical) are ubiquitous in both natural and engineered systems, and their influences in the gas-liquid and liquid-solid interfaces will be present in every unsaturated system. The behavior of an unsaturated soil system can be greatly affected through relatively small changes in surface energy or electrolyte composition, and can be vastly changed, depending on the stage of the wetting or drying cycle, and possibility of cementation or meniscus formation.

REFERENCES

Adamson, A. W., and Gast, A. P. (1997). *Physical Chemistry of Surfaces*, John Wiley & Sons, Inc.

Barnes, G. T., and Gentle, I. R. (2005). *Interfacial Science*, Oxford, New York.

Behrens, S. H., and Grier, D. G. (2001). "The charge of glass and silica surfaces." *Journal of Chemical Physics*, 115(14), 6716-6721.

Blomqvist, G., and Johansson, E.-L. (1999). "Airborne spreading and deposition of de-icing salt - a case study." *Science of the Total Environment*, 235(1), 161-168.

Brandrup, J., Immergut, E. H., Grulke, E. A., Abe, A., and Bloch, D. R. (2005). "Polymer Handbook (4th Edition)." John Wiley & Sons, Inc.

Budhu, M. (2007). *Soil Mechanics and Foundations*, John Wiley & Sons, Inc, NJ.

Butkus, M. A., and Grasso, D. (1998). "Impact of aqueous electrolytes on interfacial energy." *Journal of Colloid and Interface Science*, 200(1), 172-172.

Chateau, X., Moucheront, P., and Pitois, O. (2002). "Micromechanics of unsaturated granular media." *Journal of Engineering Mechanics*, 128(8), 856-863.

Cho, G.-C., Dodds, J., and Santamarina, J. C. (2006). "Particle shape effects on packing density, stiffness, and strength: Natural and crushed sands." *Journal of Geotechnical and Geoenvironmental Engineering*, 132(5), 591-602.

Cho, G. C. (2001). "Unsaturated soil stiffness and post liquefaction shear strength," PhD, Georgia Institute of Technology, Atlanta, GA.

Cho, G. C., and Santamarina, J. C. (2001). "Unsaturated particulate materials-particle-level studies." *Journal of Geotechnical and Geoenvironmental Engineering*, 127(1), 84-96.

Doerr, S. H., Shakesby, R. A., and Walsh, R. P. D. (2000). "Soil water repellency: its causes, characteristics and hydro-geomorphological significance." *Earth-Science Reviews*, 51(1-4), 33-65.

Dow Chemical. (2003). "Calcium Chloride Handbook: A Guide to Properties, Forms, Storage and Handling." Dow Chemical.

Drelich, J. L., J.S.; Mittal, K.L. (2000). " Apparent and Microscopic Contact Angles." VSP.

Fernandez, A. L., and Santamarina, J. C. (2001). "Effect of cementation on the small-strain parameters of sands." *Canadian Geotechnical Journal*, 38(1), 191-199.

Gili, J. A., and Alonso, E. E. (2002). "Microstructural deformation mechanisms of unsaturated granular soils." *International Journal for Numerical and Analytical Methods in Geomechanics*, 26(5), 433-468.

Green, S. M., Machin, R., and Cresser, M. S. (2008). "Effect of long-term changes in soil chemistry induced by road salt applications on N-transformations in roadside soils." *Environmental Pollution*, 152(1), 20-31.

Hicher, P.-Y., and Chang, C. S. (2008). "Elastic model for partially saturated granular materials." *Journal of Engineering Mechanics*, 134(6), 505-513.

Iler, R. K. (1979). *Chemistry of Silica - Solubility, Polymerization, Colloid and Surface Properties and Biochemistry*, John Wiley & Sons.

Israelachvili, J. (1992). *Intermolecular & Surface Forces*, Academic Press Limited, London.

Kim, D., Kim, J., Park, H. C., Lee, K.-H., and Hwang, W. (2008). "A superhydrophobic dual-scale engineered lotus leaf." *Journal of Micromechanics and Microengineering*, 18(1).

Li, X. S. (2003). "Effective stress in unsaturated soil: A microstructural analysis." *Geotechnique*, 53(2), 273-277.

Lian, G. P., Thornton, C., and Adams, M. J. (1993). "A theoretical-study of the liquid bridge forces between 2 rigid spherical bodies." *Journal of Colloid and Interface Science*, 161(1), 138-147.

Lu, N., and Likos, W. J. (2004). *Unsaturated Soil Mechanics*, John Wiley & Sons, Inc.

Lu, N., and Likos, W. J. (2006). "Suction stress characteristic curve for unsaturated soil." *Journal of Geotechnical and Geoenvironmental Engineering*, 132(2), 131-142.

Lu, N., Wu, B., and Tan, C. P. (2007). "Tensile strength characteristics of unsaturated sands." *Journal of Geotechnical and Geoenvironmental Engineering*, 133(2), 144-154.

Lundmark, A., and Olofsson, B. (2007). "Chloride deposition and distribution in soils along a deiced highway - Assessment using different methods of measurement." *Water, Air, and Soil Pollution*, 182(1-4), 173-185.

Maheshwari, R., Sreeram, K. J., and Dhathathreyan, A. (2003). "Surface energy of aqueous solutions of Hofmeister electrolytes at air/liquid and solid/liquid interface." *Chemical Physics Letters*, 375(1-2), 157-61.

McHale, G., Shirtcliffe, N. J., Newton, M. I., and Pyatt, F. B. (2007a). "Implications of ideas on super-hydrophobicity for water repellent soil." *Hydrological Processes*, 21(17), 2229-38.

McHale, G., Shirtcliffe, N. J., Newton, M. I., Pyatt, F. B., and Doerr, S. H. (2007b). "Self-organization of hydrophobic soil and granular surfaces." *Applied Physics Letters*, 90(5), 54110-1.

Mitchell, J. K., and Soga, K. (2005). *Fundamentals of Soil Behavior*, John Wiley & Sons, Inc., Hoboken, New Jersey.

Mittal, K. L. (2002). *Contact Angle, Wettability and Adhesion, Volume 2.*, VSP - An imprint of BRILL.

Molenkamp, F., and Nazemi, A. H. (2003a). "Interactions between two rough spheres, water bridge and water vapour." *Geotechnique*, 53(2), 255-264.

Molenkamp, F., and Nazemi, A. H. (2003b). "Micromechanical considerations of unsaturated pyramidal packing." *Geotechnique*, 53(2), 195-206.

Nanotechnology and Interdisciplinary Research Initiative. (2009). "Role of roughness as an amplifier."

Quere, D. (2002). "Rough ideas on wetting." Physica A: Statistical Mechanics and its Applications, Elsevier, Altenberg, Germany, 32-46.

Santamarina, J. C. (2003). "Soil behavior at the microscale: Particle forces." *American Society of Civil Engineers*, Geotechnical Special Publication 119, 25-56.

Santamarina, J. C., Klein, K. A., and Fam, M. A. (2001). *Soils and Waves: Particulate Materials Behavior, Characterization and Process Monitoring*, John Wiley & Sons, Inc.

Thompson, R. L., Hutchings, L. R., Narrainen, A. P., Eggleston, S. M., and Clarke, N. (2006). "Surface-active fluorocarbon end-functionalized polylactides." *Polymer*, 47(24), 8116-22.

Trevena, D. H. (1984). "Cavitation and the generation of tension in liquids." *Journal of Physics D: Applied Physics*, 17(11), 2139-2164.

Washburn, E. W. (2003). "International Critical Tables of Numerical Data, Physics, Chemistry and Technology (1st Electronic Edition)." Knovel.

Wisconsin Transportation Bulletin. (1997). "Using Salt and Sand for Winter Road Maintenance " Road Management Journal.

Zumdahl, S. (2003). *Chemistry*, Houghton Mifflin Company.